EVALUATION OF THE DOSIMETRIC ACCURACY IN THE PRESENCE OF INHOMOGENEITIES OF TWO COMMERCIAL ELECTRON PLANNING SYSTEMS

by

James Beck

A practicum submitted to the faculty of Graduate Studies of the University of Manitoba

in partial fulfillment of the requirements for the degree of

MASTER OF SCIENCE

Department of Physics

University of Manitoba

Winnipeg, Canada

THE UNIVERSITY OF MANITOBA

FACULTY OF GRADUATE STUDIES

*****

COPYRIGHT PERMISSION PAGE

EVALUATION OF THE DOSIMETRIC ACCURACY IN THE PRESENCE OF INHOMOGENEITIES OF TWO COMMERCIAL ELECTRON PLANNING SYSTEMS

BY

James Beck

A Thesis/Practicum submitted to the Faculty of Graduate Studies of The University of Manitoba in partial fulfillment of the requirements of the degree of

Master of Science

Abstract

The generally accepted level of dosimetric accuracy for the planning of radiation treatments is ± 5 %. Presented in this thesis is an evaluation of the quality of the dosimetric predictions generated by the Focus (version 2.5 - Computerized Medical Systems) and Helax-TMS (version 4.1 - MDS Nordion) electron planning systems in the presence of inhomogeneities.

The dosimetric accuracy in a water equivalent phantom containing cylindrical or slab-shaped inhomogeneities was investigated for nominal beam energies of 9 MeV and 18 MeV, and field sizes of 10 cm x 10 cm and 15 cm x 15 cm. Both air and aluminum inhomogeneities were investigated. A novel PMMA phantom was designed, and used experimentally to verify the accuracy of EGS4 Monte Carlo dose calculations in the presence of these inhomogeneities. The accuracy of treatment planning predictions was then established by comparison with Monte Carlo calculations.

Both treatment planning systems exhibited a decrease in calculation accuracy as inhomogeneity thicknesses were increased. Distributions predicted for 15 cm x 15 cm fields were found to exhibit accuracies and trends similar to those predicted for 10 cm x 10 cm fields of the corresponding energy. Overall, neither treatment planning system was found to generate consistently accurate dose predictions beneath the inhomogeneities considered in this study. Dosimetric inaccuracies in excess of 10 % of the normalization dose were frequently observed for both slab-shaped and cylindrical inhomogeneity geometries. The only dose distributions found to exhibit continual agreement with Monte

Carlo results within the therapeutic range were the 18 MeV Focus predictions beneath air slabs (Maximum deviation < 3 % of normalization dose), and the 18 MeV Helax predictions beneath aluminum slabs (Maximum deviation < 4 % of normalization dose). No straightforward interpretation of the restricting approximations implemented by the Focus and Helax electron dose calculation algorithms could adequately explain the observed discrepancies between prediction and theory.

Acknowledgments

I would like to thank my advisors, Dr. John Lewis and Dr. Stephen Pisotorius, for their time, their instruction, and their motivation. Their experience in the field proved to be invaluable.

I would also like to thank all those who read this thesis and offered their criticisms and comments. This includes my thesis committee: Dr. John Lewis, Dr. Stephen Pistorius, Dr. Jim Butler, Dr. Norm Davison, and Dr. Daniel Rickey. It also includes Dr. Boyd McCurdy and Dr. Keith Furutani.

I am indebted to Dr. John Lewis and Dr. Boyd McCurdy for their work generating phase space files for the various energies and field sizes considered in this work. Access to these data allowed me to perform realistic simulations when I was still a relative newcomer to Monte Carlo methods.

Thanks to Chad Harris of Medical Devices for constructing the phantom used in this work.

I am grateful to my fellow students: Kyle Malkoske, Heather Andres, and Niranjan Venugopal. They were willing to share in my frustrations in spite of their own.

Lastly, I thank my wife Susan. She has struggled to maintain my sanity, and I am grateful for her patience during those intervals when she was unable to do so.

Table of Contents

List of Figures

List of Tables

1 Introduction

Radiation therapy has proven to be one of the most effective methods of cancer treatment available. This is because cancer cells can be killed or sterilized if they receive a sufficient radiation dose. Unfortunately, the same is true for normal tissues. Hence, the optimum radiotherapy treatment should maximize the dose delivered to cancer cells while minimizing the dose received by healthy tissues. The improved implementation of these principles serves as the motivation for many of the most modern advancements in treatment technology. It is of critical importance that an accurate representation of the expected dose distribution within a patient is obtained prior to treatment.

The dose delivered to a given tissue is defined as the amount of energy deposited there by the applied radiation, divided by the tissue mass. For example, when 1 Joule (J) of energy is absorbed by 1 kilogram (kg) of material, a total dose of 1 Gray (Gy) has been delivered. The problem of predicting the patient dose distribution depends on the way that a given radiation beam deposits its energy within a particular patient. This will depend on the type of radiation used as well as the anatomy of the treatment site and surrounding tissues.

Many different types of ionizing radiation beams have been used for radiotherapy. Some examples include: photons, electrons, protons, neutrons, and pions. These types of beams may be divided into two classes. If a beam particle is charged, it falls into the category of directly ionizing radiation. Uncharged beam particles are referred to as

indirectly ionizing. A radiation dose is deposited by interactions between energized charged particles, and the particles which make up the medium being irradiated. A charged quantum of radiation is therefore capable of depositing its energy *directly* to the medium. A neutral quantum of ionizing radiation must first undergo a number of energy transfer interactions, whereby it passes its energy to charged particles which themselves go on to deposit the dose.

Relatively advanced treatment facilities are required in order to use proton, neutron, or pion beams. However, almost all radiotherapy treatment centers in North America have both photon and electron beams available. Being of two separate classes, electron and photon beams deposit dose very differently within a patient. Each modality exhibits characteristics which make it preferable in different situations. Photons are uncharged particles with zero mass. They are therefore able to penetrate deep into the patient, and can transfer their energy to charged particles over a large range of depths. These energized charged particles subsequently deposit dose within the patient.

Electrons have both charge and mass. They begin to undergo multiple interactions immediately upon entering the patient. Electrons are significantly less penetrating than photons of the same energy, and the electron fluence can be expected to decrease dramatically at depths greater than the electron range. Consequently, electron beams begin to deposit dose much closer to the patient surface than do photon beams, with a significantly more dramatic dose falloff beyond the depth of maximum dose (d_{max}). This behavior makes electron beams preferable to photon beams for the superficial

treatments often required in head and neck cancers, chest wall irradiation, and skin treatments.[1]

Curative radiotherapy treatments are usually designed for individual patients, and must therefore be tailored to each person's anatomy. Three dimensional treatment planning systems can use a set of computed tomography (CT) slices or selected contours to reconstruct an accurate computerized model of the patient. Different beam configurations are then investigated in an attempt to obtain the optimum patient dose distribution. Many combinations of beams may be used, each with a selected energy, field size, and source to surface distance (SSD). Each of these parameters will affect the pattern of dose deposition. Treatment planning systems make use of a set of approximate theoretical models and measured data in order to predict the resulting patient dose distribution.

Electrons, being very light charged particles, experience many Coulomb scattering events and may follow a wide variety of torturous paths while traversing an object. As a consequence, electron dose deposition is difficult to model analytically, particularly when the object irradiated is not homogeneous. Currently, the most accurate method of dose calculation is Monte Carlo simulation. With the Monte Carlo dose calculation technique, the paths of a large number of individual electrons are simulated, each being tracked until it is no longer capable of depositing a meaningful dose. Note that simulated electron tracks are not expected to represent the *actual* paths followed by the electrons within the patient. Rather, a large number of simulated electrons are

expected to yield an accurate statistical representation of the pattern of total dose deposition resulting from the actual treatment beam. Unfortunately this technique is often too time consuming for regular clinical use.[2]

This work examines the accuracy of electron dose calculations performed by two different treatment planning systems: Focus (version 2.5 - Computerized Medical Systems), and Helax-TMS (version 4.1 - MDS Nordion). Each of these treatment planning systems has been studied independently in the past[3,4], but the direct comparison presented in this work explores the differences between the algorithms implemented by Focus and Helax, and the resulting discrepancies in the calculated dose distributions. Doses were calculated in a water phantom containing either cylindrical or slab-shaped inhomogeneities. Both air and aluminum inhomogeneities were considered. These materials and geometries were suggested by Van Dyk et al.[5] as appropriate when evaluating the accuracy of electron dose calculations. Dosimetric predictions were computed along the central axis for both 9 and 18 MeV electron beams using field sizes of 10 cm x 10 cm and 15 cm x 15 cm. Of all the electron beams used clinically at CancerCare Manitoba, beam energies of 9 and 18 MeV were selected because they represent the most stable low and high energy beams. They are also similar in energy to the 10 and 20 MeV beams used by Shortt et al. [6] The selected field sizes correspond to those most commonly used for electron treatments at CancerCare Manitoba.

Central axis measurements were performed in an adjustable Polymethylmethacrylate (PMMA) phantom which was designed to model all the required

inhomogeneity geometries efficiently. Dose measurements were performed by loading LiF thermolumeniscent dosimeters (TLDs) into the phantom such that the measurement at any particular location was not influenced by the presence of TLDs at other depths. The corresponding dose distributions were then calculated by Monte Carlo simulation. These simulated results were verified to be nearly equivalent to experimental measurements.

Exploiting the observed reliability of Monte Carlo dosimetry, the accuracy of each dose distribution predicted by Focus and Helax for each inhomogeneous water based phantom was evaluated through a comparison with Monte Carlo calculations. Quantitative similarities between Monte Carlo calculations and treatment planning predictions were used to rank each distribution produced by Focus and Helax either as a pass, as indeterminate, or as a failure. An identical ranking procedure was followed for each combination of inhomogeneity, beam energy, and field size. It is believed that clinical results may improve as a result of the identification of the strengths and weaknesses in these treatment planning systems.

2 Theory

The primary objective of this work is a comparative analysis of the performance of the Helax and Focus treatment planning systems. Both of these systems make use of pencil beam algorithms for electron dose calculation. According to this formalism, a broad beam of radiation is considered to be composed of a continuum of pencil beams. Initially each of these pencil beams has an infinitesimal cross section. As the pencils traverse a medium, they broaden, and begin to overlap. The total dose deposited at a particular location within an irradiated phantom is determined by adding up the dose contribution from each pencil beam at that point.

Pencil beam algorithms have been used successfully to determine the dose deposited by photon beams.[7] They enable differing field sizes and beam modulations to be accounted for in a straightforward fashion. When predicting the dose deposited in the presence of inhomogeneities, pencil beams are scaled according to broad beam dose measurements.[8] One of the most well known shortcomings of the pencil beam approach is its reliance upon the semi-infinite slab approximation. Under this approximation all electrons represented by a given pencil beam are treated as if they encounter only the medium traversed by the central ray of the pencil. The breakdown of this assumption becomes increasingly likely when a large amount of scattering takes place. Hence pencil based algorithms are expected to yield considerably less accurate predictions for electrons than they do for photons. This work is an investigation of those inaccuracies.

Although both Focus and Helax calculate electron doses using similar algorithms, their predictions are often incompatible. It is therefore important to understand how these treatment planning systems implement their algorithms. Of particular interest is the way that Focus and Helax predict pencil broadening with depth in an inhomogeneous phantom, and the approximations involved. Sections 2.1 and 2.2 describe the pencil beam algorithms implemented by Helax and Focus respectively. A comparison between these two approaches is then presented in section 2.3. The remaining sections of this chapter describe the physics and implementation of the Monte Carlo simulations used in this work.

2.1 Helax Dose Formalism

Electron doses calculated by Helax are evaluated using a pencil beam approach developed by Lax and Brahme.[9,10,11] In this section, the important aspects of this approach will be presented. Each pencil beam is characterized by a kernel which describes the fraction of energy deposited per unit volume (or mass) in the surrounding region. Pencil beam kernels have been calculated by Helax using the EGS4 Monte Carlo code by simulating the dose deposited by a narrow beam of energy E, normally incident upon a semi-infinite block of water. Following the work of Lax and Brahme [10] a linear superposition of three Gaussians is used to parameterize the radial variation of each pencil kernel at various depths. This parameterization is expressed symbolically in

equation (2.1).

$$\frac{p_{MC}}{\rho}(r) = \sum_{i=1}^{3} \frac{C_i}{\pi a_i^2} e^{-(r/a_i)^2} \qquad (2.1)$$

By tabulating the fitting parameters (C_i and a_i) for various beam energies and penetration depths, Helax has amassed a library of pencil kernels describing dose deposition in water.

The Fermi Eyges theory of radiation transport provides a mathematical description of the radial and angular broadening of an electron pencil beam due to interactions within the medium traversed. Helax uses Fermi Eyges theory in order to determine how a homogeneous pencil kernel expressed by equation (2.1) can be scaled to take a particular inhomogeneous geometry into account. The related equations may be expressed for a multi-layer geometry as shown below.[1] These equations have been written for a geometry consisting of n slabs perpendicular to the z axis, with each slab indexed by the letter i.

$$\overline{\theta^2}(z_n) = \overline{\theta^2}(z_{n-1}) + T_n\left(z_n - z_{n-1}\right)\left\{1 + k\sum_{i=1}^{n-1} S_i\left(z_i - z_{i-1}\right) + \frac{k}{2} S_n\left(z_n - z_{n-1}\right)\right\} \qquad (2.2)$$

---

1 Equations 2.2 - 2.4 are consistent with equations 4.3 - 4.5 in the Helax manual [11]. In order to make these equations consistent with those developed by Lax and Brahme [9] the stopping power in layer i (S_i) should be divided by the corresponding beam energy (E_i). The reason for this discrepancy was not resolved.

$$\overline{r\theta}(z_n) = \overline{r\theta}(z_{n-1}) + \overline{\theta^2}(z_{n-1})(z_n - z_{n-1}) + T_n \frac{(z_n - z_{n-1})^2}{2}\left\{1 + k\sum_{i=1}^{n-1} S_i(z_i - z_{i-1}) + \frac{k}{3}S_n(z_n - z_{n-1})\right\} \quad (2.3)$$

$$\overline{r^2}(z_n) = \overline{r^2}(z_{n-1}) + 2\overline{r\theta}(z_{n-1})(z_n - z_{n-1}) + \overline{\theta^2}(z_{n-1})(z_n - z_{n-1})^2 + T_n \frac{(z_n - z_{n-1})^3}{3}\left\{1 + k\sum_{i=1}^{n-1} S_i(z_i - z_{i-1}) + \frac{k}{4}S_n(z_n - z_{n-1})\right\} \quad (2.4)$$

Where z_n is the depth of the slab of interest, $\overline{\theta^2}$ and $\overline{r^2}$ describe the respective mean squared angular and radial spread of the pencil beam, and $\overline{r\theta}$ expresses their covariance. Here S_n is the total linear stopping power at a depth z_n, and T_n is the linear scattering power at a depth z_n. The constant k is determined using the assumed exponential relationship between the energy (E) and the scattering power (T) shown in equation (2.5).

$$T \propto E^{-k} \quad (2.5)$$

Helax uses a value of 1.85 for k.[11]

Following the approach taken by Lax and Brahme [9], two convenient depth related quantities are determined. These are: the fractional CSDA range (ξ_0) and the effective depth (ξ_{Rp}).

$$\xi_0(z_n) = \sum_{i=1}^{n} \frac{z_i - z_{i-1}}{R_{0,i}} \qquad (2.6)$$

$$\xi_{R_p}(z_n) = \sum_{i=1}^{n} \frac{z_i - z_{i-1}}{R_{p,i}} \qquad (2.7)$$

Where $R_{0,i}$ and $R_{p,i}$ are the CSDA and practical ranges in the medium making up slab i respectively.

Using the semi-infinite slab approximation, equation (2.2) is consulted to determine the mean square scattering angle as a function of depth through the geometry of interest. ξ_0 is then used to calculate E_{eff}, the energy of the pencil beam which would have exhibited the same mean square scattering angle after traveling an effective depth ξ_{Rp} through water.

$$E_{eff} = \left\{ \frac{qZ_w(1+\delta)}{\overline{\theta^2} - \overline{\theta_0^2}} \xi_0 - E_a \right\} \Bigg/ \left\{ 1 - \frac{cqZ_w}{\overline{\theta^2} - \overline{\theta_0^2}} \delta \xi_0 (Z_w + 4) \right\} \qquad (2.8)$$

Here Z_w is the effective atomic number of water, E_a is an energy related constant, and both c and q are non-trivial constants taken from Lax and Brahme [9]. The parameter δ is defined as:

$$\delta = \frac{k\xi_0}{2} \quad (2.9).$$

When Helax evaluates the effective energy it assumes that the initial mean squared scattering angle ($\overline{\theta_0^2}$) is zero.

One of the major limitations of the Fermi Eyges theory is that it describes a perpetually broadening pencil beam and does not take range straggling into account. Helax adjusts the mean square radius of the pencil beam calculated by equation (2.4) using a range straggling correction factor ($C_{straggl}$).

$$r_{corr}^2 = C_{straggl}\overline{r^2} \quad (2.10)$$

The parameterization of $C_{straggl}$ is accomplished using a comparison between the widths of Fermi Eyges and Monte Carlo pencil kernels for a homogeneous water phantom. Helax performs this parameterization using a complex function of beam energy (E) and effective depth in water (ξ).

$$C_{straggl}(E,\xi) = \frac{1 + f_1(E)\cdot\xi + f_2(E)\xi^2 + f_3(E)\xi^3}{1 + \exp\left[10\left(\xi - f_4(E)\right)\right]} + f_5(E)\left(1 - \frac{1}{1 + \exp\left[10\left(\xi - f_4(E)\right)\right]}\right) \quad (2.11)$$

where

$$\xi_{R_p,H_2O} = \xi(z) = \frac{z}{R_{p,H_2O}} \qquad (2.12)$$

The parameters denoted by f_n (n = 1→5) represent polynomials in E. Helax specifies the coefficients of these polynomials to 5 significant figures.[11] When computing the straggling correction factor for a treatment plan, Helax uses E_{eff} rather than E, and ξ_{Rp} rather than ξ. These dependencies are shown explicitly in the following equation.

$$r^2_{Tx,corr} = C_{straggl}(E_{eff}, \xi_{R_p})\overline{r^2} \qquad (2.13)$$

The corrected pencil beam radius is then used to scale the homogeneous water kernels represented by equation (2.1). The scaled kernels are considered suitable for the inhomogeneities present in the treatment being planned. This kernel scaling is accomplished using the parameter λ defined as

$$\lambda = \frac{\sqrt{r^2_{Tx,corr}}}{r^{MC}_{1/e}} \qquad (2.14),$$

where $r^{MC}_{1/e}$ is the 1/e radius of the parameterized Monte Carlo distribution. The scaled pencil kernel may then be represented as

$$\frac{p_{TMS}}{\rho} = \sum_{i=1}^{3} \frac{C_i}{\pi\left(\lambda a_i\right)^2} e^{-\left(r/\lambda a_i\right)^2} \qquad (2.15).$$

E_{eff} and ξ_{Rp} are used to select the appropriate pencil kernel (C_i and a_i) for use at each depth within the patient.

Fermi Eyges theory is also used to predict the radial and angular broadening which occurs while the beam traverses the air gap between the collimator and the patient surface. Radial broadening in the air is assumed to be negligible near the beam center, but angular broadening is not.

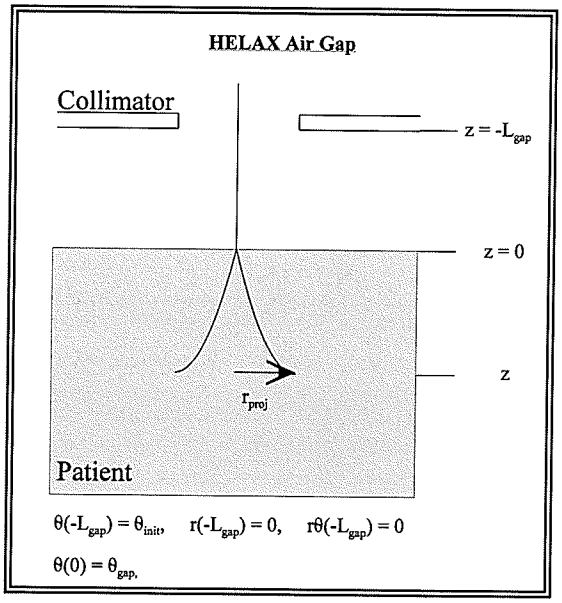

Figure 2.1 The treatment of air gap broadening by Helax-TMS. This figure was adapted from Helax fig. 4-5.[11] The curved path within the patient is intended to represent the lateral broadening described by equation (2.2)

The angular broadening at the position of the collimator is designated by $\theta_{init.}$

While traversing a distance L_{gap} from the collimator to the patient surface, the angular broadening will increase from θ_{init} to some larger value (θ_{gap}) according to equation (2.2). Thus, at the patient surface, the pencil beam is considered to have an initial angular spread of θ_{gap}. As a result of the presence of this air induced *angular* broadening, equation (2.4) predicts an increase in the *radial* broadening of the pencil beam such that r increases from zero to r_{proj} at a depth of z.

$$r_{proj}^2 = 2z\overline{r\theta}_{gap} + z^2\overline{\theta^2}_{gap} \qquad (2.16)$$

The net effect of interactions in the air gap and interactions in the medium may be determined using a convolution. The resulting pencil kernel is

$$\frac{p_{TMS}}{\rho} = \sum_{i=1}^{3} \frac{C_i}{\pi\left(\left(\lambda a_i\right)^2 + r_{proj}^2\right)} e^{-r^2/\left(\left(\lambda a_i\right)^2 + r_{proj}^2\right)} \qquad (2.17).$$

When modeling the effects of the air gap near the penumbra, radial broadening can no longer be ignored. Assuming an initial pencil radius of $\overline{r}_{gap}$ at the patient surface and taking the convolution yields

$$\frac{p_{TMS}}{\rho} = \sum_{i=1}^{3} \frac{C_i}{\pi\left(\left(\lambda a_i\right)^2 + r_{proj}^2 + \overline{r^2}_{gap}\right)} e^{-r^2/\left(\left(\lambda a_i\right)^2 + r_{proj}^2 + \overline{r^2}_{gap}\right)} \qquad (2.18).$$

Consider a point P located in a plane at a depth z_n within the patient. In order to calculate the dose at P, Helax assembles a series of concentric annular rings in the plane around P and divides them into segments. Rather than integrating over every pencil kernel in the entire plane, one kernel is assigned to each segment, and the dose contribution to P is added up one integrated segment at a time. More specifically, the absorbed dose due to segment k is calculated as

$$D_k = w_k \frac{D(z_{s,k})\Phi_k}{\iint\limits_{\substack{characterization \\ field}} \frac{p}{\rho}(r,\alpha)r \cdot drd\alpha} \iint\limits_{segment\ k} \frac{p}{\rho}(r,\alpha)r \cdot drd\alpha \qquad (2.19).$$

Here Φ_k is the electron fluence directed toward segment k, r and α are the polar coordinates in the plane at z_n, and w_k is a segment weighting factor used to take field shape into account. $z_{s,k}$ denotes the water equivalent distance which corresponds to a depth z_n within the phantom, and is calculated as

$$z_{s,k} = \sum_{i=1}^{n} \left(z_i - z_{i-1}\right) \frac{S_i}{S_{H_2O}} \qquad (2.20).$$

$D(z_{s,k})$ represents the dose deposited to a water segment at a depth $z_{s,k}$, and is determined from a bank of measured depth dose curves provided by the user. The measured dose includes a contribution from contaminant photons. This is the only consideration that

Helax gives to contaminant photons when calculating the dose from an electron beam.

2.2 Focus Dose Formalism

The physics of the Focus-CMS approach for electron dose calculation is based primarily on the Hogstrom pencil beam method.[12,13] Both electrons and contaminant photons deposit dose in an electron beam treatment. Focus calculates the dose contribution from each of these sources separately, and then adds them up to determine the total dose.

$$D(x,y,z) = D_e(x,y,z) + D_\gamma(x,y,z) \qquad (2.21)$$

The first step is the characterization of the relative intensity of a pencil beam located at position (x,y) in the field. Even directly beneath the collimator opening, the beam intensity distribution is not perfectly uniform, nor does it drop immediately to zero at the field boundary. Hence, the beam intensity is not well characterized by a square modulating function. Focus uses the function shown as C(x,y) in equation (2.22) to describe the beam intensity across the collimator plane as a function of distance from each set of collimating jaws. The center of the field is taken to be the origin of the xy plane.

$$C(x,y) = \frac{1}{4}\left\{F(x+\frac{W}{2}) - F(x-\frac{W}{2})\right\}\cdot\left\{F(y+\frac{L}{2}) - F(y-\frac{L}{2})\right\} \quad (2.22)$$

Where W and L are the width and length of the field respectively. F is a function which exhibits the following behavior.

F(arg) = -1 for arg < -1.5 cm

F(arg) = 0 for arg = 0.0 cm

F(arg) = +1 for arg > 1.5 cm

From this definition it can be seen that the intensity modulation factor C(x,y) varies from a maximum of 1 to a minimum of 0.

Focus assumes that the electron transmission is zero beneath a block, and unity if no block is present. This transmission function, $T_e(x,y)$, is clearly not valid for contaminant photons present in the electron beam, and it becomes necessary to treat electrons and contaminant photons separately. Thus the intensity of the electron component of the beam is modulated by $I_e(x,y)$, and that of the contaminant photon component is modulated by $I_\gamma(x,y)$.

$$I_e(x,y) = C(x,y)\cdot T_e(x,y) \quad (2.23)$$

$$I_\gamma(x,y) = C(x,y) \cdot T_\gamma(x,y) \qquad (2.24)$$

As developed above, $I_e(x,y)$ describes the electron intensity distribution at the collimator. Focus extends the electron intensity modulation factor down into the patient by including the radial smearing which occurs at depth as a result of the air traversed between the collimator ($z = -L_{gap}$) and the patient surface ($z = 0$). Radial smearing resulting from multiple coulomb scattering within the patient is not considered until much later.

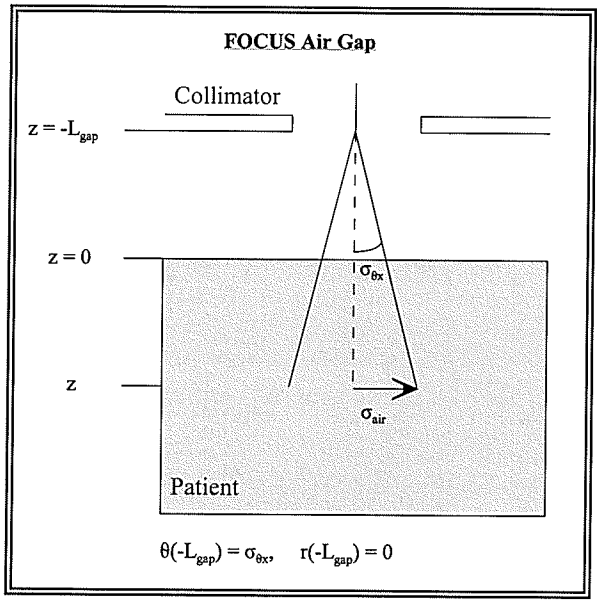

Figure 2.2 The treatment of air gap broadening by Focus-CMS

The initial angular spread at the collimator surface ($\sigma_{\theta x}$) is calculated using the lateral spread of measured air profiles. Starting with $\sigma_{\theta x}$, Focus uses a simple

trigonometric relation and small angle approximation to determine the subsequent *radial* broadening (σ_{air}) at a depth z within the patient. This approach is illustrated in figure 2.2

$$\sigma_{air}(z) = Tan(\sigma_{\theta x})\left(L_{gap} + z\right) \approx \sigma_{\theta x}\left(L_{gap} + z\right) \qquad (2.25)$$

A normalized Gaussian exhibiting a standard deviation of $\sigma_{air}(z)$ is then convolved with $I_e(x,y)$ to give $I_{air}(x,y,z)$:

$$I_{air}(x,y,z) = \frac{1}{2\pi\sigma_{air}^2(z)} \int_{L(z)} \int_{W(z)} I_e(x',y') \exp\left[-\frac{(x'-x)^2 + (y'-y)^2}{2\sigma_{air}^2(z)}\right] dx'dy' \qquad (2.26).$$

The limits of integration extend over the field width and length at depth. In order to improve the calculation efficiency, this convolution is actually evaluated using a summation of error functions:

$$I_{air}(x,y,z) = \frac{1}{4} \sum_{i=\frac{-W(z)}{2}-x-2cm}^{\frac{W(z)}{2}-x+2cm} \sum_{j=\frac{-L(z)}{2}-y-2cm}^{\frac{L(z)}{2}-y+2cm} I_e(x_i,y_j) \cdot \left\{erf\left[\frac{x_i + \Delta x/2}{\sqrt{2\sigma_{air}(z)}}\right] - erf\left[\frac{x_i - \Delta x/2}{\sqrt{2\sigma_{air}(z)}}\right]\right\} \cdot \left\{erf\left[\frac{y_j + \Delta y/2}{\sqrt{2\sigma_{air}(z)}}\right] - erf\left[\frac{y_j - \Delta y/2}{\sqrt{2\sigma_{air}(z)}}\right]\right\} \qquad (2.27).$$

The limits of the summation have been adjusted to ensure that $I_e(x_i,y_j)$ is zero everywhere

outside of the summation. It should be noted that Focus evaluates all convolutions in this manner. However, for mathematical clarity only the integral version will be shown in the following equations.

Focus proceeds by calculating the central axis term, $G_{H2O}(0,0,z_{eff})$. This term represents the electron dose which would have been measured along the central axis of a water phantom in the absence of radial smearing. It is calculated by dividing the *electron* percentage depth dose in water by a quantity equal to the corresponding fraction of the dose which is permanently scattered away from the central axis. The Focus manual [12] writes the central axis term as

$$G_{H_2O}(0,0,z_{eff}) = \frac{PDD_{H2O}(0,0,z_{eff}) - D_{\gamma,H_2O}(0,0,z_{eff})}{\frac{1}{2\pi\sigma^2_{H_2O}(z_{eff})}\int_{L(z_{eff})}\int_{W(z_{eff})} I_{e,H_2O}(x',y')\exp\left[-\frac{(x')^2+(y')^2}{2\sigma^2_{H_2O}(z_{eff})}\right]dx'dy'} \qquad (2.28).$$

Here the electron dose at a water equivalent depth of z_{eff} is determined from a percentage depth dose (PDD) measurement performed in a water tank. The equivalent depth is given by

$$z_{eff}(x,y,z) = \int_{-L_{gap}}^{z} \frac{S_{med}(x,y,z')}{S_{H_2O}(z')}dz' \qquad (2.29),$$

where $S_{med}(x,y,z')$ is the stopping power for the medium located at (x,y,z'), and $S_{H2O}(z')$ is

the stopping power at a depth z' in water.

As shown in the numerator of equation (2.28), the *electron* PDD_{H2O} along the central axis is determined by subtracting the corresponding *photon* dose component, $D_{\gamma, H2O}(0,0,z_{eff})$, from the measured $PDD_{H2O}(0,0,z_{eff})$ data. For effective depths less than the practical range (R_p), $D_{\gamma, H2O}(0,0,z_{eff})$ is given the same value as $PDD_{H2O}(0,0,R_p+5mm)$. For effective depths beyond R_p, $D_{\gamma, H2O}(0,0,z_{eff})$ is set equal to $PDD_{H2O}(0,0,z_{eff})$ and the central axis term becomes zero.

The term shown in the denominator of equation (2.28) is a combination of the intensity modulation factor corresponding to the setup used when PDD_{H2O} was measured ($I_{e,H2O}$), and a distribution describing the radial smearing due to interactions in the air and multiple coulomb scattering (MCS). The width of the radial smearing function is characterized by σ_{H2O}.

$$\sigma_{H_2O}(z_{eff}) = \sqrt{\sigma^2_{air}(z_{eff}) + (fmcs)\left(\sigma^2_{MCS}(z_{eff})\right)} \qquad (2.30)$$

The calculation of $\sigma^2_{air}(z_{eff})$ is performed according to equation (2.25). The multiple Coulomb scattering contribution (σ_{MCS}) is calculated here for a water phantom using the following equation from Fermi Eyges theory:[14]

$$\sigma^2_{MCS}(x,y,z_{eff}) = \frac{1}{2}\int_{-L_{gap}}^{z}(z-z')^2\, T(z_{eff}(x,y,z'))dz' \qquad (2.31).$$

Here $T(z_{eff})$ is the linear angular scattering power. The linear angular scattering power is more properly a function of the mean energy (E), but may be expressed as a function of z_{eff} using the following approximate relationship:

$$E(z_{eff}) = E(0)\left(1 - \frac{z_{eff}}{R_p}\right) \qquad (2.32).$$

Equation (2.31) leads to an underestimation of σ_{MCS}. fmcs is a multiplicative correction factor designed to compensate for this effect. Hogstrom recommends an fmcs value of 1.4. [15] Focus allows the user to modify fmcs to obtain optimal agreement with measured isodoses. [12]

Focus then combines the central axis term with $I_{air}(x,y,z)$ and an inverse square correction factor.

$$I(x,y,z) = I_{air}(x,y,z)G_{H_2O}(0,0,z_{eff}(x,y,z))\left(\frac{SSD + z_{eff}(x,y,z)}{SSD + z}\right)^2 \qquad (2.33)$$

It is this new parameter, I(x,y,z), which is convolved with an inhomogeneity dependent MCS smearing Gaussian to calculate the electron component of the total dose ($D_e(x,y,z)$):

$$D_e(x,y,z) = \int_{-\infty}^{\infty}\int_{-\infty}^{\infty} I(x',y',z)\frac{1}{2\pi \cdot fmcs \cdot \sigma^2_{MCS}(x',y',z)} \cdot \exp\left[-\frac{(x-x')^2+(y-y')^2}{2\cdot fmcs\cdot\sigma^2_{MCS}(x',y',z)}\right]dx'dy' \quad (2.34).$$

Here σ_{MCS} is calculated for the actual phantom using equation (2.31).

Focus calculates the photon component of the total dose ($D_\gamma(x,y,z_{eff})$) using equation (2.35).

$$D_\gamma(x,y,z) = PDD_{H_2O}(0,0,\phi)\cdot I_\gamma(x,y)\cdot\left(\frac{SSD+z_{eff}(x,y,z)}{SSD+z}\right)^2 \cdot\frac{1}{4}\frac{\left(erf\left[\frac{W/2+x}{\sqrt{2}\sigma_{air}}\right]-erf\left[\frac{W/2-x}{\sqrt{2}\sigma_{air}}\right]\right)\left(erf\left[\frac{L/2+y}{\sqrt{2}\sigma_{air}}\right]-erf\left[\frac{L/2-y}{\sqrt{2}\sigma_{air}}\right]\right)}{erf\left[\frac{W/2}{\sqrt{2}\sigma_{air}}\right]\cdot erf\left[\frac{L/2}{\sqrt{2}\sigma_{air}}\right]} \quad (2.35)$$

Here φ is defined as:

$\varphi = R_p + 0.5$ mm. if $z \le R_p + 0.5$ mm

$= z$ if $z > R_p + 0.5$ mm.

The total dose is then obtained by summing the photon and electron components.

2.3 Comparison and Limitations of the Focus and Helax Algorithms

As evidenced by the previous two sections, there are considerable differences between the pencil based dose calculation algorithms used by Focus and Helax. There are also several similarities. For example, both use the angular broadening which occurs in the air gap between the collimator and the patient in the determination of the corresponding radial broadening at depth. Focus specifies the initial angular distribution at the collimator using $\sigma_{\theta x}$, and extends this distribution into the patient. The corresponding radial broadening is then predicted at depth using a small angle approximation of $\mathrm{Tan}(\sigma_{\theta x})$. Helax begins with an initial angular distribution, specified by θ_{init}. However Helax uses Fermi Eyges theory to take account of the evolution of this angle as the gap is crossed. Fermi Eyges theory is then used a second time to determine the radial broadening at depth within the phantom based on the calculated angular distribution at the patient surface.

The radial pencil broadening which results from interactions within the patient is also treated differently by Focus and Helax. Focus specifies radial broadening using σ_{MCS}, which is calculated directly from Fermi Eyges theory and does not include the effects of range straggling. Helax also uses Fermi Eyges theory to specify phantom induced radial broadening, but goes one step further and employs a range straggling correction.

Neither treatment planning system models large angle scattering very well. By

fitting a superposition of three Gaussians to Monte Carlo dose deposition kernels, Helax enables the large angle scattering contribution to the kernel edges to be accurately represented.[11] This is certainly more accurate than the single Gaussian that Focus uses to characterize pencil beam width. However, one must not lose sight of the fact that the Fermi Eyges treatment of radiation transport, which plays a crucial role in both treatment planning systems, is based upon an assumption of small scattering angles.

Another difference between these two treatment planning systems is their treatment of the dose deposited in an electron treatment by contaminant photons. Focus subtracts the photon contribution from the measured depth dose data, and uses the result to scale the electron pencil beams. The photon dose is then treated separately and added to the electron dose at the end of the calculation. Helax takes account of the dose contribution arising from contaminant photons by using unaltered depth dose data to scale pencil beams.

Perhaps the most severe limitation of both of these treatment planning systems is their reliance upon the semi-infinite slab approximation. Under this approximation all electrons represented by a given pencil beam are treated as if they encounter only the medium traversed by the central ray of the pencil. These concepts are illustrated in figure 2.3. As indicated in parts (A) and (B) of this figure, the semi-infinite slab approximation accurately predicts the broadening of a pencil beam when there is no lateral inhomogeneity variation. In part (C) however, over the depths for which the central ray is within the inhomogeneity, the entire beam broadens as if it has encountered this material.

This leads to an inaccurate representation of dose deposition for that portion of the beam on the right hand side, which has not traversed the inhomogeneity. In part (D) the opposite effect takes place. Here the central pencil ray does not interact with the inhomogeneity, and the entire pencil beam broadens as if the phantom were completely homogeneous. This is reasonable for the right half of the beam, but is clearly incorrect for the left. When predicting the total dose distribution, a continuum of pencil beams is considered to be incident at the phantom surface. When inhomogeneities are not infinite in lateral extent, adding up the contribution from pencil beams behaving as shown in parts (C) and (D) of figure 2.3 diminishes the effect of the inhomogeneity.

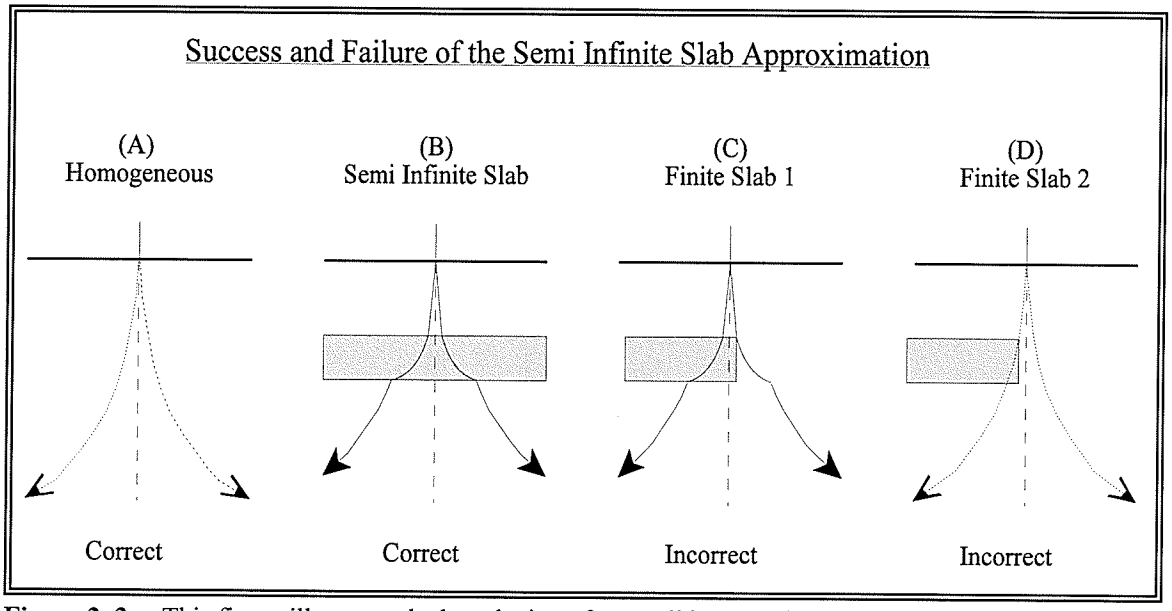

Figure 2. 3 This figure illustrates the broadening of a pencil beam as it passes through different phantom geometries.

The semi-infinite slab approximation becomes increasingly likely to fail when the scattering power and stopping power of the inhomogeneity material begin to differ significantly from that of the surrounding medium. The air and aluminum cylinders used in this work differ substantially from their water surroundings, and failure was anticipated in some degree.

When an inhomogeneity has a larger atomic number (Z) than its surroundings, it is expected that more electrons will scatter out of the inhomogeneity than will scatter in (the scattering power is proportional to Z^2). Hence there will be fewer electrons beneath a relatively high Z inhomogeneity than would have been present in a completely homogeneous phantom. This results in the production of a low dose region, or a cold spot. The reverse is true when the inhomogeneity has a lower atomic number than its surroundings. In this case in-scattering exceeds out-scattering and a hot spot is created. These concepts are illustrated in figure 2.4.

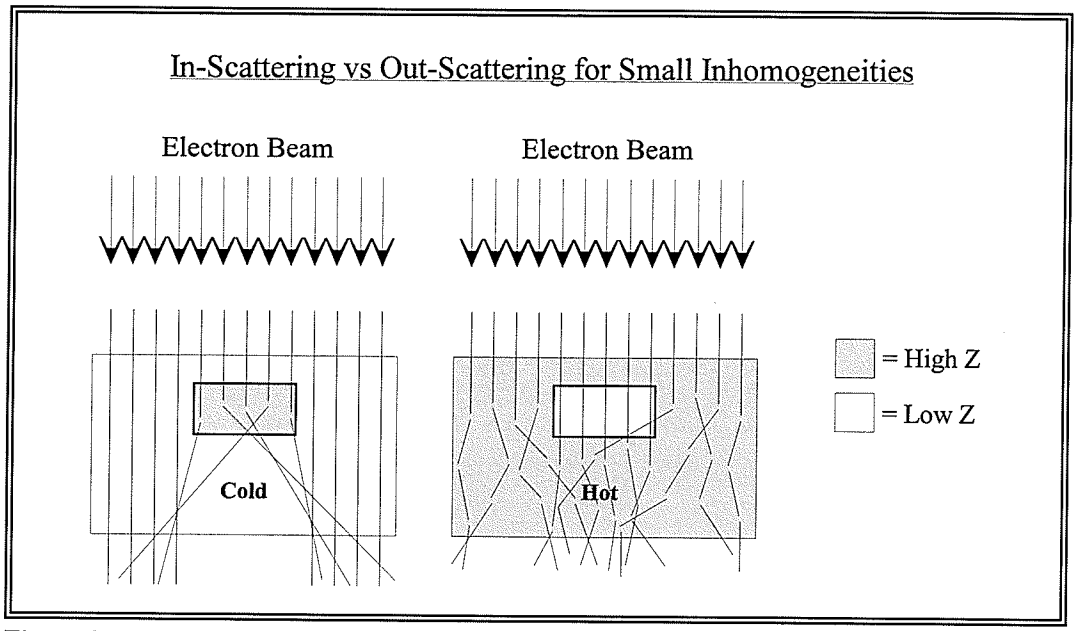

Figure 2. 4 An electron beam that encounters an inhomogeneity which has a higher atomic number than its surroundings will experience more out-scattering than in-scattering. This creates a cold spot directly below the inhomogeneity. The opposite is true for an inhomogeneity which has a lower atomic number than its surroundings.

2.4 EGS4 Monte Carlo Calculations

In Monte Carlo simulation the path and corresponding energy deposition of each individual quanta of radiation are simulated and tracked through a particular object. The simulated path is constructed by using random numbers to periodically select a physical interaction from a library of probability distributions. The specific effect that each selected interaction has on the simulated path is determined by theoretical equations and randomly sampled probability distributions.

The finite period of random number generators represents a fundamental limitation on the number of independent tracks that can be simulated. Very accurate results can be

generated when the number of independent tracks becomes large.

EGS4 (**E**lectron **G**amma **S**hower version **4**) is a Monte Carlo code used to simulate the radiative transport of electrons (e^-), positrons (e^+), and photons (γ). EGS4 is considered reliable over an energy range of 1keV to "several thousand" GeV for photons, and from 2 or 3 keV to "a few thousand GeV" for charged particles. [16] The code is written using a Fortran77 preprocessor known as Mortran (version 3). EGS4 uses RANMAR, a lagged Fibonacci pseudo random number generator with a period of 2^{144}.[17]

In order to simulate radiative transport through an object composed of a number of different materials, EGS4 must have access to a set of material dependent interaction probabilities. The PEGS4 (**P**reprocessor for **EGS4**) software may be used to generate these data for elements or mixtures using archived cross section data for elements with atomic numbers ranging from 1 to 100. Once this data file has been generated, it may be saved and accessed repeatedly. After EGS4 has located the required data for each medium present in the specified geometry, the transport of photons and electrons is initiated.

2.4.1 Photon Transport

Photons are present in an electron beam treatment as a result of initial beam contamination, bremsstrahlung radiation, and positron annihilation. An accurate Monte Carlo simulation of an electron beam must therefore also handle photon transport. EGS4 models the following interactions to determine the path traveled and the energy deposited by photons.[18,19]

- Coherent Scattering (γ + Atom → γ + Atom)
- Photoelectric Effect (γ + bound e^- → free e^-)
- Compton Effect (γ + lightly bound e^- → γ + free e^-)
- Pair Production (γ → e^- + e^+)

The contribution from each of these interactions to the total cross section is illustrated in figure 2.5 for a water phantom. These data were generated using a Mortran program called Examin to analyze the 700ICRU PEGS4 data file. The Examin software and 700ICRU data were provided with the EGS4 Monte Carlo package.

Once it has been determined that an interaction will occur, the PEGS4 data are consulted in order to select which specific interaction that will be. As a result of the relatively small contribution from coherent scattering, this interaction is usually ignored.

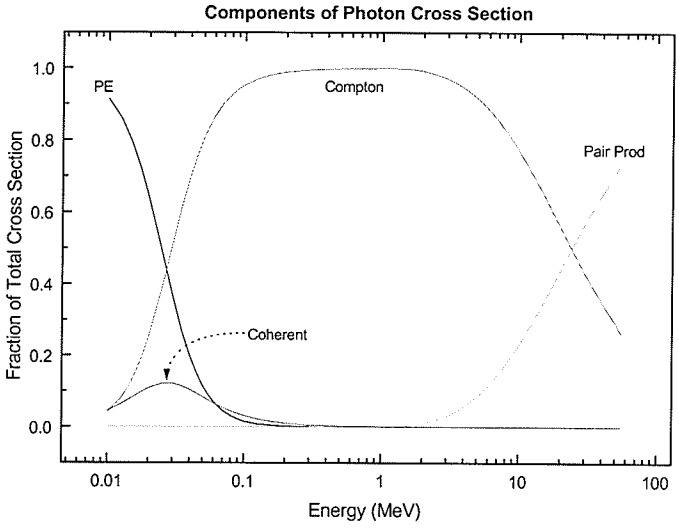

Figure 2.5 Contribution of photon interactions to the total cross section. AE = 0.700 MeV, AP = 0.01 MeV

Since the absolute magnitude of these cross sections is not exceedingly large, the total number of photon interactions is manageable, and each interaction may be treated discretely. The photon mean free path (λ) is used to determine the distance between successive interaction sites. More specifically, PEGS4 calculates λ as the reciprocal of the total macroscopic interaction cross section. The number of mean free paths (N_λ) traveled from one interaction site to the next is then determined by sampling from a distribution ($P(N_\lambda)$) which describes the probability that a photon will travel *less than* N_λ mean free paths without interacting:

$$P(N_\lambda) = 1 - e^{-N_\lambda} \qquad (2.36).$$

Once N_λ has been determined, the actual distance between photon interactions may be calculated by inverting the following equation.

$$N_\lambda = \int_{x_0}^{x} \frac{dx'}{\lambda(x')} \qquad (2.37)$$

Here x_0 is the location of the previous interaction and x is the position of the current interaction. $\lambda(x')$ is a function of the photon energy and the medium located at position x'. PEGS4 data files are consulted to obtain the mean free path as a function of energy and material. Figure 2.6 illustrates the photon mean free path for various materials. These data were extracted from the 700ICRU PEGS4 data files using the Examin software.

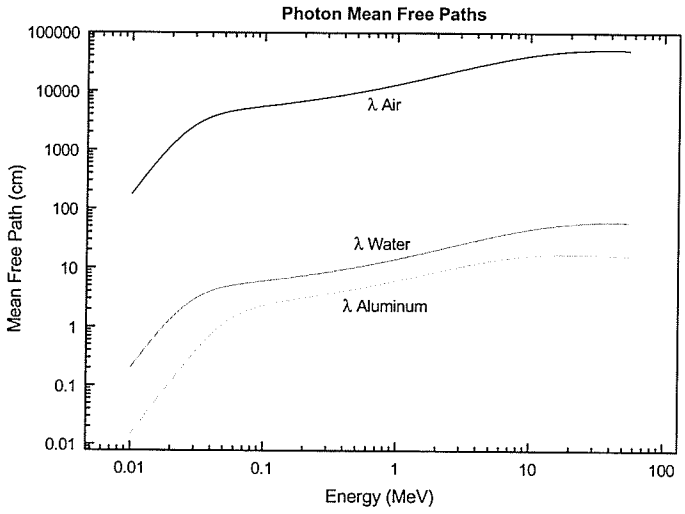

Figure 2.6 Mean free path between photon interaction sites in water, air, and aluminum. AE = 0.700 MeV, AP = 0.01 MeV

Each individual photon being tracked is followed only until it reaches a location where its energy falls below a user specified value (AP). All remaining energy is then considered to be deposited immediately.

2.4.2 Electron Transport

Electron interaction cross sections tend to diverge toward infinity as the electron kinetic energy approaches zero. Consequently, electrons undergo too many interactions to allow for discrete modeling. EGS4 employs a condensed history technique whereby a small number of 'catastrophic' interactions are treated individually, and the remaining 'non-catastrophic' interactions are considered collectively.

Catastrophic interactions are distinguished from non-catastrophic interactions using energy thresholds specified by the user. An interaction is considered catastrophic if it yields a charged particle with total energy greater than AE, or a photon with energy greater than AP. All remaining interactions are non-catastrophic.

The catastrophic interactions modeled by EGS4 are: [18, 19]

- large energy-loss Møller scattering $(e^- + e^- \rightarrow e^- + e^-)$
- large energy-loss Bhabha scattering $(e^+ + e^- \rightarrow e^+ + e^-)$
- hard bremsstrahlung $(e^{\pm} + \text{nucleus} \rightarrow e^{\pm} + \text{nucleus} + \gamma)$
- positron annihilation $(e^+ + e^- \rightarrow \gamma + \gamma)$.

The non-catastrophic interactions are: [18, 19]

- low energy-loss Møller scattering
- atomic excitation ($e^{\pm}$ + nucleus → $e^{\pm}$ + excited nucleus)
- soft bremsstrahlung
- elastic multiple scattering from atoms ($e^{\pm}$ + nucleus → $e^{\pm}$ + nucleus)

Energy losses arising from the first three non-catastrophic interactions are accounted for using the Beth-Bloch theory of charged particle energy loss.[20,21] That is, while traveling its convoluted path the electron is subjected to continuous energy loss, characterized by the restricted stopping power. Low energy-loss Møller scattering and atomic excitation contribute to the collisional component of the restricted stopping power while soft bremsstrahlung interactions make up the radiative component. The material and energy dependence of the restricted stopping power is obtained from PEGS4. Figure 2.7 illustrates the restricted stopping power as a function of energy for several materials of interest. These data were extracted from the 700ICRU PEGS4 data files using Examin.

Although multiple elastic scattering is always a non-catastrophic event, it cannot be treated in a continuous manner. The angle by which this interaction will alter the direction of the electron must be sampled randomly. Multiple elastic scattering is treated using Bethe's version of Molière scattering theory, which is reasonably accurate for both

large and small scattering angles.[22]

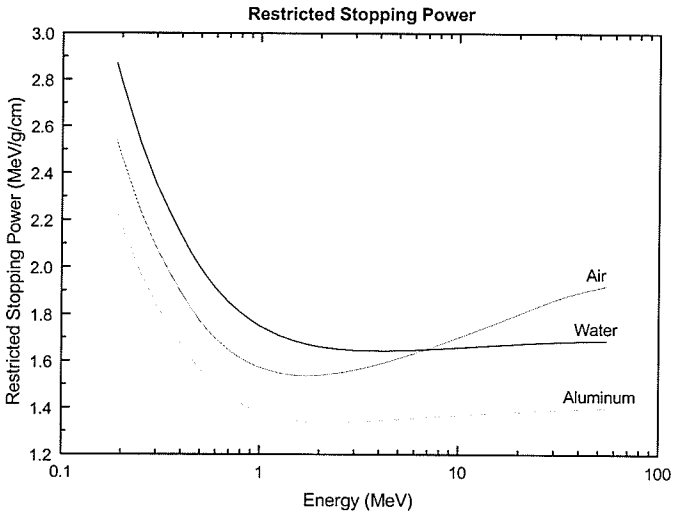

Figure 2.7 Restricted stopping power in water, air, and aluminum. AE = 0.700 MeV, AP = 0.01 MeV

As was the case for photons, electron interaction cross sections depend on particle energy and the materials encountered. Since electrons are considered to lose energy continuously when traversing a medium, *their* cross sections will vary continuously with path length. This complicates the calculation of the distance between discrete electron interactions. In EGS4 a fictitious null-interaction cross section ($\sigma_{fict}(x)$) is introduced such that the resulting total cross section ($\sigma_{t,fict}(x)$) is kept equal to the actual total cross section at the previous interaction site ($\sigma_{t,real}(x_0)$):

$$\sigma_{t,fict}(x) = \sigma_{t,real}(x) + \sigma_{fict}(x) = \text{constant} = \sigma_{t,real}(x_0) \qquad (2.38).$$

The *actual* mean free path between discrete interactions (λ_d) is determined from PEGS4 data. Figure 2.8 illustrates the energy dependence of λ_d for a variety of different materials. These data were generated from the 700ICRU PEGS4 data set using Examin. It should be noted that it is the *fictitious* mean free path corresponding to $\sigma_{t,fict}$ which is used to determine the distance to the next interaction.

Once the interaction site has been reached a random number is generated. If the generated number is *greater* than the ratio between $\sigma_{t,real}(x)$ and $\sigma_{t,fict}(x_0)$ the null-interaction is selected and the electron proceeds without energy loss or deflection. If the random number is *less* than this ratio one of the catastrophic interactions is selected.

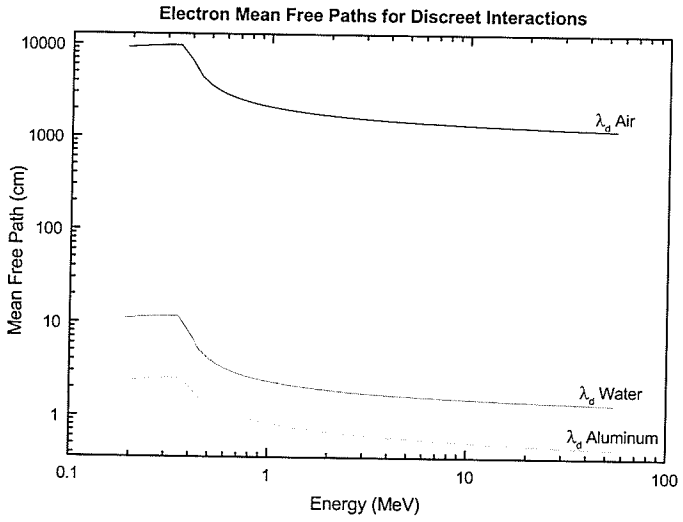

Figure 2.8 Mean free path between discrete interactions in water, air, and aluminum. AE = 0.700 MeV, AP = 0.01 MeV

The effect of both catastrophic and non-catastrophic interactions must be combined in order to simulate an actual electron path. As mentioned above, deflections in the path of an electron arising from multiple elastic scattering are randomly sampled from a probability distribution based on Bethe's version of Molière scattering theory.[22] Electrons are assigned a scattering angle after each of these interactions, between which they are assumed to travel straight lines. As with photons, the electron is only followed until its energy falls below a user specified value (AE), at which point all remaining energy is deposited.

Unlike the method used for catastrophic interactions, the step size between multiple elastic scattering events is not determined using a mean free path calculation. Frequently one specifies the step size by assigning a fixed value for the fractional energy loss per step. For this work, an algorithm know as PRESTA was used in conjunction with EGS4 in order to optimize the step sizes used.

2.4.2.1 PRESTA

One of the most important considerations in electron transport involves the determination of an appropriate distance by which multiple elastic scattering events should be separated. Small step sizes yield accurate results, but may be unnecessarily inefficient. Large step sizes certainly lead to faster calculations but are generally less accurate. PRESTA (**P**arameter **R**educed **E**lectron **S**tep **T**ransport **A**lgorithm) determines

the optimum step sizes during the Monte Carlo simulation, and increases calculation accuracy when using large step sizes.

The electron trajectory is constructed assuming a straight line path between multiple elastic scattering events. However, this results in an underestimation of the actual path traveled between interaction sites, which will most likely exhibit some curvature. Since the actual electron path length should be used when considering continuous energy losses, this curvature should be accounted for. The EGS4 path length correction is based on the approach of Messel and Crawford [23] which is itself rooted in the Fermi-Eyges theory of multiple scattering. The PRESTA path length correction (PLC) is based on Molière scattering theory and has been shown to be more accurate than the default method employed in EGS4.[24]

Very large step sizes can be used with the increased accuracy gained from the PLC. However, when an increased step size is used the space between the two bracketing interactions has replaced other multiple elastic scattering events. If explicitly considered, each of these dismissed events would have introduced another scattering angle and contributed to the deflection of the electron path. Hence, as very large step sizes are introduced, the lateral electron deflection will be underestimated. PRESTA includes a lateral correlation algorithm (LCA) which introduces an additional angular deflection to compensate for this effect.

When the straight line trajectory joining two interaction sites has not crossed any media boundaries, EGS4 assumes that the actual electron path has remained entirely

within the original medium, regardless of proximity to a material interface. When the interaction step occurs near a medium boundary, the curvature of the path that the electron actually follows may render this assumption false. The breakdown of this one-medium assumption becomes increasingly likely when large step sizes are considered. The boundary crossing algorithm implemented by PRESTA (BCA) compensates for this effect by forcing electron paths to exhibit small step sizes near material boundaries. Furthermore, an electron which is crossing a media boundary is forced to undergo an interaction at the interface.

2.4.3 Combined Transport

A photon, electron, or positron undergoing a discrete interaction may result in the production of a secondary source of radiation (particle or photon). This secondary radiation must also be tracked until the appropriate energy cutoff (AE or AP) has been reached. When a single quantum of primary radiation and all of its subsequent progeny have been followed to their energy cutoff values, one history is said to have been evaluated. A very large number of histories must be considered before an appreciable statistical accuracy will been obtained. December 19, 2001

2.4.4 The OMEGA-BEAM Software Package

The OMEGA-BEAM software package [25] contains a number of EGS4 based simulation codes. These codes use EGS4 for radiation transport, but provide the user with a more convenient interface for geometry specification. The following discussion will focus primarily on three such programs: DOSRZ, DOSXYZ, and BEAM.

2.4.4.1 Input Specifications

Geometrical definition of the object through which the simulation is to take place is different for DOSRZ, DOSXYZ, and BEAM. Despite this diversity, the different materials used to make up the phantom are specified in the same manner; a medium is selected from the PEGS4 database and assigned to a particular geometrical region. Once the phantom is defined, one must specify the source which will be irradiating it. The source composition and geometry are defined by IQIN and ISOURCE respectively. Sources used in this work include narrow electron pencil beams and phase space files which model clinical electron beams.

DOSRZ, DOSXYZ, and BEAM record the dose scored in selected regions of the object being irradiated. The accuracy of the dose recorded in each of these scoring voxels will depend on several parameters which influence the radiation transport directly. ESTEPE gives the user the option of specifying the fractional energy loss between

electron steps. A zero entry implies use of the default EGS4 step size algorithm. SMAX represents the maximum allowable step size between interactions. With the implementation of the PRESTA algorithm, the importance of ESTEPE and SMAX is diminished.

ECUT and PCUT represent the energies at which electron and photon tracks are terminated (respectively). Since a particle is considered to deposit all of its remaining energy into the scoring voxel in which it is terminated, the smaller these parameters are, the more accurate the pattern of dose deposition will be. For example, as ECUT is increased it becomes increasingly likely that a terminated electron would have penetrated into the next voxel. If ECUT is set to 700 keV, the transport of electrons will cease when their total energy falls below this value, leaving the electron with a kinetic energy less than 189 keV. Since the CSDA range of 189 keV electrons in water is about 0.41 mm, the remaining electron energy would have been deposited in a sphere smaller than 0.5 mm in radius. If ECUT or PCUT are less than their PEGS4 counterparts (AE and AP respectively), then these parameters will automatically be replaced in favor of the larger PEGS4 values. Decreasing the values of ECUT and PCUT increases the simulation time dramatically.

The total number of histories to be evaluated (NCASE) is of critical importance in any simulation. Increasing the number of histories will lengthen the simulation time. However, if the scoring volume remains constant, an increased number of histories will improve the statistical accuracy of the dose calculation. The statistical methods used to

calculate dose deposition are described in further detail in the following section.

2.4.4.2 Statistical Methods

When specifying the phantom geometry, the user selects the regions in which dose will be scored. For simplicity, the following discussion considers the calculation in only one such region. In DOSRZ, DOSXYZ, and BEAM, a simulation consisting of N histories is divided into n statistical batches. If the energy absorbed in this region volume from a single batch b is ε_b, then the total energy there absorbed (ε) is found by summing over all batches.

$$\varepsilon = \sum_{b=1}^{n} \varepsilon_b \qquad (2.39)$$

The average energy absorbed per batch ($\langle \varepsilon \rangle$) and the standard error of this quantity ($\sigma_{\langle \varepsilon \rangle}$) are then calculated.

$$\langle \varepsilon \rangle = \frac{\varepsilon}{n} \qquad \sigma_{\langle \varepsilon \rangle} = \sqrt{\frac{\sum_{b=1}^{n} \left(\varepsilon_b^2\right) - n\langle \varepsilon \rangle^2}{n(n-1)}} \qquad (2.40)$$

The validity of this statistical calculation depends upon the applicability of the central limit theorem, which is a reasonable approximation when the number of batches is

large.[26] Although DOSXYZ, DOSRZ, and BEAM default to ten batches, larger numbers are preferable. Each of these programs records the *total* energy absorbed in each region (ε). The associated error (σ_ε) is calculated as shown below.

$$\sigma_\varepsilon = n\sigma_{\langle\varepsilon\rangle} = \frac{\sigma_{\langle\varepsilon\rangle}}{\langle\varepsilon\rangle}\varepsilon \qquad (2.41)$$

These quantities are converted to units of dose by dividing by the total mass of the scoring region in question. The mass of each region is determined using the material density from the PEGS4 data file and the geometrical volume of the scoring region. Final results are reported per unit incident fluence in order to remove the dependence on the number of histories simulated.

2.4.4.3 DOSRZ

DOSRZ uses a right cylindrical coordinate system to specify the geometry of the phantom through which the simulation is to take place. Naturally this software is most useful when the phantom exhibits cylindrical symmetry.

The computer representation of the phantom may be constructed as follows. The z position of the uppermost portion of the phantom is declared, and then the location of successive slabs may be specified in one of two ways. The first method enables the user

to record the depth of each plane according its z coordinate. The second method enables the user to specify the total number of slabs, along with the corresponding thicknesses. Finally, radial boundaries are assigned. The result is a stack of concentric disks of a specified height, each of which is divided into a series of annular segments of a defined radial thickness. If desirable, the user can restrict the region of the phantom in which the dose will be scored.

One advantage of using DOSRZ is that upon simulation, the phantom geometry is immediately illustrated using a simple ASCII figure. This figure summarizes the geometry and material composition of the phantom in 2D. Another advantage associated with DOSRZ is that the user can request the output in a ready-to-plot format. This feature may be used to generate plots as a function of either depth or radius.

2.4.4.4 DOSXYZ

DOSXYZ uses a cartesian coordinate system to define the geometry of the phantom. This platform is best applied to situations exhibiting rectangular symmetry, and is somewhat less restrictive than DOSRZ.

Phantom definition is accomplished by dividing the phantom volume into a set of rectangular voxels and assigning a material to each. The voxel dimensions need not be uniform across the phantom. The user may then select the region of the phantom within which the dose will be scored. Typical simulation output will record the dose deposited

to each voxel in a given plane, one plane at a time. The disadvantage of this form of output is that the resulting file is often very large, and is difficult to interpret directly. However, the OMEGA-BEAM software package also includes a Mortran program called Statdose, which may be used to extract and plot data from this file along any ray within the calculation region.

2.4.4.5 BEAM

The BEAM program is used to simulate the evolution of a radiation beam as it progresses through the head of a linear accelerator. The output from this program is in the form of a phase space file, which contains position, energy, direction, charge, and history information for each quanta of radiation at one or more user defined planes in the simulation geometry. A phase space file which accurately characterizes the state of the accelerator beam at the phantom surface is the most realistic form of source input for DOSRZ and DOSXYZ.

When writing the BEAM input file, the geometries of the components which make up the accelerator head need to be specified. In order to simplify this process, BEAM includes a list of relevant component modules (CMs). The user may select an appropriate series of CMs from this list, and tailor each one for the geometry and material composition of the accelerator being used. All of the available CMs are described in detail in the BEAM users manual [25]. The CMs used in this work are listed below.

- SLABS — Used to create slabs perpendicular to the beam axis.
- FLATFILT — Used for stacks of truncated rotationally symmetric cones.
- CHAMBER — Used to characterize a parallel plate ionization chamber
- JAWS — Defines a pair of bars of specified thickness.
- APPLICAT — Constructs rectangular apertures of defined thickness and width.

The BEAM package contains graphics software which allows the user to view the specified accelerator geometry in 3D. One can also view the photon, electron, and positron tracks as they traverse the different components. This provides a useful visual verification that the simulation of the accelerator head has proceeded as expected.

2.4.5 Verification of Monte Carlo Calculations

A verification of the accuracy of EGS4 dosimetry in PMMA was be judged to be indicative of a similar accuracy for EGS4 calculations in water. This conclusion was based on the similarity of the radiation transport characteristics between these two media. This similarity is illustrated in figures 2.10 and 2.9 which show the components of the photon interaction cross section and the restricted stopping power respectively for these two media. These data were extracted from the 700ICRU PEGS4 data files using Examin.

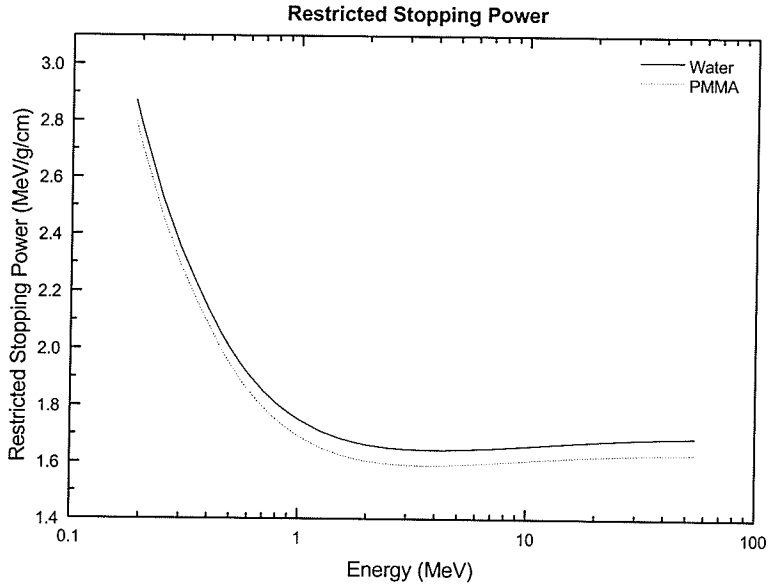

Figure 2. 9 The energy deposition characteristics of electrons in water (solid line) and PMMA (dotted line) are shown here. As a result of the similarity between these two data sets, our PMMA verification of EGS4 dosimetry was assumed to be applicable to water phantoms as well.

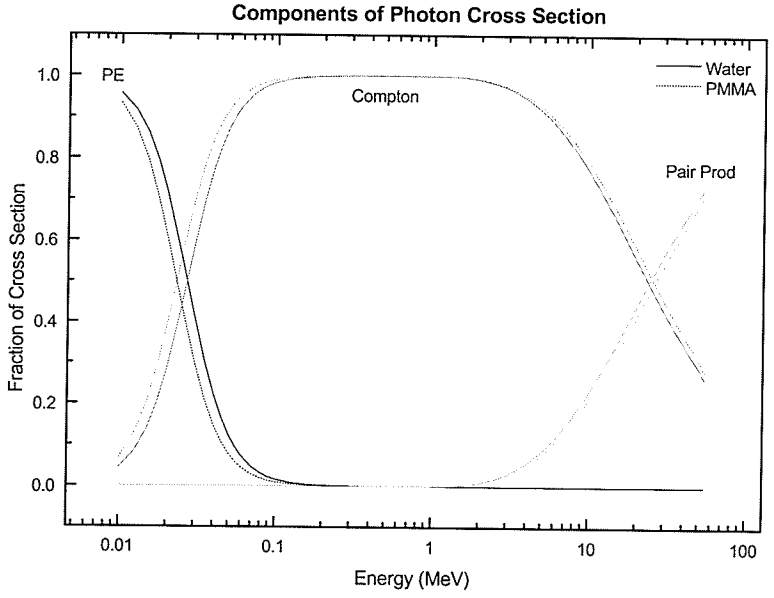

Figure 2.10 The three main components of the photon cross section are shown here for water (solid line) and PMMA (dotted line). As a result of the similarity between these two data sets, our PMMA verification of EGS4 dosimetry was assumed to be applicable to water phantoms as well.

3 Materials and Methods

Focus version 2.5 (Computerized Medical Systems) and Helax-TMS version 4.1 (MDS Nordion) were used to calculate central axis depth dose distributions in the presence of various cylindrical and slab shaped inhomogeneities. These calculations were performed for two different electron energies (9 MeV and 18 MeV), and two different field sizes (10 cm x 10 cm, 15 cm x 15 cm). The overall performance of these treatment planning systems was evaluated using a comparison with Monte Carlo calculations. The accuracy of the Monte Carlo calculations was established using a comparison with measured data obtained at CancerCare Manitoba using a linear accelerator (Siemens KD2-B) which was capable of producing electron beams with nominal energies of 6, 9, 12, 15, 18, and 21 MeV. Actual beam energies determined from measured PDD distributions for the 9 MeV and 18 MeV beams were found to be well within ± 3 % of these nominal values.

The slab-shaped inhomogeneities were positioned so that the axis which characterized the slab thickness was parallel with the beam direction (z axis). In this way the slab geometries represented an inhomogeneity in the z direction only. Each cylindrical inhomogeneity was oriented so that the rotationally symmetric axis was parallel with the beam axis. Cylindrical geometries therefore represented inhomogeneities along each of the x, y, and z axes. These concepts are illustrated in figure 3.1, which shows a cross section through the center of the irradiated geometry.

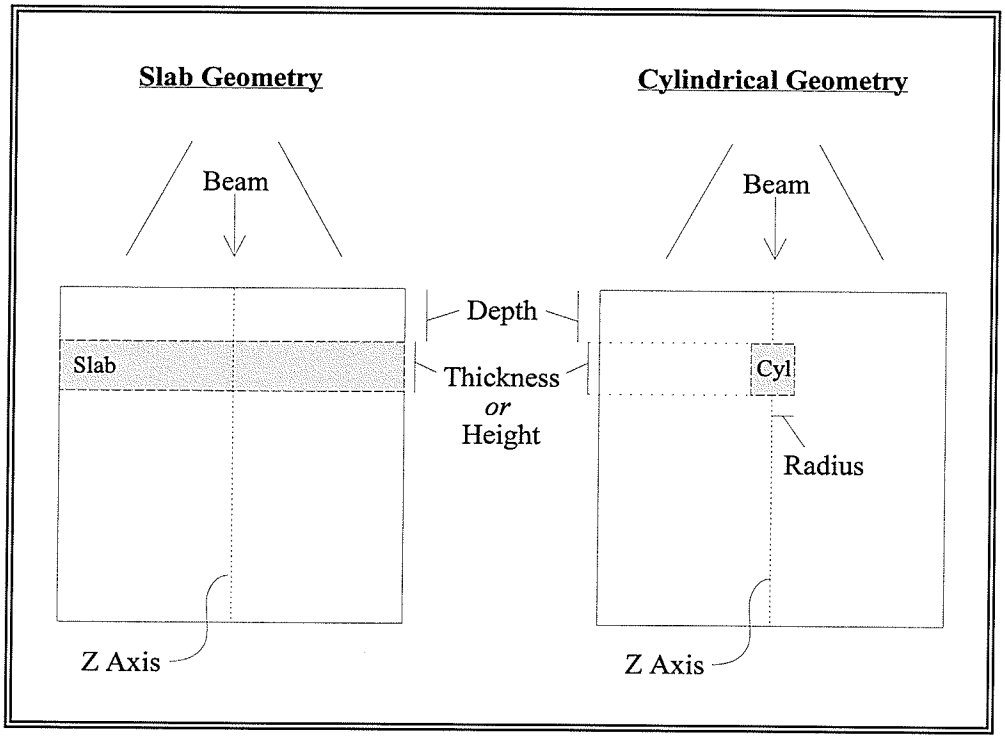

Figure 3.1 Cross section through the center of slab-shaped and cylindrical geometries.

The dimensions of the inhomogeneities simulated in this work are listed in table 3.1. The apparently awkward dimensions tabulated correspond to standard imperial thicknesses of PMMA, and were chosen in order to minimize the amount of machining required when constructing a phantom capable of reproducing all of the required geometries. The tabulated geometries span the range considered by Shortt et al [6], who used EGS4 to simulate the electron dose distribution beyond air and aluminum cylinders exposed to 10 and 20 MeV point sources. The cylinders considered by these authors were 1 cm in diameter, and either 1 cm (aluminum) or 2 cm (air) in height.

Table 3.1 Summary of the dimensions of simulated inhomogeneities. These values correspond to standard imperial thicknesses of PMMA: 1/8" = 0.3175 cm, 1/4" = 0.635 cm, 1/2" = 1.27 cm, 1" = 2.54 cm.

	Cylindrical Geometries			**Slab Geometries**	
	Radius (cm)	*Height (cm)*	*Depth (cm)*	*Thickness (cm)*	*Depth (cm)*
9 MeV	0.635	0.3175	0.635	0.3175	0.635
	0.635	0.635	0.635	0.635	0.635
	0.635	1.27	0.635	1.27	0.635
18 MeV	0.635	0.635	1.27	0.635	1.27
	0.635	1.27	1.27	1.27	1.27
	0.635	2.54	1.27	2.54	1.27

The outer boundaries of an ideal phantom would be large enough so as to appear semi-infinite to an incident electron. A cylindrical phantom with a diameter and height in excess of 30 cm was determined to be acceptable for the field sizes and beam energies considered here. A justification of the adequacy of these phantom dimensions is provided in Appendix I.

All numerical analysis, curve fitting, and interpolation reported in this work was performed using Microcal Origin (version 4.10). [27] This software was also used to plot all graphical data.

3.1 The Phantom

A layered PMMA phantom was constructed by Medical Devices at CancerCare Manitoba, and was used to verify the accuracy of Monte Carlo dose calculations in the presence of slab-shaped and cylindrical inhomogeneities. This phantom was composed of a series of slabs of varying thickness. The slabs came in five varieties:

- PMMA slabs (x 9)
- Aluminum slabs (x 4)
- Square PMMA borders (x 4)
- PMMA slabs with a cylindrical cavity in the center and corresponding cylindrical aluminum plugs (x 4)
- Detector slab (x 1)

The aluminum slabs and the square PMMA borders were used to create aluminum and air slab inhomogeneities respectively. The aluminum slabs were square in cross section, measuring 32.0 ± 0.1 cm on each side. The PMMA borders were also square, with outer dimensions of 30.50 ± 0.09 cm and inner dimensions of 28.06 ± 0.02 cm. The outer dimensions of the remaining slabs were machined to be identical in order to facilitate convenient alignment. These slabs were 30.11 ± 0.02 cm long on each side. PMMA slabs containing cylindrical cavities (diameter = 1.286 ± 0.001 cm) were

accompanied with tight fitting aluminum plugs (diameter = 1.283 ± 0.001 cm) allowing the creation of either aluminum or air inhomogeneities.

The detector slab consisted of a PMMA slab with a thin rubber mat embedded into the center of its upper surface. This rubber mat had a thickness of 0.86 ± 0.01 mm and contained nine square holes in a 3 x 3 grid. These holes were each engineered to contain one LiF thermoluminescent dosimeter (TLD) of dimensions 3.19 ± 0.01 mm x 3.19 ± 0.01 mm x 0.88 ± 0.01 mm. Thus, when placed into the detector slab, both the TLDs and the rubber mat were flush with the upper surface of the slab. When mounted into the detector slab, the central position of the 3 x 3 grid coincided with the center of the slab. This rubber mat is illustrated in figure 3.2.

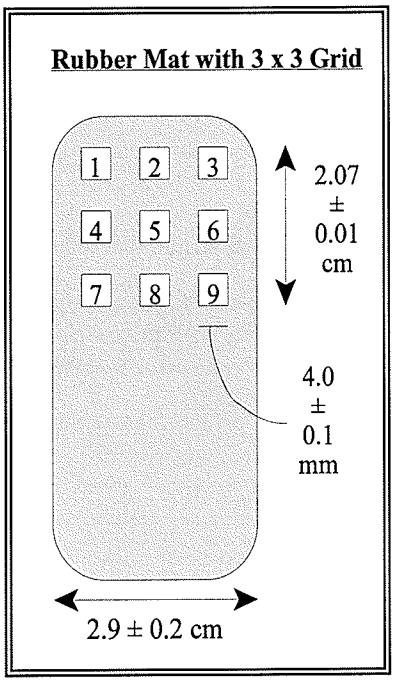

Figure 3.2 This figure illustrates the rubber mat which was placed into the detector slab.

All desired inhomogeneity configurations could be modeled with this phantom by arranging a stack of the appropriate slabs. The basal slab was a 5.013 ± 0.003 cm thick slab of PMMA, which was used primarily as a source of backscatter. Positioned on top of this base were a collection of thinner PMMA slabs and the detector slab. The measurement depth could be varied by changing the position of the detector slab among the homogeneous slabs. Finally, a slab containing an inhomogeneity was added to the stack and placed beneath a homogeneous PMMA slab which had a thickness

corresponding to the desired inhomogeneity depth. These concepts are illustrated in figure 3.3.

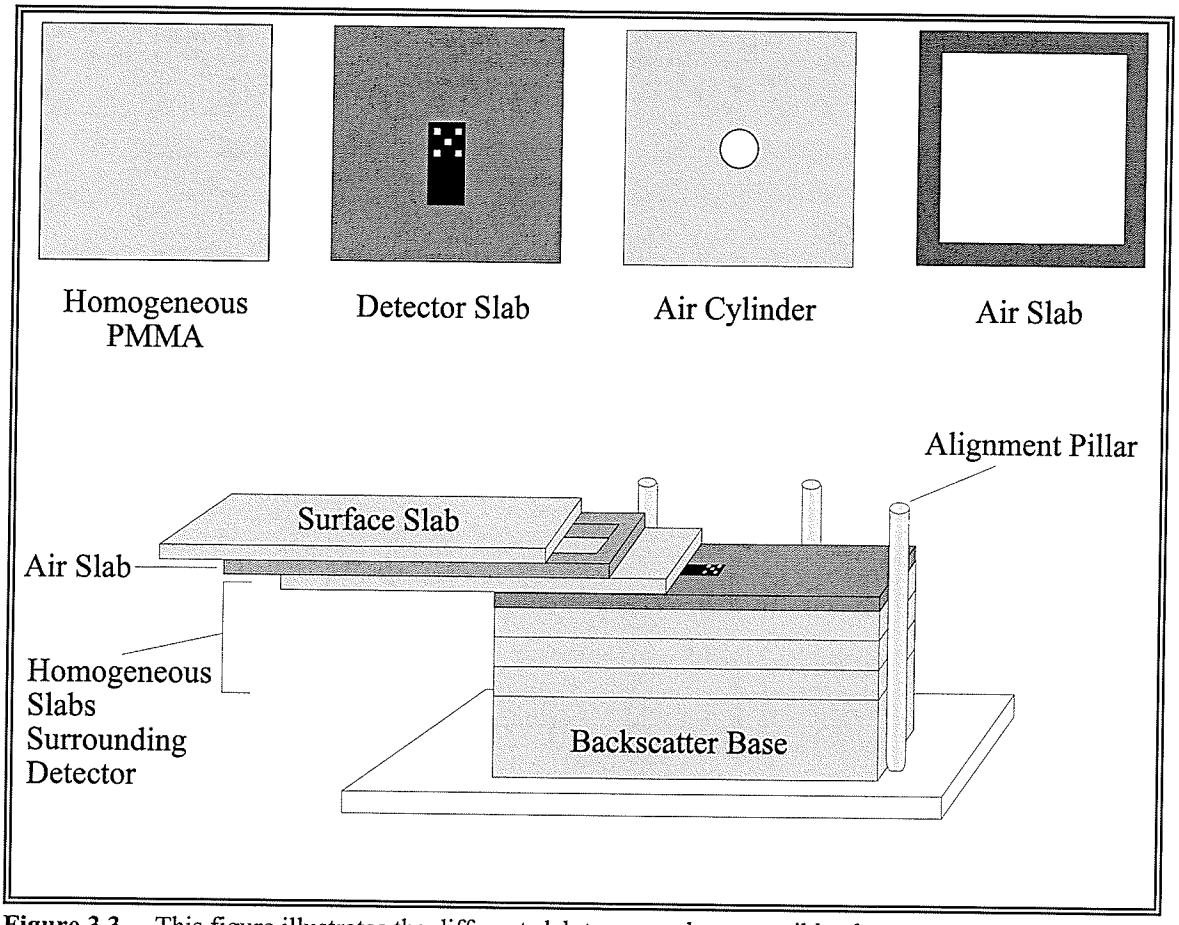

Figure 3.3 This figure illustrates the different slab types, and one possible phantom arrangement.

A three pillar system was used to ensure that all of the slabs well aligned when stacked. These pillars were mounted to a large slab of PMMA, which was clamped to the treatment couch. The treatment couch was used in conjunction with the radiation light field and lasers to maneuver the phantom into the center of the beam. Thus, when the radiation field was centered on the phantom surface, the central axis of the beam

intersected the TLD located in the middle grid position (position 5). All phantom irradiations were performed with the surface slab at an SSD of 100 cm.

This phantom was designed to be capable of reproducing all of the inhomogeneity geometries listed in table 3.1 as closely as possible. With the exception of the 5.013 ± 0.003 cm thick backscatter slab, all slabs were cut from PMMA sheets of various standard thicknesses. The measured thickness of each of these slabs has been tabulated in Appendix II. It was found that these measured thicknesses often differed significantly from the nominal standard thickness. Despite these differences, the slabs were not machined to match the ideal. Excessive machining of PMMA results in a buildup of material stresses which eventually produce warping effects which are detrimental to the alignment of the phantom. Unfortunately, a small degree of slab warping was unavoidable, and a 6 kg UPVC border was centered on top of the phantom in order to counteract this effect. This square border enclosed a 20.1 ± 0.2 cm x 20.1 ± 0.2 cm opening and did not interfere with the radiation field incident upon the phantom.

All reported phantom dimensions correspond to the mean of several measurements made using a digital caliper. The uncertainty in these measurements was calculated as the standard error of the mean. When the standard error was less than 0.001 cm (the smallest digit reported by the caliper), this value was used to represent the measurement uncertainty.

The phantom arrangement was most susceptible to misalignment when measurements were made at large depths beneath cylindrical inhomogeneities. Since the

dose distribution beneath these small cylinders was expected to exhibit dramatic lateral variation, the TLD in position 5 had to be located directly underneath the center of the cylinder.

In order to test the phantom alignment, a piece of lead and tin solder was molded into the shape of a TLD and placed into the detector slab at position 5. The phantom was then stacked up in the following configuration: 1.23 ± 0.01 cm of PMMA (buildup), a PMMA slab containing a 1.28 ± 0.01 cm thick aluminum cylinder, 4.33 ± 0.05 cm of PMMA, a 0.579 ± 0.001 cm thick detector slab containing the solder TLD, one sheet of ready pack diagnostic film (Kodak X-Omat V), and finally 5.013 ± 0.002 cm of PMMA for backscatter. These slabs were all aligned carefully to the three pillar mount and positioned at 100 cm SSD. The phantom was then exposed to 100 MU from a 6 MV photon beam. The film was developed (Konica SRX - 101 developer), and digitized with a film scanner (Lumiscan model number 50, serial number 5391). Osiris (version 3.1) [28] was used to optimize the contrast of the digitized image. The resulting image is shown in figure 3.4, and was judged to exhibit an acceptable degree of alignment.

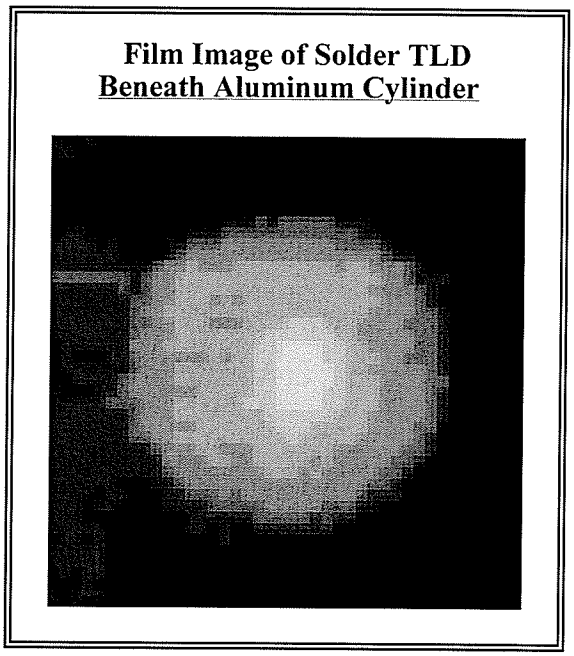

Figure 3.4 The large grey circle depicts the cross section of the aluminum cylinder (1.283 ± 0.001 cm diameter). The relatively bright central square illustrates the position of the solder TLD beneath the cylinder.

The close alignment achievable with this phantom enabled accurate and reproducible results to be obtained along the central axis. The phantom design offered several advantages, such as: cost effectiveness, ease of set-up, and portability. As a result of the versatility of this phantom, many different inhomogeneities could be modeled with a limited number of slabs. Only slight modifications or additions would be required to extend the applicability of the phantom to other situations. For example, only a single slab need be constructed to introduce an entirely new inhomogeneity. Furthermore, if off-axis measurements were desired, TLD pockets could be punched out of a second rubber mat and inserted into the present detector slab.

3.2 General Monte Carlo Methods

BEAM was used to generate a phase space file which modeled the accelerator beam at the phantom surface. A separate file was required for each energy and field size. Since two energies and two field sizes were considered, a total of four phase space files were used: 18 MeV 10 cm x 10 cm, 18 MeV 15 cm x 15 cm, 9 MeV 10 cm x 10 cm, and 9 MeV 15 cm x 15 cm. These files were prepared by Dr. John Lewis and Dr. Boyd McCurdy at CancerCare Manitoba. When changing the field size for a beam of fixed energy, the accelerator components above the main jaws were not changed. Thus a preliminary phase space file was constructed for the geometry illustrated in the left half of figure (3.5). This consisted of a double exit window, primary scattering foils, primary collimator, secondary scattering foils, and an electron dose chamber. The radiation source incident upon this initial set of accelerator components was a cylindrical pencil beam of electrons.

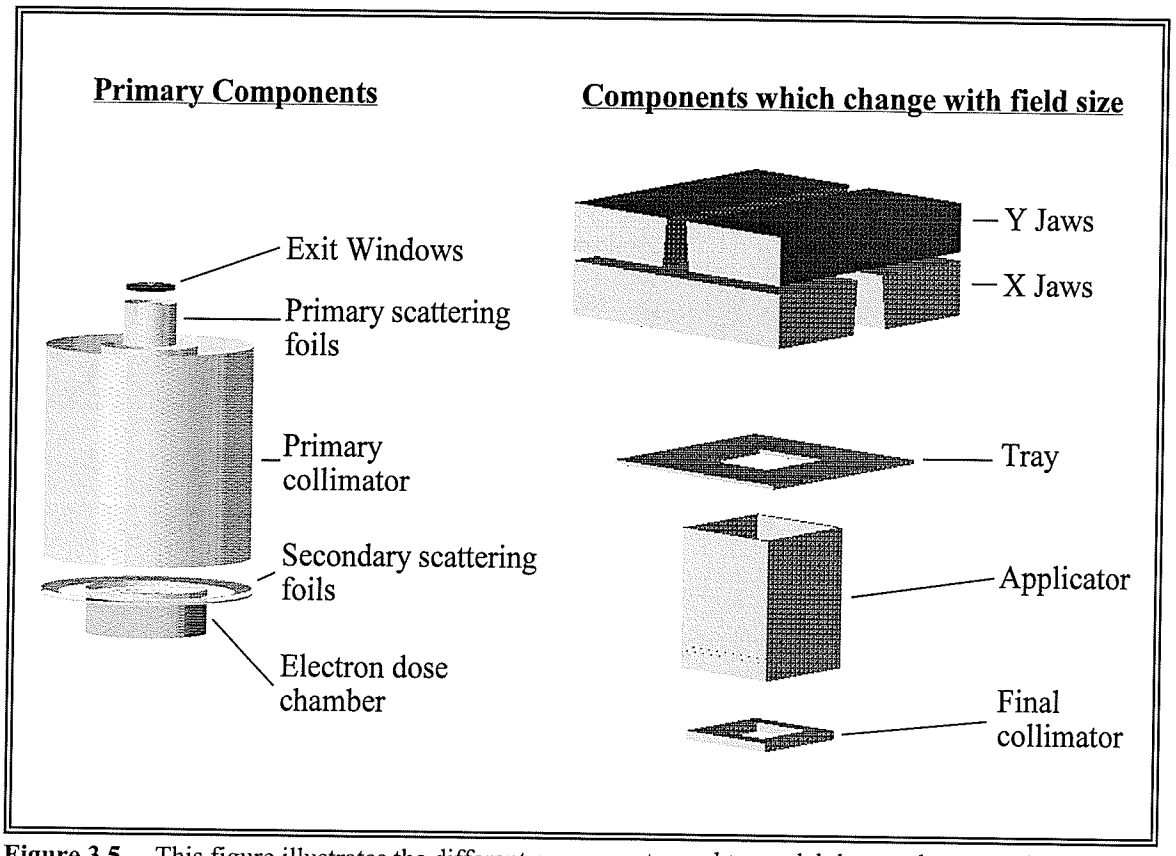

Figure 3.5 This figure illustrates the different components used to model the accelerator. The radiation beam leaving the primary components was used as the source for the components which change with field size. The final phase space file characterizes the radiation beam right at the phantom surface (100 cm SSD). This figure was generated using the BEAM graphics package.[25]

Output from this type of preliminary phase space file was then used as a source, incident on the remaining accelerator geometry. In this way only the latter half of the accelerator needed to be simulated when generating phase space files for the two field sizes. The remaining components in the accelerator geometry are illustrated on the right half of figure (3.5), and include: secondary collimating jaws (X,Y), tray, applicator, and final collimator.

The geometry and material composition of each individual accelerator component were determined using information provided by Siemens.[29] The CMs used to construct these components are summarized in table 3.2. Since only square fields were considered in this analysis, the multileaf collimator was modeled using the JAWS component module rather than the more complicated MLC component module. The ultimate justification for using each of the tabulated CMs was the close agreement observed between phase space files and measured data.

Table 3.2 Components and associated CMs used to define the accelerator geometry.

Primary Components		**Components Dependent upon Field Size**	
Component	*CM*	*Component*	*CM*
Exit Windows	SLABS	Y Jaws (MLC)	JAWS
Primary Foils	FLATFILT	X Jaws	JAWS
Primary Collimator	FLATFILT	Tray	APPLICAT
Secondary Foils	FLATFILT	Applicator	APPLICAT
e^- Dose Chamber	CHAMBER	Final Collimator	APPLICAT

Materials and geometrical dimensions used to specify the tabulated components were obtained from Siemens.[29]

All *phantom* simulations were performed using a phase space file as a source. Furthermore, all *phantom* simulations used the 700ICRU PEGS4 data files to define the phantom media. Consequently ECUT was set at 0.700 MeV, and PCUT at 0.01 MeV. The number of batches used for each of these simulations was changed from 10 to 20.

3.3 General Helax Methods

The exact method used to define a particular phantom geometry in Helax differed for each of the cases considered. Section 3.5.2 discusses the specific details of phantom definition for the homogeneous case. Sections 3.6.1.3 and 3.6.2.2 discuss the definition of phantoms containing slab-shaped and cylindrical inhomogeneities respectively.

In general, Helax allows the user to define a phantom geometry using a stack of two dimensional slices. Polygons and circles are used to specify regions of particular phantom materials in each slice. The three dimensional material composition of the phantom is determined by interpolation between slices. Polygons were defined by inputting the mathematical coordinates of their vertices, and circles by inputting their center, radius, and the number of points along the circumference. The circumference of every Helax circle defined in this work was composed of 10 points. The relative mass densities of the phantom materials may be specified as either air, water, PMMA, aluminum, or vacuum. Once a phantom was defined, it was divided into a matrix of voxels for the purpose of dose calculation. The size of these voxels was dependent upon phantom size, and the separation distance between slices. The maximum resolution (128 x 128 pixels in the transverse plane) was used in all cases. This resolution was sufficient to reproduce all inhomogeneity dimensions in table 3.1 to within ± 0.1 cm.

After the dose distribution was calculated, a depth dose curve was exported as an ASCII file using the LineDose option. The dose was calculated along the central axis

through the entire phantom in depth increments of 0.1 cm. The depth dose curves were smoothed by averaging each point with its two nearest neighbors on either side, provided that those neighbors were not located outside of the phantom or within an inhomogeneity. Using this adjacent averaging technique, the water portion of the depth dose curve consisted of average doses within overlapping 0.5 cm segments. The normalization depth was defined to be 5 cm along the central axis for 18 MeV calculations, and 2.5 cm along the central axis for 9 MeV cases. These specific depths were chosen because they were both below the thickest inhomogeneities considered, and yet they were not so deep as to correspond to extremely low dose regions.

A single fraction dose of 10 Gy was prescribed to the 100% isodose line, and the corresponding number of monitor units was recorded (MU_{TMS}). The dose distribution was then scaled to that which would have resulted if 1000 MU were applied. This was accomplished by multiplying the distribution by $1000/MU_{TMS}$.

3.4 General Focus Methods

The exact method used to define a particular phantom geometry in Focus differed for each of the cases considered. Section 3.5.2 discusses the specific details of phantom definition for the homogeneous case. Sections 3.6.1.3 and 3.6.2.3 discuss the definition of phantoms containing slab-shaped and cylindrical inhomogeneities respectively.

Focus does not allow the phantom geometry to be entered directly, it requires the

user to trace phantom slices on a tablet surface using a mouse-like pointer. Using this apparatus scaled diagrams of several transverse cross sections through the phantom were defined. The proper phantom dimensions were established by specifying the appropriate scaling factor. A button indicator was used to enter important contour points. The remaining contour points were read in automatically at a specified sampling rate of 1 point every 5 cm. This coarse sampling rate was used to ensure that phantom contours were drawn as straight as possible. Phantom inhomogeneities defined in this way were capable of reproducing the geometries listed in table 3.1 to ± 0.1 cm.

Contours defining material boundaries were traced onto each phantom slice. The final material composition of the phantom was determined by interpolating contours between transverse slices. Focus does not provide the user with a list of available phantom materials. Rather, the user defines the phantom composition by assigning a value for the relative electron density of the material within each contour. Table 3.3 lists the relative electron densities used for the materials of interest. Note that Focus only allows these values to be specified to two decimal places.

A series of interest points were positioned along the central axis. These interest points were placed every 0.5 cm when using the 18 MeV beam, and every 0.25 cm when using the 9 MeV beam. The calculated dose at each of these points was printed out with a hard copy of the treatment plan.

Table 3.3 Relative Electron Densities for Different Media

	Mass Density (g/cm^3)	Electron Density (10^{23} e^-/cm^3)	Relative Electron Density
Water	0.998	3.337	1.000
Air	1.205×10^{-3}	3.622×10^{-3}	0.001
PMMA	1.19	3.984	1.194
Aluminum	2.69	7.804	2.339

Mass densities and electron densities were obtained from appendices B.1 and B.2 of *Introduction to radiological physics and radiation dosimetry* by F.H. Attix.[30]

In order to compare dose distributions computed by Helax and Focus, a consistent normalization scheme was required. Consequently, Focus dose distributions were normalized at the central axis interest point located either 5 cm below the phantom surface (18 MeV beam), or 2.5 cm below the phantom surface (9 MeV beam). A single fraction dose of 10 Gy was prescribed to the 100% isodose line, and the MU required to deliver this dose was recorded as MU_{CMS}. Finally, the dose distribution was normalized to 1000 MU using the multiplicative factor $1000/MU_{CMS}$.

3.5 Homogeneous Dose Distributions

The electron dose calculation algorithms used by Focus and Helax make use of homogeneous water measurements when predicting the dose within complicated phantoms. Therefore, any differences in the homogeneous dose distributions used by these treatment planning systems will also affect the inhomogeneous dose distributions.

Corrections can be made to the inhomogeneous distribution if such differences are identified. Consequently, the dose distributions for a simple homogeneous water phantom were evaluated before performing dose calculations in the presence of any inhomogeneities.

Homogeneous dose distributions were generated using both Helax and Focus, and the resulting central axis percentage depth dose curves (PDDs) were compared to measured data. Several numerical parameters characterizing these data sets were calculated and used to quantitatively assess the agreement between these homogeneous distributions. The first such parameter was d_{max}. d_{max} was recorded as the depth coordinate at which the maximum central axis dose value was observed. The uncertainty of this parameter was taken to be the distance between successive depth dose values.

A second numerical parameter recorded was R_{50}, the depth at which a given PDD crosses 50 %. The method of least squares was used to fit a straight line to each homogeneous PDD across the range extending from 70 % to 30 %. The correlation coefficients describing the quality of these fits were typically above 0.999, indicating an excellent representation of the data. R_{50} was determined from the depth coordinate at which each line crossed the 50 % level. Uncertainties were calculated according to the rules of error propagation.

R_{50} was used to calculate the mean energy of the electron beam at the phantom surface. The following equation was used for an electron beam incident on a homogeneous water phantom:

$$E(z = 0) = 2.33 \cdot R_{50} \quad (3.1).$$

Here R_{50} is specified in cm and the mean energy (E) is in MeV. The constant 2.33 MeV/cm is widely accepted for the determination of R_{50}.[1, 31] The uncertainty in the mean energy was calculated by multiplying the uncertainty in R_{50} by 2.33 MeV/cm.

The final parameter used to characterize these homogeneous PDDs was the practical range, R_p. The value of R_p was determined as the depth coordinate of the intersection point between two lines. The first line was fit to the bremsstrahlung tail of the PDD, and the second line was fit to the region of the PDD located between R_{50} and the beginning of the bremsstrahlung tail. Both linear fits were performed using the method of least squares, and uncertainties were calculated by propagating the corresponding errors.

The homogeneous dose distribution was also calculated using Monte Carlo simulation. This dose distribution was compared to measurements in order to investigate the validity of the phase space file being used to describe the accelerator beam. Both a central axis PDD, and transverse dose profiles were considered. The PDDs were evaluated as described above. Transverse dose profiles were obtained at depths of 1.0 cm, 2.5 cm, and 3.5 cm for the 9 MeV beam, and 2.0 cm, 4.5 cm, and 7.5 cm for the 18 MeV beam. In order to ensure that the profiles were evaluated independently of the PDDs, the center point of each Monte Carlo profile was normalized to the central point of each measured profile. A separate Boltzman function was then fit to each side of every

individual profile. This function is shown in equation (3.2), and was used to determine the distance ($x_{1/2}$) at which the profile drops to half of its maximum value. This sigmoidal Boltzmann curve was found to represent the data with a confidence level in excess of 99%.

$$\text{Boltzman}(x) = A_2 + \frac{A_1 - A_2}{1 + \exp\left[\frac{x - x_{1/2}}{\Delta x}\right]} \qquad (3.2)$$

Here, A_1 and A_2 represent the initial height and final height of the profile respectively. Δx determines the slope with which the sigmoid varies between maximum and minimum amplitudes. The $x_{1/2}$ parameter was recorded for each side of the profile being analyzed and compared with measured data. The uncertainty in $x_{1/2}$ was dominated by the positional uncertainty of the chamber, and the accuracy with which each voxel dose could be ascribed to the central position of that voxel.

3.5.1 Homogeneous Monte Carlo Calculations

DOSRZ was used to compute the Monte Carlo PDDs in a homogeneous water phantom. The phantom was defined as a large cylinder concentric with the central axis of the beam. The outer diameter of this cylinder was set at 30.48 cm. Dose was scored within a smaller cylinder, which was also concentric with the central axis. The scoring

cylinder had a diameter of 1cm, and was segmented along its length by planes located every 0.635 cm in the 18 MeV simulations, and every 0.3175 cm in the 9 MeV simulations. The scoring geometry is summarized in table 3.4. The depth position of each recorded dose was taken to be the center of the associated scoring voxel. 50 million histories were simulated in each case.

Table 3.4 This table summarizes the scoring geometry used when simulating the homogeneous PDDs. ECUT was set at 0.700 MeV and PCUT was set at 0.01 MeV.

	9 MeV	**18 MeV**
Height of cylindrical scoring voxels	0.3175 cm	0.635 cm
Radius of cylindrical scoring voxels	0.5 cm	0.5 cm
Number of scoring planes	25	18

To obtain transverse dose profiles, calculations were performed with DOSXYZ for a homogeneous water phantom. In this case the geometry was defined from -15.75 cm to + 15.75 cm in the x and y directions, and from 0 cm to 31.5 cm along the direction of the beam axis (z). This cubic volume was then divided into 63^3 cubic voxels, each having a dimension of 0.5 cm on a side. After simulating 10 million histories, dose profiles were extracted for the appropriate depths using Statdose.

It should be pointed out that the abovementioned PDD data could also have been extracted from this DOSXYZ data set. However, PDD values used throughout this work were obtained using DOSRZ, and hence the homogeneous dose distributions were evaluated using the same geometry.

3.5.2 Homogeneous Calculations with Helax and Focus

Homogeneous dose distributions were calculated using a cubic water phantom with sides 30.5 ± 0.1 cm in length. This phantom was constructed by defining a square contour, and copying this contour onto three transverse slices as shown in figure 3.6. The phantom was assumed to be in the supine position, and the beam was applied to its surface at an SSD of 100 cm. The gantry and couch angle were set to 0.0°.

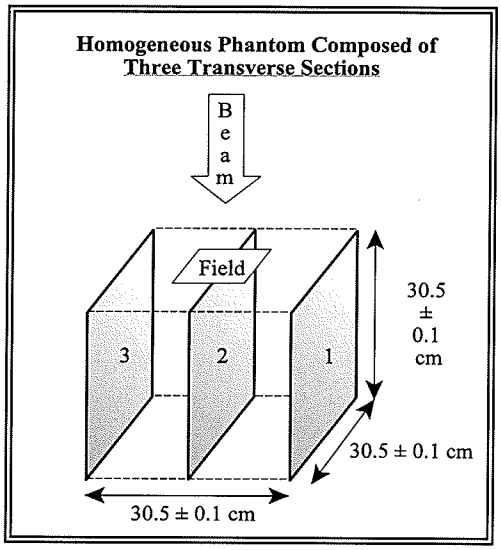

Figure 3.6 Geometry involved in the definition of a homogeneous phantom.

3.5.3 Water Measurements

A series of dose distributions were recorded in a homogeneous water phantom. These measurements were performed by Yuri Mandelzweig at CancerCare Manitoba (then Manitoba Cancer Treatment and Research Foundation) in December of 1996 using a scanning water tank (PTW-Freiburg MP3-S model number 41002-0037). The tank was composed of perspex, and had inner dimensions of 59.4 cm x 49.6 cm x 50.2 cm.[32] The tank was equipped with motorized stages which maneuvered an ionization chamber

along the x, y, and z directions. A second chamber was fixed above the tank to serve as a reference, monitoring any fluctuations in beam output. Both chambers were thimble ionization chambers (PTW-Freiburg model number 31002, serial numbers 0423 and 0424). The ionization produced in these chambers was measured using an electrometer (PTW-Freiburg MP3-S model number 41004, serial number 0038), and recorded using the associated Software (Mephysto Version 6.0 - PTW-Freiburg).[33]

The scanning tank was leveled, and aligned beneath the accelerator head. With the water surface at 100 cm SSD, the scanning chamber was used to measure the ionization produced along the central axis. The 18 MeV measurements were taken in 0.5 mm intervals over a distance extending from the water surface down to a depth of 12 cm. Further measurements were then recorded every 10 mm, to a total depth of 30 cm. For 9 MeV measurements, 0.5 mm steps were used from the surface to a depth of 6 cm. The remainder of the distance out to 30 cm was sampled every 10 mm. In both cases the chamber was held at each measurement location for 0.2 seconds. Mephysto was used to convert the resulting depth ionization curves into depth dose curves according to the IAEA TR277 code of practice.[33]

In order to measure the beam profiles, the chamber was moved to the required depth (1.0 cm, 2.5 cm, and 3.5 cm for the 9 MeV, 2.0 cm, 2.5 cm, and 7.5 cm for the 18 MeV beam), and then scanned laterally across the field in 1 mm steps. This scan extended from -7 cm to 7 cm for the 10 cm x 10 cm field, and from -9.5 cm to 9.5 cm for the 15 cm x 15 cm field. The chamber was held in place for 0.1 seconds at each location.

The positional uncertainty of the chamber was ± 0.05 cm.

3.6 Inhomogeneous Dose Distributions

Inhomogeneous dose distributions were calculated by Focus and Helax for the geometries listed in table 3.1. The accuracy of these calculations was evaluated along the central axis using a comparison with Monte Carlo simulations. These distributions were expressed as PDD curves, with the vertical axes normalized to 100% at the maximum dose of the corresponding *homogeneous* distribution. Both Focus and Helax make use of homogeneous depth dose data when predicting the dose in the presence of an inhomogeneity. When these homogeneous distributions differ, corresponding differences arise in the inhomogeneous prediction. In order to minimize these effects when comparing dose distributions calculated by different modalities, each inhomogeneous curve calculated via treatment planning computer was multiplied by a ratio of homogeneous dose distributions. The numerator and denominator of this ratio were taken from the homogeneous distributions predicted by Monte Carlo simulation and the appropriate treatment planning system respectively. More specifically, Focus and Helax predictions were interpolated linearly to depths at which a Monte Carlo dose had been scored. The homogeneous and inhomogeneous interpolated distributions may be represented by $(\text{Hom PDD(d)})_{\text{TPS}}$ and $(\text{Inhom PDD(d)})_{\text{TPS}}$ respectively. In this notation d is the interpolated depth, and TPS represents the treatment planning system involved. The

corrected inhomogeneous distribution was calculated as shown in equation (3.3).

$$\left(\text{Inhom PDD(d)}\right)_{TPS}^{Corr} = \left(\text{Inhom PDD(d)}\right)_{TPS}\left[\frac{\left(\text{Hom PDD(d)}\right)_{EGS4}}{\left(\text{Hom PDD(d)}\right)_{TPS}}\right] \qquad (3.3)$$

Here $(\text{Hom PDD(d)})_{EGS4}$ is the dose calculated by Monte Carlo simulation at a depth d within a homogeneous water phantom and $\left(\text{Inhom PDD(d)}\right)_{TPS}^{Corr}$ is the corrected inhomogeneous distribution. Although this ratio multiplication technique was only an approximate correction method, it was judged to be sufficiently accurate that any differences between corrected treatment planning predictions and Monte Carlo results could be attributed to a weakness in the way that the treatment planning system expected the inhomogeneity to affect the dose distribution. The effectiveness of this ratio correction method is discussed in further detail in appendix III.

The difference between the corrected data and Monte Carlo calculations was used to represent the deviation between treatment planning predictions and the actual depth dose values. This deviation was calculated over two different depth ranges. The first extended from directly beneath the inhomogeneity to the depth at which the inhomogeneous Monte Carlo PDD dropped permanently below 80%. The second range was defined in a similar fashion, but was extended all the way down to the 50% depth. The maximum and mean deviations were tabulated over both of these ranges for each

individual inhomogeneity.

3.6.1 Slab Inhomogeneities

3.6.1.1 Verification of Monte Carlo Calculations

EGS4 was tested to ascertain its ability to accurately calculate absorbed dose in the presence of slab inhomogeneities. This was accomplished by comparing the EGS4 predictions with data measured in the PMMA phantom. One air slab and one aluminum slab were considered for each energy. The nominal slab geometries used for this verification are summarized in table 3.5 below.

Table 3.5 Summary of the dimensions of slabs simulated for Monte Carlo verification. These slab inhomogeneities were simulated in a phantom specified to consist of PMMA.

	Air Slab		Aluminum Slab	
	Depth (cm)	*Thickness (cm)*	*Depth (cm)*	*Thickness (cm)*
9 MeV	0.635	0.3175	0.635	0.635
18 MeV	1.27	1.27	1.27	1.27

The simulations were performed using DOSRZ. The homogeneous phantom was defined as a cylinder 30.48 cm in diameter, and composed of a stack of PMMA disks. Each disk was 0.635 cm (0.3175 cm) thick when the 18 MeV (9 MeV) beam was used. In both cases, the total thickness of the stack was greater than 15 cm. For the

inhomogeneous phantom, the required thickness of consecutive PMMA disks were replaced with either air or aluminum. The thickness and depth of these inhomogeneous slabs were defined as tabulated above. The central axis scoring volumes were cylindrical, 1 cm in diameter, with heights of either 0.635 cm (18 MeV) or 0.3175 cm (9 MeV). 50 million histories were evaluated in each case.

The corresponding geometrical arrangements were then assembled beneath the linear accelerator using the PMMA phantom, and doses were measured at several depths beneath the inhomogeneity. When using TLDs, a certain amount of statistical fluctuation was expected between similar measurements. Thus the average of five TLD measurements was used to calculate a single dose value. The uncertainty of this average value was expressed by calculating the standard error of the mean. Measured results were compared to simulated values after being corrected through the use of dose ratios. This ratio correction is shown in equation (3.4). $\langle \text{Inhom PDD(d)} \rangle_{\text{TLD}}$ denotes the mean of five inhomogeneous TLD measurements at depth d, and $\langle \text{Hom PDD(d)} \rangle_{\text{TLD}}$ denotes the mean of five corresponding homogeneous measurements. Homogeneous Monte Carlo data $(\text{Hom PDD(d)})_{\text{EGS4}}$ were calculated at the measurement depth using linear interpolation. The uncertainty of the corrected dose value $\left(\text{Inhom PDD(d)}\right)_{TLD}^{Corr}$ was determined using the ordinary rules of error propagation.

$$\left(\text{Inhom PDD(d)}\right)_{TLD}^{Corr} = \left\langle \text{Inhom PDD(d)} \right\rangle_{TLD} \frac{\left(\text{Hom PDD(d)}\right)_{EGS4}}{\left\langle \text{Hom PDD(d)} \right\rangle_{TLD}} \qquad (3.4)$$

In order to minimize any systematic errors arising from gradual changes in the beam intensity, each homogeneous and inhomogeneous pair of dose measurements were obtained one after the other. That is, TLDs were placed into the detector slab at positions 1, 3, 5, 7, and 9. The detector slab was positioned at a depth d within a homogeneous phantom, and the TLDs were irradiated. Immediately afterward, a set of five new TLDs were loaded into the same grid locations, and the detector slab was positioned within the inhomogeneous phantom arrangement at the same depth d. Following the second irradiation, the process was repeated at other depths. Measurements were concentrated in the range extending from the base of the inhomogeneity to the depth at which the inhomogeneous dose distribution was expected to fall permanently below 80% of the *homogeneous* dose maximum. The lateral dose distribution was sufficiently uniform that there was no statistically significant difference between TLD measurements from grid positions 1, 3, 7, and 9, and measurements from the TLD located directly on the central axis (position 5).

3.6.1.2 Monte Carlo Methods for Slab Geometries

Once the accuracy of the EGS4 simulations was established in the presence of slab inhomogeneities, simulations were executed for all slab geometries listed in table 3.1. The method of phantom definition was identical to that described above, except that water was used in place of PMMA. 50 million histories were evaluated for each case.

3.6.1.3 Helax and Focus Methods for Slab Geometries

Slab phantoms were defined using three identical transverse slices as shown in figure 3.7. The outer periphery of the volume contained by these slices was a cube, with each side measuring 30.5 ± 0.1 cm. The slab inhomogeneity was drawn into the upper portion of each transverse slice using a rectangular contour. The depth and thickness of this rectangle defined the depth and thickness of the slab. The phantom was assumed to be in the supine position, and a 0.0° gantry and couch angle was used. The field was specified at an SSD of 100 cm.

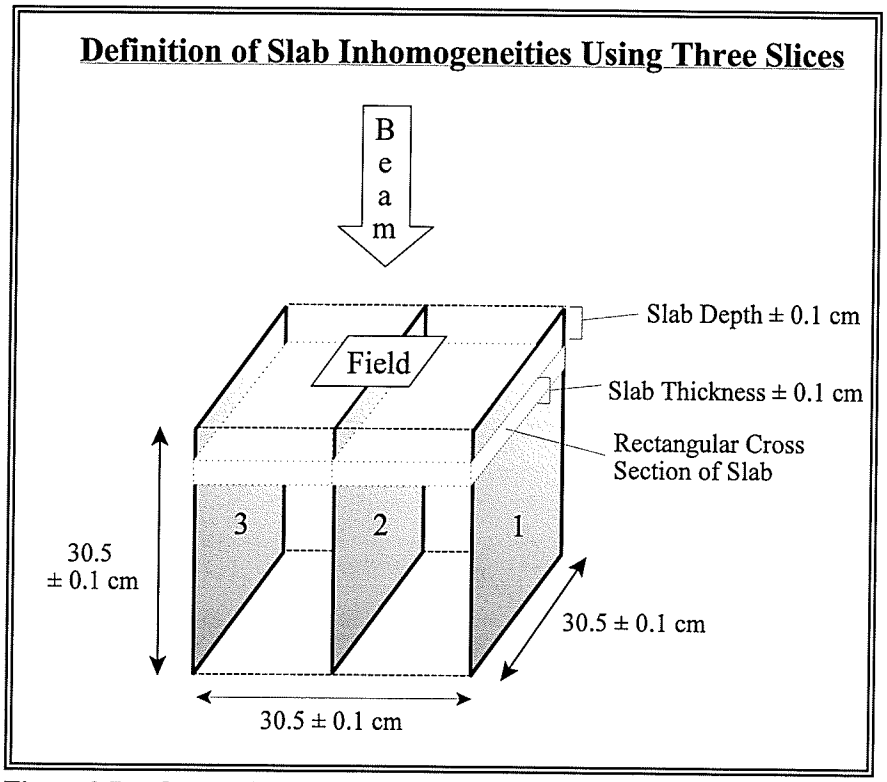

Figure 3.7 Geometrical construction of slab geometry in Focus and Helax.

3.6.2 Cylindrical Inhomogeneities

3.6.2.1 Verification of Monte Carlo Calculations

An examination was made of the accuracy with which EGS4 simulations represented experimental measurements in the presence of cylindrical inhomogeneities. One air cylinder and one aluminum cylinder were simulated in PMMA for each energy and compared to measured data. The nominal cylindrical geometries used for this verification are summarized in table 3.6 .

Table 3.6 Summary of the dimensions of cylinders simulated for Monte Carlo verification. The cylinder height is defined as the cylinder thickness along the z axis. These cylindrical inhomogeneities were simulated in a phantom defined to consist of PMMA.

	Air			**Aluminum**		
	Depth (cm)	*Height (cm)*	*Radius (cm)*	*Depth (cm)*	*Height (cm)*	*Radius (cm)*
9 MeV	0.635	0.635	0.635	0.635	0.635	0.635
18 MeV	1.27	2.54	0.635	1.27	1.27	0.635

Simulations were performed using DOSRZ. As before, the homogeneous phantom was defined by a cylinder 30.48 cm in diameter, which was composed of PMMA disks stacked up to a total height in excess of 15 cm. When the 18 MeV (9 MeV) beam was used each of these disks was assigned a height of 0.635 cm (0.3175 cm). For the inhomogeneous phantom, the center of the required thickness of PMMA disks was

replaced with an air or aluminum cylinder. The geometry and position of the inhomogeneous layers is defined in Table 3.6. The scoring volumes were cylindrical, 3 mm in diameter, with heights of either 0.635 cm (18 MeV) or 0.3175 cm (9 MeV). The 3 mm diameter was chosen so that the amount of lateral variation within each scoring volume would be similar to that experienced by a single TLD. 200 million histories were evaluated for each simulation.

The physical PMMA phantom was then assembled accordingly, and doses were measured at several depths beneath each inhomogeneity. As before, the dose ratio at any particular depth was evaluated by dividing the mean of five inhomogeneous TLD measurements by the mean of five homogeneous measurements. The lateral dose distribution beneath cylindrical inhomogeneities was expected to exhibit significant variations. Therefore, measurements were made one TLD at a time, with each TLD located directly on the central axis (position 5 of the detector layer). Five homogeneous and five inhomogeneous measurements were collected for each depth. Measurements were concentrated above the depth at which the inhomogeneous dose distribution was expected to fall permanently below 50% of the *homogeneous* dose maximum.

The agreement between TLD measurements and Monte Carlo simulation was evaluated using equation (3.4). As before, the EGS4 data were interpolated to the measurement depth.

3.6.2.2 Monte Carlo Methods for Cylindrical Geometries

Once the accuracy of the EGS4 simulations was established in the presence of cylindrical inhomogeneities, simulations were executed for all corresponding geometries listed in table 3.1. The phantom was defined as described in section 3.6.2.1, with water being used in the place of PMMA. 200 million histories were evaluated for each case.

3.6.2.2 Helax Methods for Cylindrical Geometries

Four transverse slices were used to define a phantom containing a cylindrical inhomogeneity with a height H, and a radius R, at a depth d. These slices were square, with each side measuring 30.5 ± 0.1 cm. The top and bottom slices were separated by a total distance of 30.5 ± 0.1 cm, and therefore defined the boundaries of a cubic phantom volume. The two remaining slices were placed a distance d and d + H from the top section respectively. These sections contained a circle of radius R at their center, and were used to define the upper and lower boundaries of the cylinder. The depth, height, and radius were all within ± 0.1 cm of the nominal values listed in table 3.1. In order to align the beam axis with the cylinder axis, the phantom was defined to be in the supine position, and the couch and gantry were rotated through an angle of 90°. A 100 cm SSD was used. This was judged to be the most accurate method for defining cylindrical inhomogeneities in Helax-TMS.

3.6.2.3 Focus Methods for Cylindrical Geometries

Due to limitations in the allowed orientation of electron beams in Focus, the procedure outlined above could not be used to plan a treatment for a phantom containing cylindrical inhomogeneities. If one tries to use the previous method, the initial beam arrangement is illustrated in figure 3.8 as 'beam position ①'. The desired treatment orientation could be arranged by rotating the beam by 90°, as illustrated by 'beam position ②'. Unfortunately the Focus user cannot make this rotation. This restriction is presumably intended to safeguard against patient-applicator collisions.

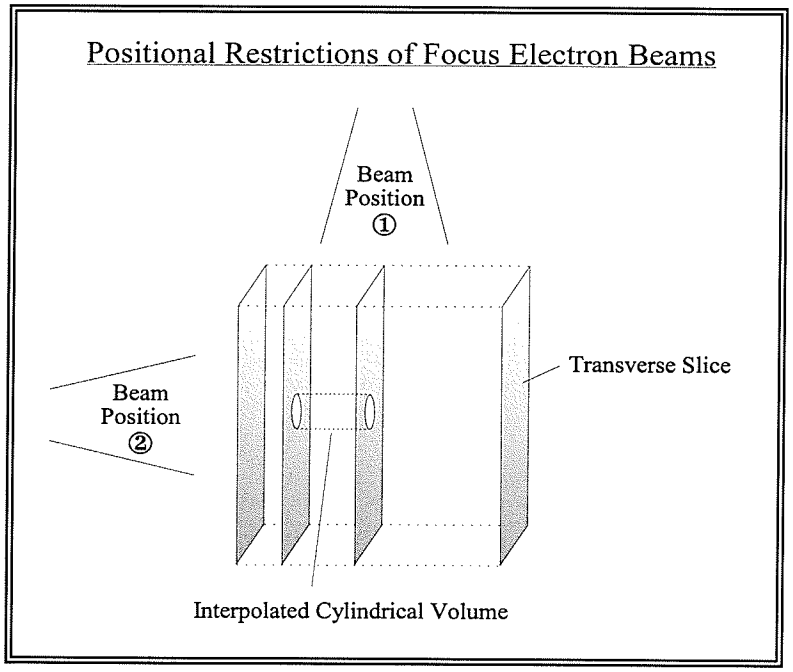

Figure 3.8 Beam positon ① is the initial beam configuration. The beam cannot be rotated through 90° into beam position ②.

In Focus, phantom electron densities are calculated by interpolating between transverse slices. Therefore only contours drawn on transverse slices could be used to define a cylindrical volume within the phantom. These slices were oriented parallel to the cylinder axis. Thus, each slice which cut through the cylinder contained a rectangle. Only the width of this rectangle varied from slice to slice. This concept is illustrated in figure 3.9.

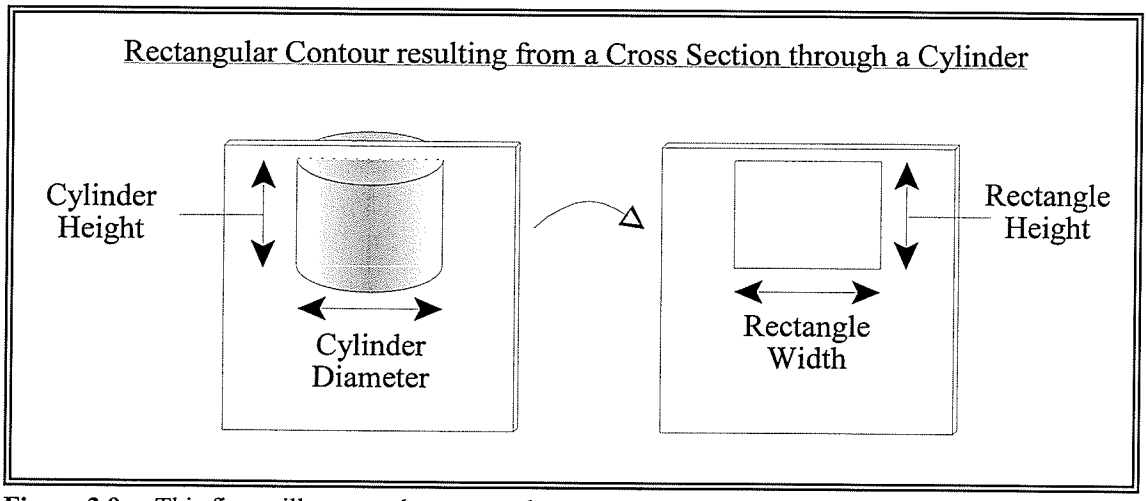

Figure 3.9 This figure illustrates the rectangular contour present in a cross section through a cylinder.

In order to define a cylindrical inhomogeneity using this set of transverse sections, the width of each rectangle had to be determined for every slice. The slice position was measured from the central axis of the cylinder, and denoted as y. The width of the corresponding rectangular inhomogeneity contour was denoted as 2x, where x was calculated according to the following equation.

$$x = \sqrt{R^2 - y^2} \qquad (3.5)$$

Here R is the cylinder radius. Nine rectangular contours were traced out over y values ranging from -R to R.

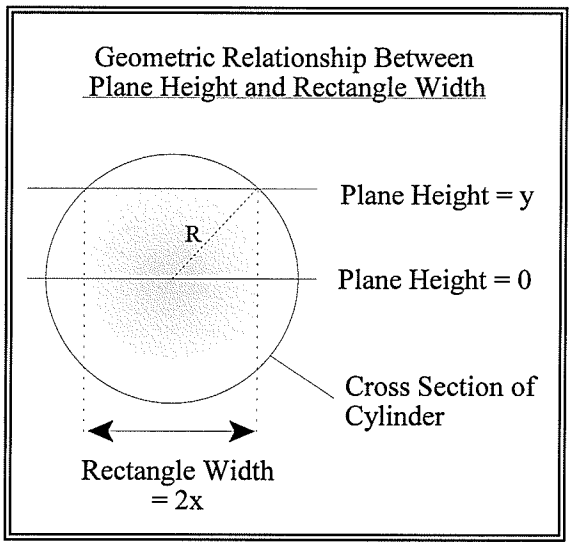

Figure 3.10 Geometrical reconstruction used to specify the relationship between rectangle width (2x) and plane height (y).

The outer boundary of the Focus phantom was a cube, with dimensions of 30.5 ± 0.1 cm on each side. The depth height and radius of the cylindrical inhomogeneity imbedded within this cube were all within ± 0.1 cm of the nominal values listed in table 3.1 . In order to obtain the proper alignment with the treatment beam, the phantom was oriented in the supine position, with an SSD of 100 cm.

A photon calculation was used to verify the equivalence between a cylinder defined in this way and one defined by two circular contours (as with Helax). Both methods were used to create a similar cylindrical inhomogeneity. In Focus the orientation of photon beams is less restricted than for electrons, and a percentage depth dose curve was generated for cylinders defined by both methods using a 6 MV photon beam. The resulting distributions did not differ by more than 1 %, with a mean deviation of 0.6 %. Although different algorithms are used to calculate photon and electron doses, both make use of the digitized electron densities used to represent the phantom. Based on the close agreement between these distributions, the two methods of cylinder definition were considered to be essentially identical in Focus.

3.7 Reading TLDs

Before being irradiated, the TLDs were annealed in an oven (PTW-TLDO model number 1321, serial number 1419). The temperature was raised to 400°C, and held there for 1 hour. The oven was then cooled down to 100°C and this temperature was maintained for 2 hours. Finally the oven was lowered to 45°C, at which point the TLDs were left to approach ambient temperature on their own. [35]

The TLDs were then read individually using a TLD analyzer (Harshaw QS model number M3500, serial number 9209017). Once placed into this unit, a TLD was immersed in a nitrogen atmosphere and preheated at 50°C for 1 second. Data acquisition

commenced shortly afterward while the temperature was raised 8°C per second up to a target value of 240°C, at which point the temperature was held constant. The total acquisition time was 30 seconds.[36]

During the acquisition process, light given off by the TLD was intercepted by a photomultiplier tube. The TLD analyzer reported the total amount of charge that was induced while the TLD glow curve was being recorded. This charge value was linearly proportional to the absorbed dose.

4 Results and Discussion

This chapter presents the depth doses calculated for homogeneous and inhomogeneous phantoms. Homogeneous results are presented in section 4.1. The Monte Carlo phase space files are validated, and justification is provided for using ratios to correct inhomogeneous dose distributions. The corrected inhomogeneous distributions are presented in sections 4.2 (slabs) and 4.3 (cylinders), where the accuracy of the Monte Carlo simulations is compared to measured data. The dosimetric accuracy of Focus and Helax predictions in a water based phantom is then presented for each field size.

4.1 Homogeneous Dose Distributions

Presented in the following sub sections are the results of an examination of homogeneous dose distributions for 9 and 18 MeV electron beams. Both the 10 cm x 10 cm and 15 cm x 15 cm field sizes were investigated.

4.1.1 Depth Dose Curves

Percentage depth dose curves calculated by Monte Carlo simulation and the Focus and Helax treatment planning systems were compared with water tank measurements obtained using an ion chamber. These comparisons are presented below for both

energies.

4.1.1.1 9 MeV Beam

Figure 4.1 shows the homogeneous percentage depth dose distributions predicted by Monte Carlo, Focus, and Helax for both the 10 cm x 10 cm field (top graph) and the 15 cm x 15 cm field (lower graph). From these figures it can be seen that the Monte Carlo and Focus predictions agreed well with the measured data. At depths greater than 2 cm, the Helax predictions underestimated the actual dose.

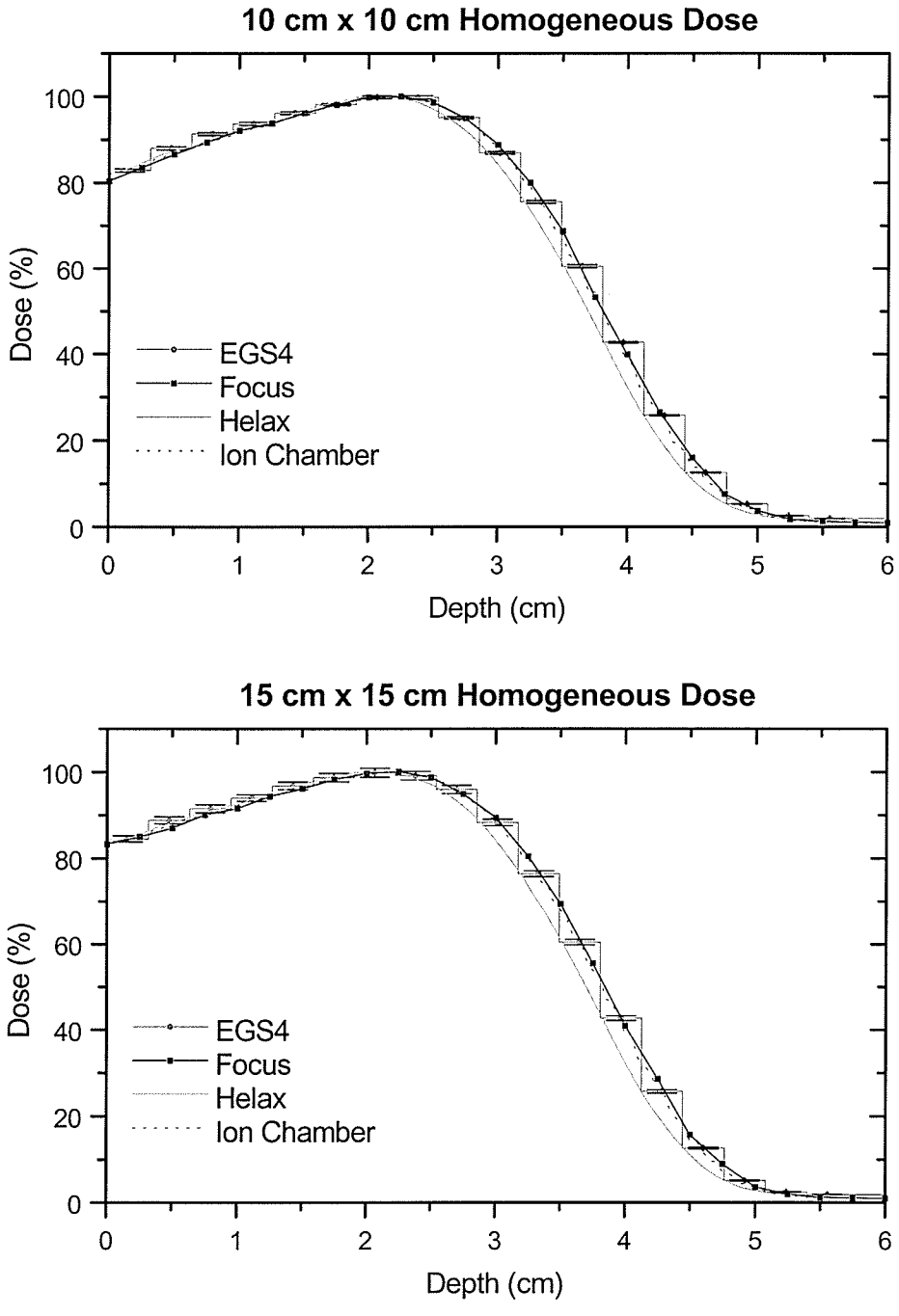

Figure 4.1 Homogeneous electron dose distributions in water for a 9 MeV beam.

Table 4.1 Summary of the parameters extracted from each individual 9 MeV homogeneous dose distribution illustrated in figure 4.1. Monte Carlo and treatment planning results should be compared with ionization chamber measurements.

Field Size	Data Source	d_{max} (cm)	R_{50} (cm)	$E_{(z=0)}$ (MeV)	R_p (cm)
10 cm x 10 cm	Chamber	2.20 ± 0.05	3.8 ± 0.1	8.9 ± 0.3	4.7 ± 0.1
	EGS4	2.1 ± 0.3	3.8 ± 0.1	8.9 ± 0.3	4.7 ± 0.1
	Helax	2.1 ± 0.1	3.7 ± 0.1	8.6 ± 0.3	4.6 ± 0.1
	Focus	2.3 ± 0.3	3.8 ± 0.1	8.9 ± 0.3	4.8 ± 0.2
15 cm x 15 cm	Chamber	2.25 ± 0.05	3.8 ± 0.1	8.9 ± 0.3	4.7 ± 0.1
	EGS4	2.1 ± 0.3	3.8 ± 0.1	8.9 ± 0.3	4.7 ± 0.1
	Helax	2.0 ± 0.1	3.7 ± 0.1	8.6 ± 0.3	4.5 ± 0.1
	Focus	2.3 ± 0.3	3.9 ± 0.1	9.0 ± 0.3	4.8 ± 0.1

The curves plotted in figure 4.1 are further characterized by the parameters listed in Table 4.1. The Monte Carlo and Focus results for d_{max}, R_{50}, the mean surface energy ($E_{(z=0)}$) and the practical range (R_p) were in good agreement with the corresponding parameters of the measured data set. Helax values were smaller than expected. The discrepancy between ion chamber measurements and Helax parameters was more pronounced in the 15 cm x 15 cm distribution.

Van Dyk [5] has stated that an electron planning system should be able to reproduce the homogeneous dose distribution along the central axis to within ± 2 % of measured data. The maximum and mean deviations between predicted and measured doses were calculated over a range of depths extending from 0 to R_{50}. These results are

tabulated below.

Table 4.2 Deviation Between Calculated and Measured Homogeneous Doses calculated for the 9 MeV beam. Tabulated values have been expressed as a percentage of the central axis normalization dose.

Field Size	Data Source	Mean Dev. (%)	Max Dev. (%)
10 cm x 10 cm	EGS4	0.7	1.8
	Helax	1.9	7.1
	Focus	0.4	1.3
15 cm x 15 cm	EGS4	0.6	1.1
	Helax	2.1	8.3
	Focus	0.4	1.3

The 7.1 % and 8.3 % deviations exhibited by the Helax distribution represent a significant departure from the Van Dyk criteria. These differences in the homogeneous data demonstrate the importance of using dose ratios to correct inhomogeneous depth dose distributions before evaluating algorithm performance.

4.1.1.2 18 MeV Beam

The homogeneous dose distributions predicted for the 18 MeV electron beam were analyzed as described in section 4.1.1.1. Figure 4.2 illustrates the homogeneous percentage depth dose curves obtained for each field size. The parameters d_{max}, R_{50}, $E_{(z=0)}$,

and R_p were determined for each homogeneous distribution and are listed in table 4.3. It can be seen that Helax underestimates the measured dose for the 10 cm x 10 cm field.

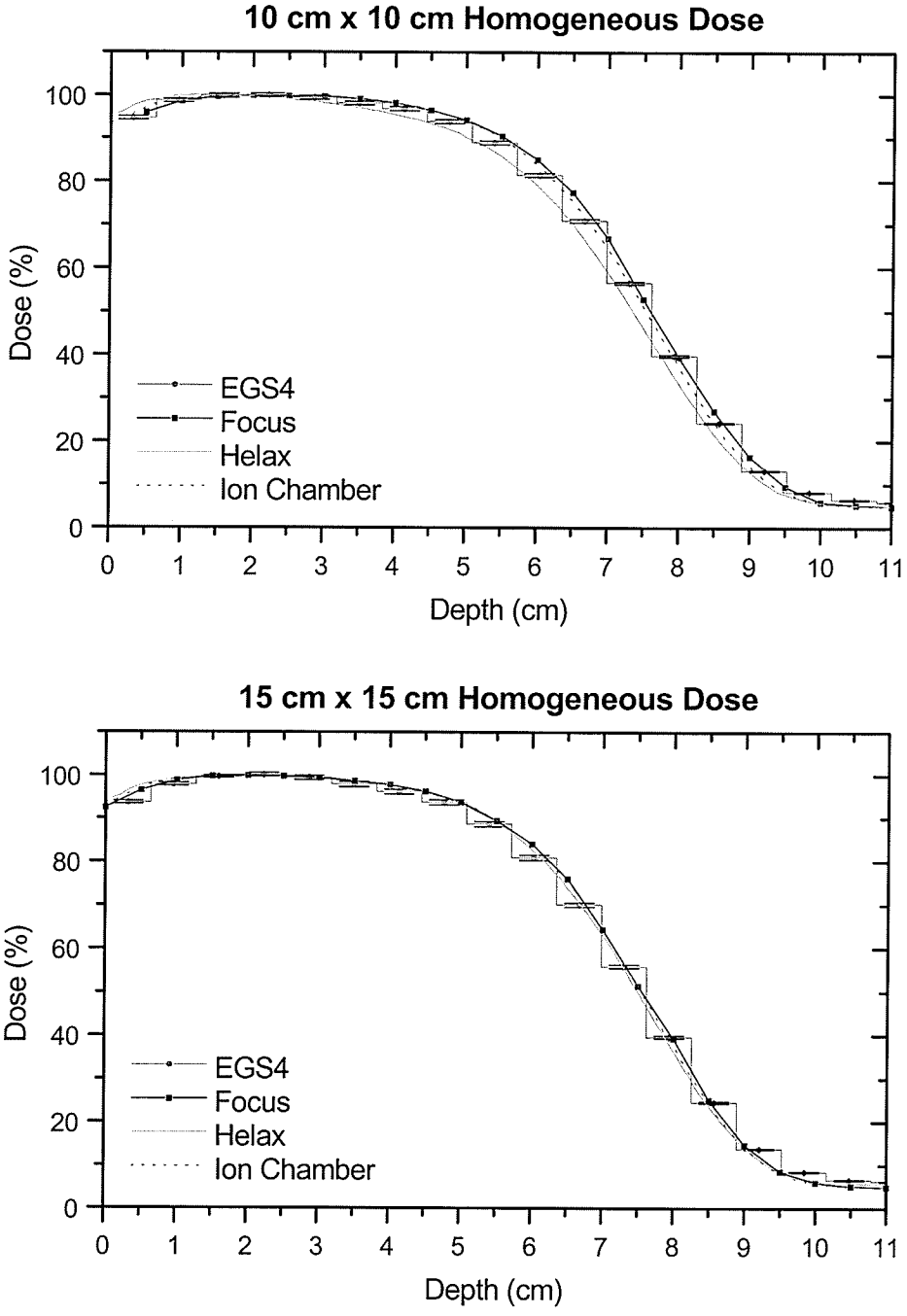

Figure 4.2 Homogeneous electron dose distributions in water for an 18 MeV beam.

Table 4.3 Summary of parameters extracted from the 18 MeV homogeneous dose distributions shown in figure 4.2. Monte Carlo and treatment planning results should be compared with ionization chamber measurements.

Field Size	Data Source	d_{max} (cm)	R_{50} (cm)	$E_{(z=0)}$ (MeV)	R_p (cm)
10 cm x 10 cm	Chamber	2.40 ± 0.05	7.55 ± 0.09	17.6 ± 0.2	9.2 ± 0.1
	EGS4	2.2 ± 0.6	7.5 ± 0.2	17.6 ± 0.5	9.3 ± 0.2
	Helax	1.2 ± 0.1	7.4 ± 0.1	17.1 ± 0.3	9.1 ± 0.1
	Focus	2.0 ± 0.5	7.6 ± 0.1	17.7 ± 0.3	9.3 ± 0.1
15 cm x 15 cm	Chamber	2.25 ± 0.05	7.5 ± 0.1	17.6 ± 0.2	9.2 ± 0.1
	EGS4	2.2 ± 0.6	7.5 ± 0.2	17.5 ± 0.4	9.3 ± 0.2
	Helax	1.9 ± 0.1	7.5 ± 0.1	17.5 ± 0.3	9.1 ± 0.1
	Focus	2.0 ± 0.5	7.6 ± 0.2	17.6 ± 0.4	9.3 ± 0.1

The homogeneous dose distribution from the 18 MeV beam exhibited a very broad high dose region. This explains the larger differences observed between the 18 MeV d_{max} results relative to the 9 MeV case. Helax results for d_{max} were not in agreement with ion chamber measurements for either field size. R_{50}, the mean surface energy ($E_{(z=0)}$), and the practical range (Rp) agreed for the 15 cm x 15 cm field. However, the 10 cm x 10 cm Helax curve yielded R_{50}, $E_{(z=0)}$, and R_p values which were consistently less than those obtained from the other distributions.

Table 4.4 shows the maximum and mean deviations calculated between measured and predicted distributions. This analysis was performed over a range of depths extending from 0 to R_{50}.

Table 4.4 Deviation Between Calculated and Measured Homogeneous Doses calculated for the 18 MeV beam. Tabulated values have been expressed as a percentage of the central axis normalization dose.

Field Size	Data Source	Mean Dev. (%)	Max Dev. (%)
10 cm x 10 cm	EGS4	0.8	1.9
	Helax	2.7	5.5
	Focus	0.6	1.8
15 cm x 15 cm	EGS4	1.2	2.3
	Helax	0.2	1.4
	Focus	0.5	0.6

The 2.3 % deviation in the 15 cm x 15 cm Monte Carlo data set may initially be considered unsatisfactory, however the uncertainty in the corresponding dose value was ± 0.5 %. This implies that the EGS4 data met the ± 2% target within the limits of statistical uncertainty.

Tables 4.3 and 4.4 indicate that the 10 cm x 10 cm Helax distribution was significantly less accurate than either the Monte Carlo or Focus distributions. In fact the homogeneous dose distribution predicted by Helax for the 18 MeV 10 cm x 10 cm field was found to be consistent with depth *ionization* data obtained under these same conditions. The maximum and mean percentage deviations between the Helax PDD and the measured depth ionization data over a range of depths extending from the water surface to R_{50} were found to be 0.36% and 0.13% respectively. It was inferred that depth ionization values were erroneously used in place of depth dose data when the Helax

planning system was configured for the linear accelerator used for these measurements. A similar impropriety could not be verified for any other homogeneous field size or energy.

These discrepancies between homogeneous dose distributions again emphasize the importance of using dose ratios to correct the inhomogeneous PDDs before evaluating algorithm performance. The 18 MeV 10 cm x 10 cm depth ionization data was used to demonstrate the effectiveness of the ratio correction. This analysis is presented in appendix III.

4.1.2 Homogenous Dose Profiles

A comparison between Monte Carlo dose profiles and measured data was performed in order to verify the accuracy of the phase space files generated by BEAM. The transverse profiles in figures 4.3 through 4.6 are plotted for three different depths, and are normalized to the value of the measured central axis PDD. The right and left field positions at which each profile fell below 50% of the maximum of the corresponding Boltzman fit (equation 3.2) were recorded as $\pm X_{1/2}$ and are included directly on each figure. Figures 4.3 and 4.4 illustrate the behavior of 9 MeV homogeneous profiles for 10 cm x 10 cm and 15 cm x 15 cm field sizes respectively. Figures 4.5 and 4.6 represent the analogous 18 MeV profiles.

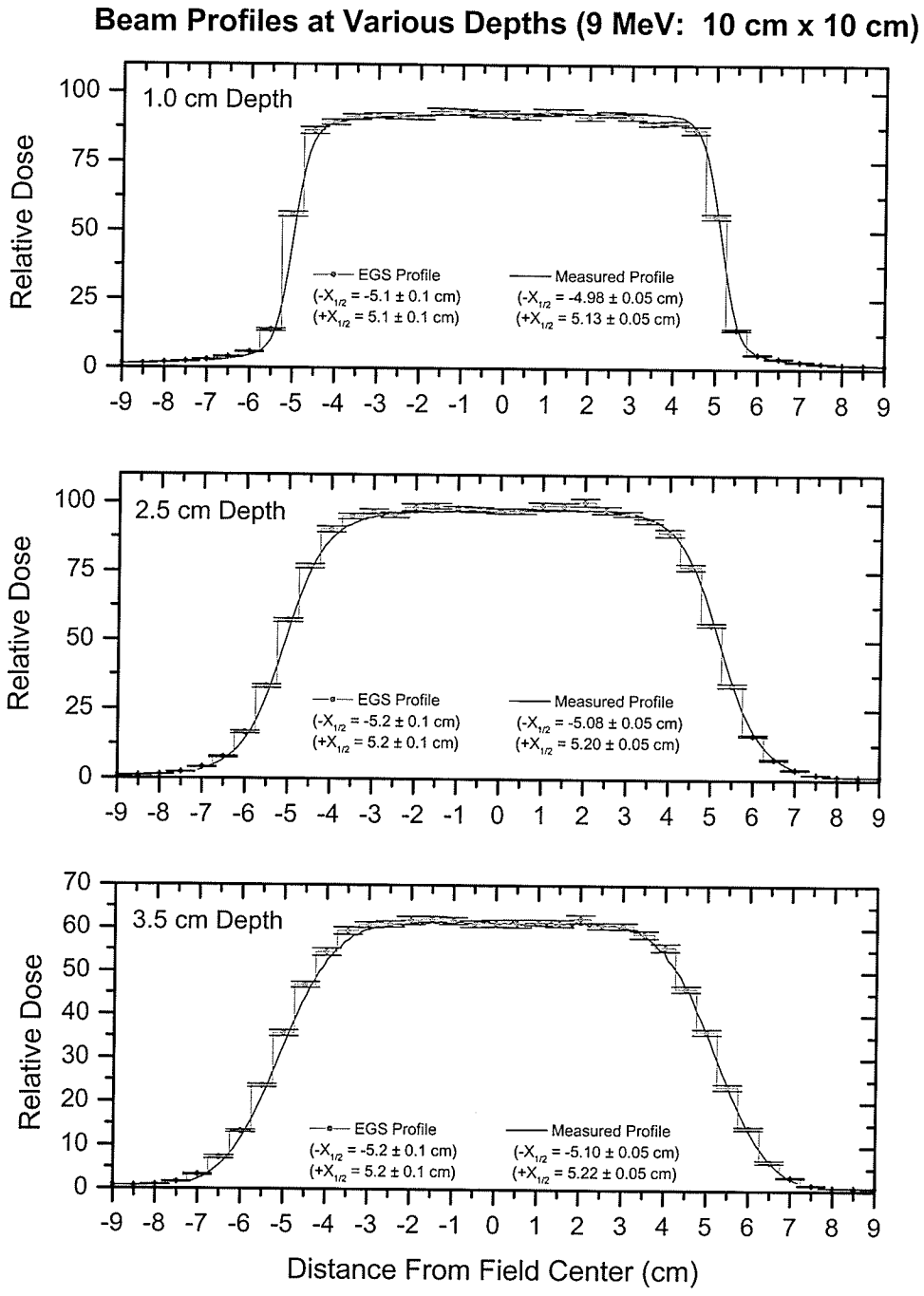

Figure 4.3 Homogeneous electron dose profiles at three different depths in water. The beam energy was 9 MeV, and the field size was 10 cm x 10 cm.. The $\pm X_{1/2}$ parameters correspond to the distance from the center of the field at which the profile drops to half of its maximum value.

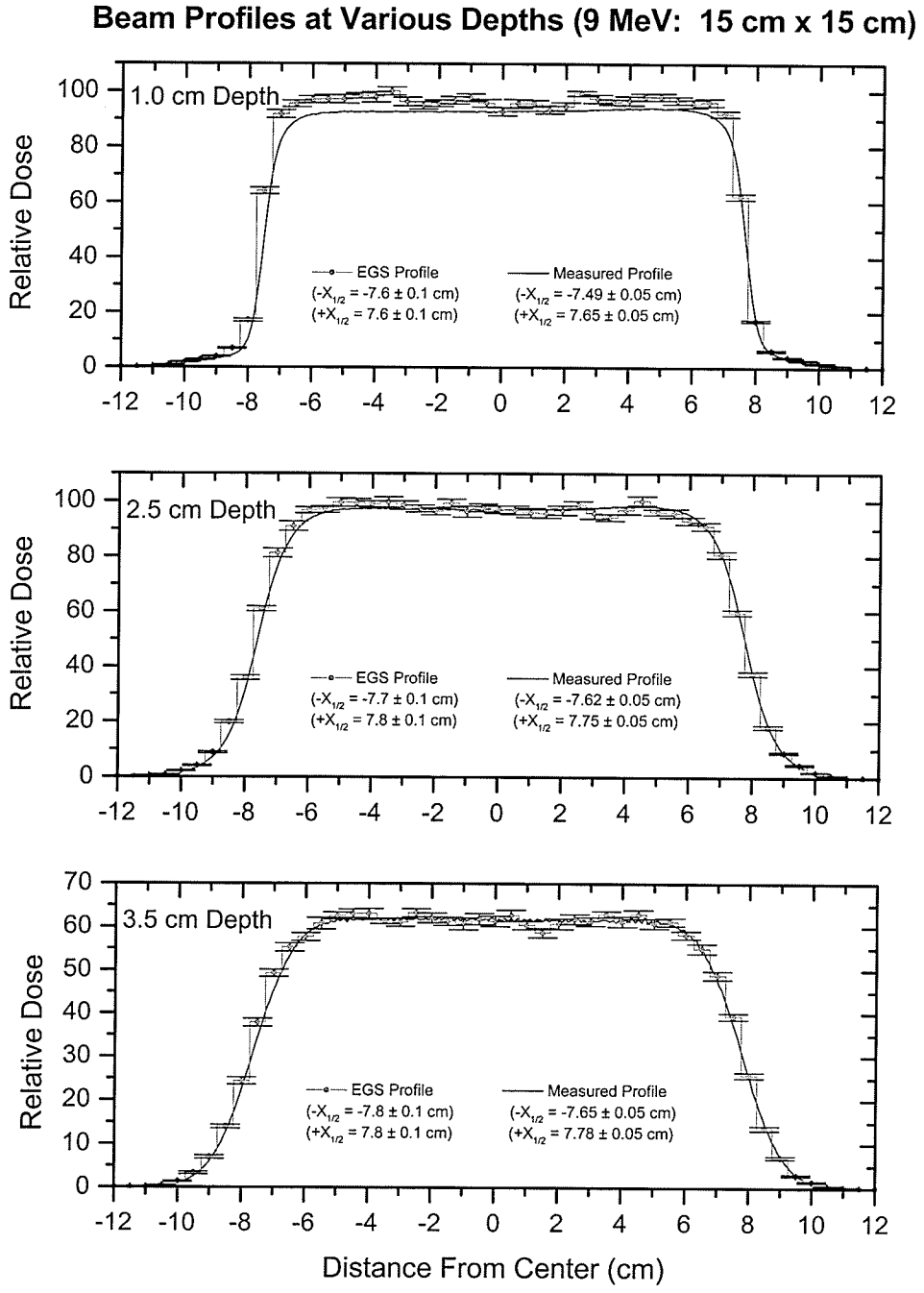

Figure 4.4 Homogeneous electron dose profiles at three different depths in water. The beam energy was 9 MeV, and the field size was 15 cm x 15 cm.. The $\pm X_{1/2}$ parameters correspond to the distance from the center of the field at which the profile drops to half of its maximum value.

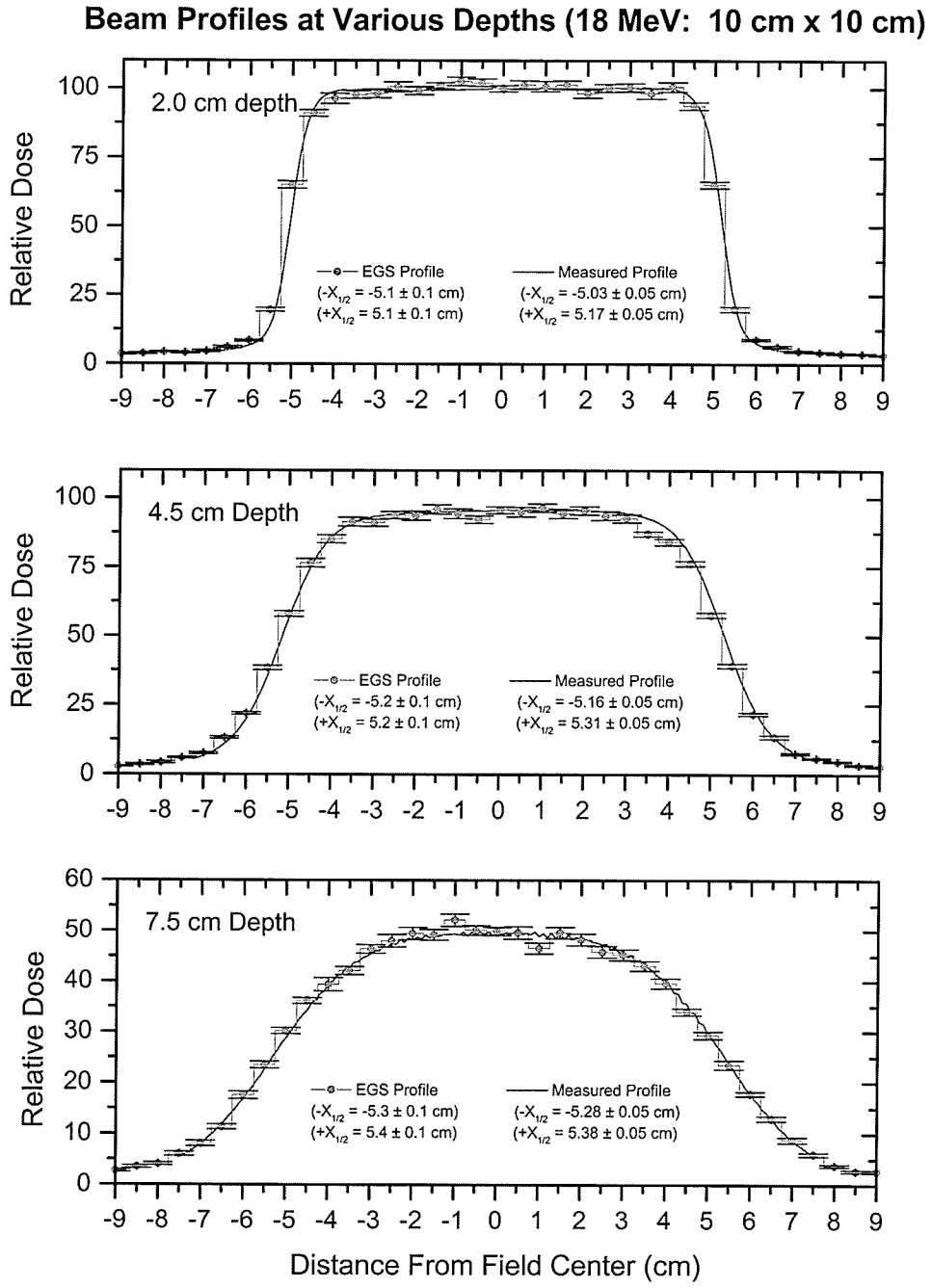

Figure 4.5 Homogeneous electron dose profiles at three different depths in water. The beam energy was 18MeV, and the field size was 10 cm x 10 cm.. The $\pm X_{1/2}$ parameters correspond to the distance from the center of the field at which the profile drops to half of its maximum value.

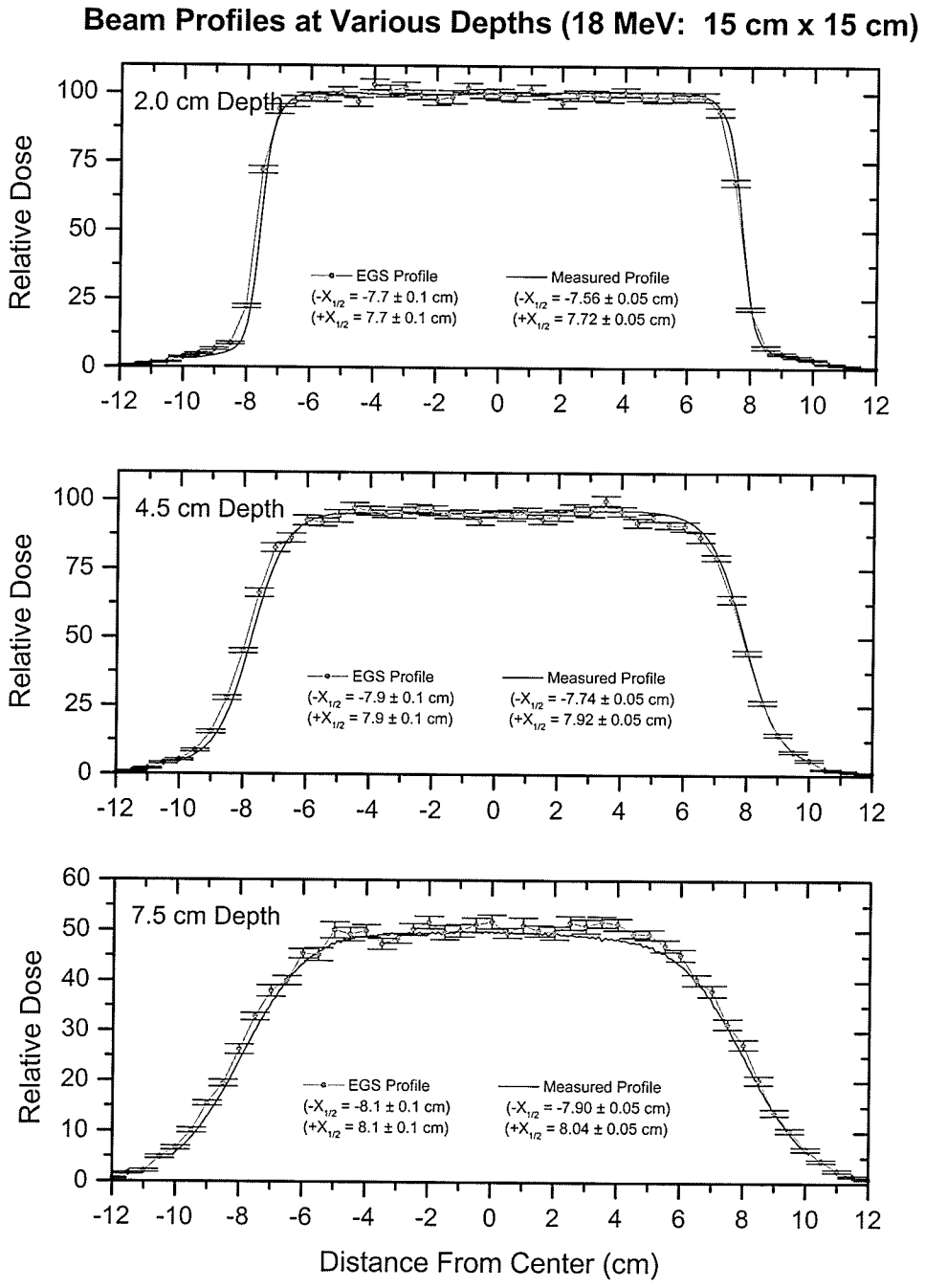

Figure 4.6 Homogeneous electron dose profiles at three different depths in water. The beam energy was 18MeV, and the field size was 15 cm x 15 cm.. The $\pm X_{1/2}$ parameters correspond to the distance from the center of the field at which the profile drops to half of its maximum value.

All $X_{1/2}$ parameters obtained from the Monte Carlo data set were within 2 mm of the corresponding measured values. Furthermore, the distance between $+X_{1/2}$ and $-X_{1/2}$, when extrapolated to the water surface, differed by less than 2 mm from the nominal field size in all cases. This close agreement was judged to be more than adequate for the central axis calculations considered in this work.

4.2 Dose Distributions Beneath Slab Inhomogeneities

Dosimetric calculations in the presence of slab-shaped inhomogeneities are presented in the following sub sections. Both Focus and Helax make use of the semi-infinite slab approximation when calculating electron dose distributions. Since the slab geometry considered in this work satisfied this approximation, dosimetric predictions beneath slab inhomogeneities were expected to be very reasonable. Van Dyk has suggested a target accuracy of ± 5 % for central axis dose calculations beneath slab inhomogeneities.[5]

4.2.1 9 MeV Beam

4.2.1.1 Verification of Monte Carlo Calculations

Dose measurements were used to verify the dosimetric accuracy of EGS4 Monte Carlo simulations beneath air and aluminum slabs. These measurements were performed

using TLDs and the PMMA phantom described in section 3.1. The slab inhomogeneities used were placed below 0.635 cm of PMMA, and had thicknesses of 0.3175 cm (air) and 0.635 (aluminum). The results of these measurements are shown in figure 4.7. Both homogeneous and inhomogeneous measurements were used in equation (3.4) to produce the corrected inhomogeneous data shown.

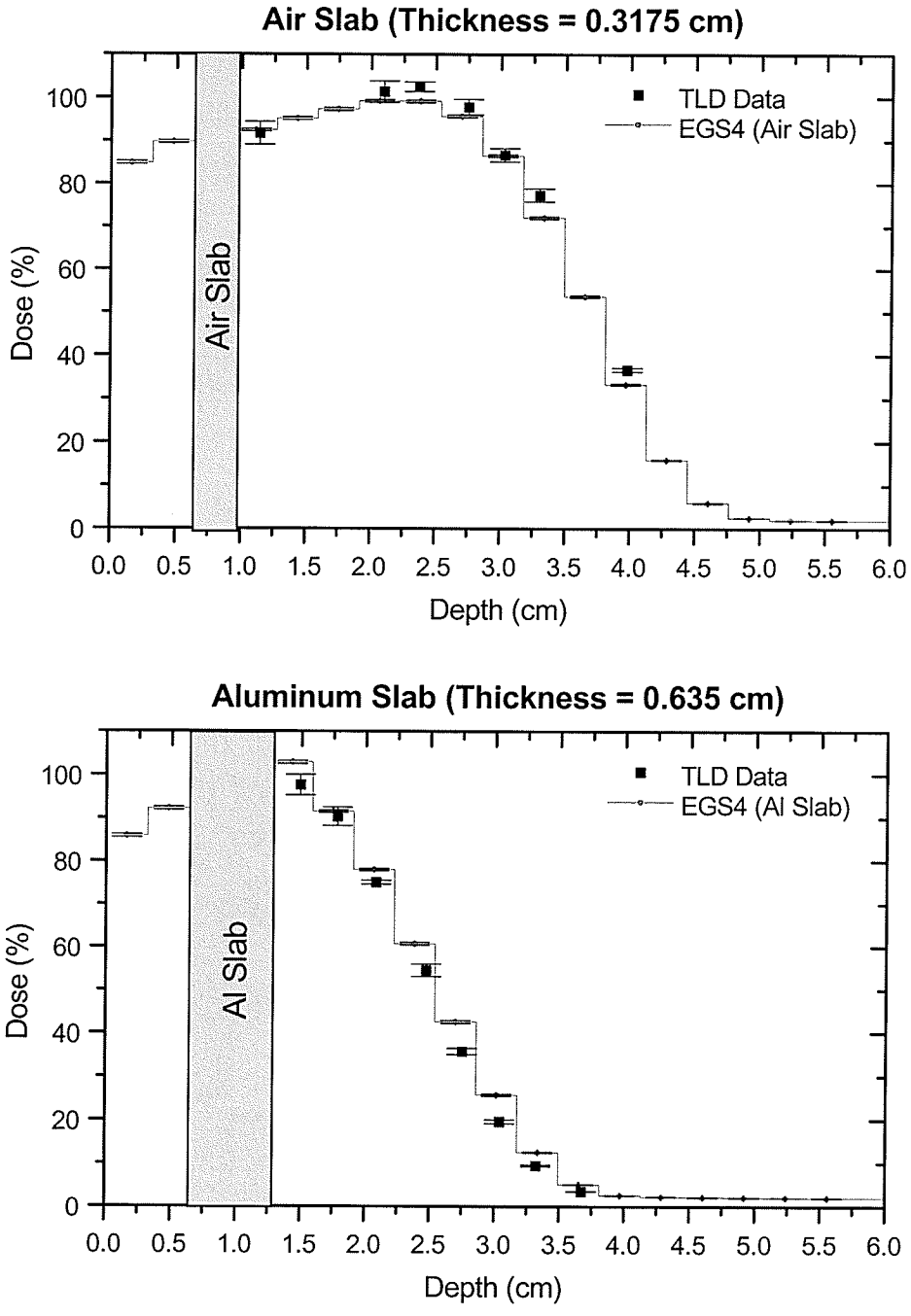

Figure 4.7 TLD measurements (square points) are shown here for a PMMA phantom containing slab inhomogeneities. The Monte Carlo data and the TLD measurements differ by less than 5 %, verifying the ability of EGS4 to accurately predict the dose behind air and aluminum slabs in PMMA. The beam energy was 9 MeV, and the field size was 10 cm x 10 cm.

Differences between the Monte Carlo predictions and TLD measurements shown in figure 4.7 were found to be within the ± 5 % target. The EGS4 simulations were therefore determined to yield an accurate representation of the 9 MeV electron dose distribution beneath slab inhomogeneities in a PMMA phantom. As discussed in section 2.4.5, EGS4 was expected to yield a similar accuracy if the phantom were composed of water.

4.2.1.2 10 cm x 10 cm Field

Figures 4.8 - 4.10 illustrate the dosimetric predictions calculated for a slab phantom exposed to a 10 cm x 10 cm beam of 9 MeV electrons. The slab thickness is illustrated on a scale identical to that of the bottom (depth) axis. The top graph of each figure shows the predictions for an air slab, while the bottom figure gives the results for an aluminum slab.

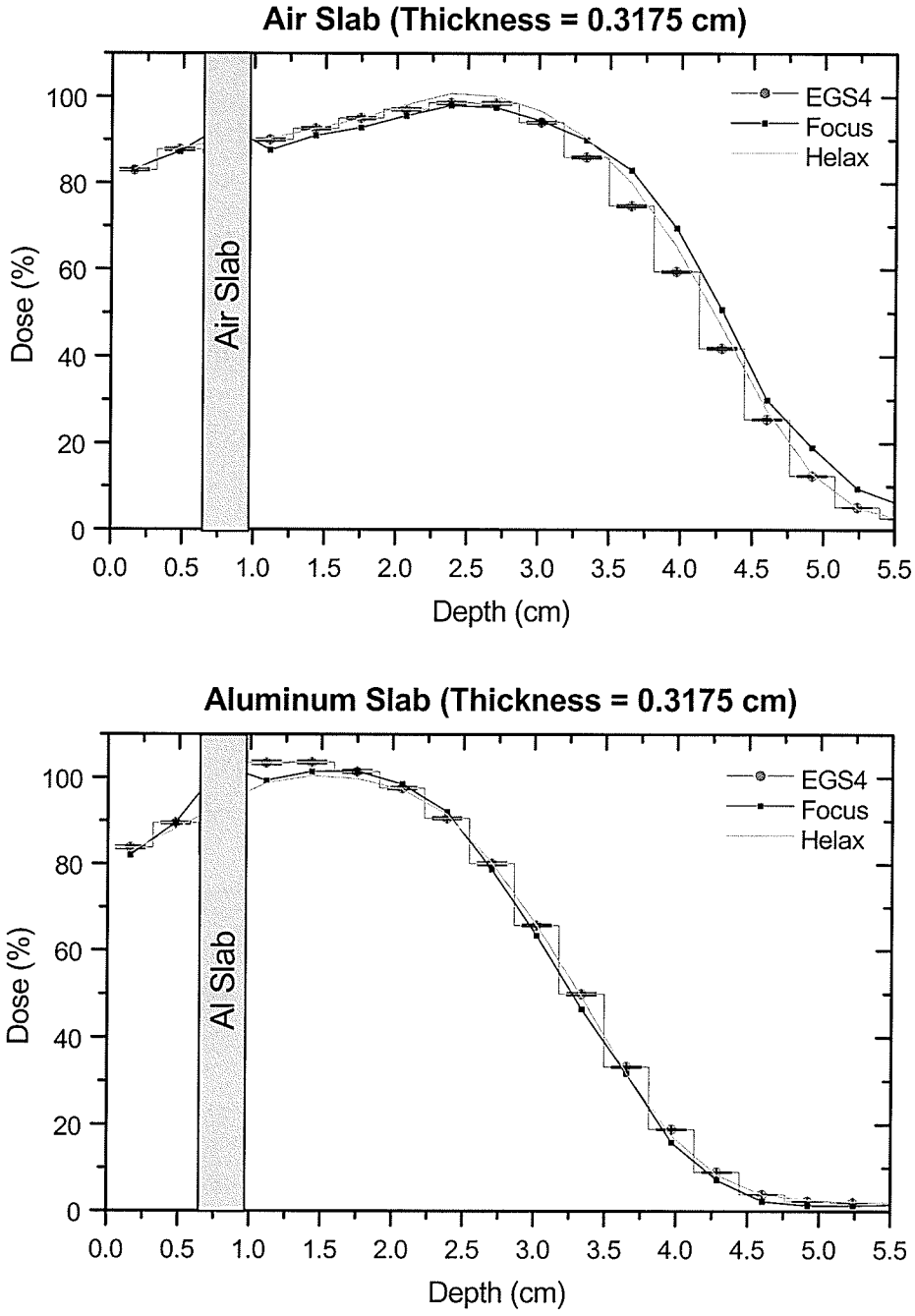

Figure 4. 8 This figure illustrates the dose distributions predicted beneath a 0.3175 cm thick slab, located 0.635 cm below the surface of a water phantom. The beam energy was 9 MeV, and the field size was 10 cm x 10 cm.

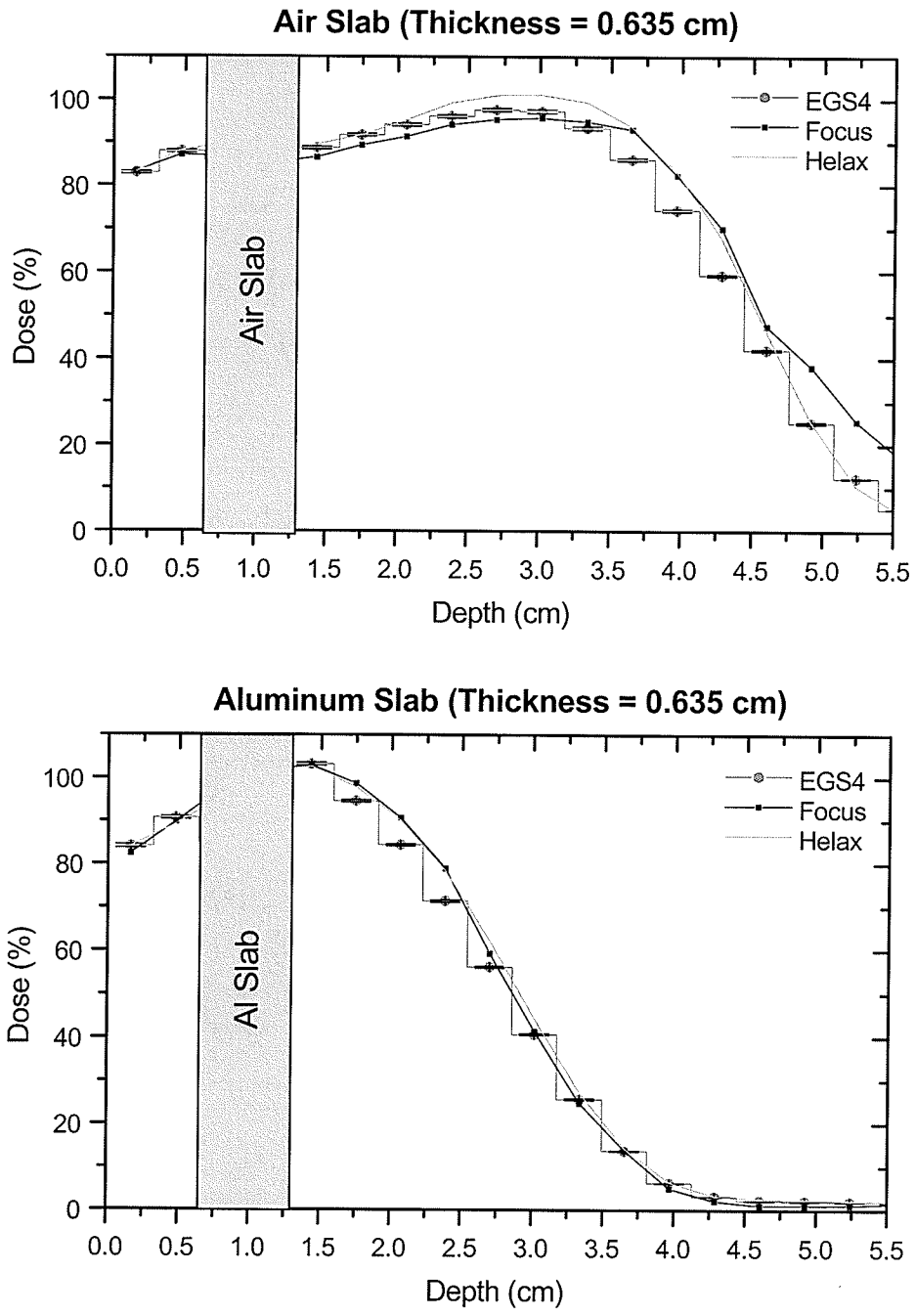

Figure 4. 9 This figure illustrates the dose distributions predicted beneath a 0.635 cm thick slab, located 0.635 cm below the surface of a water phantom. The beam energy was 9 MeV, and the field size was 10 cm x 10 cm.

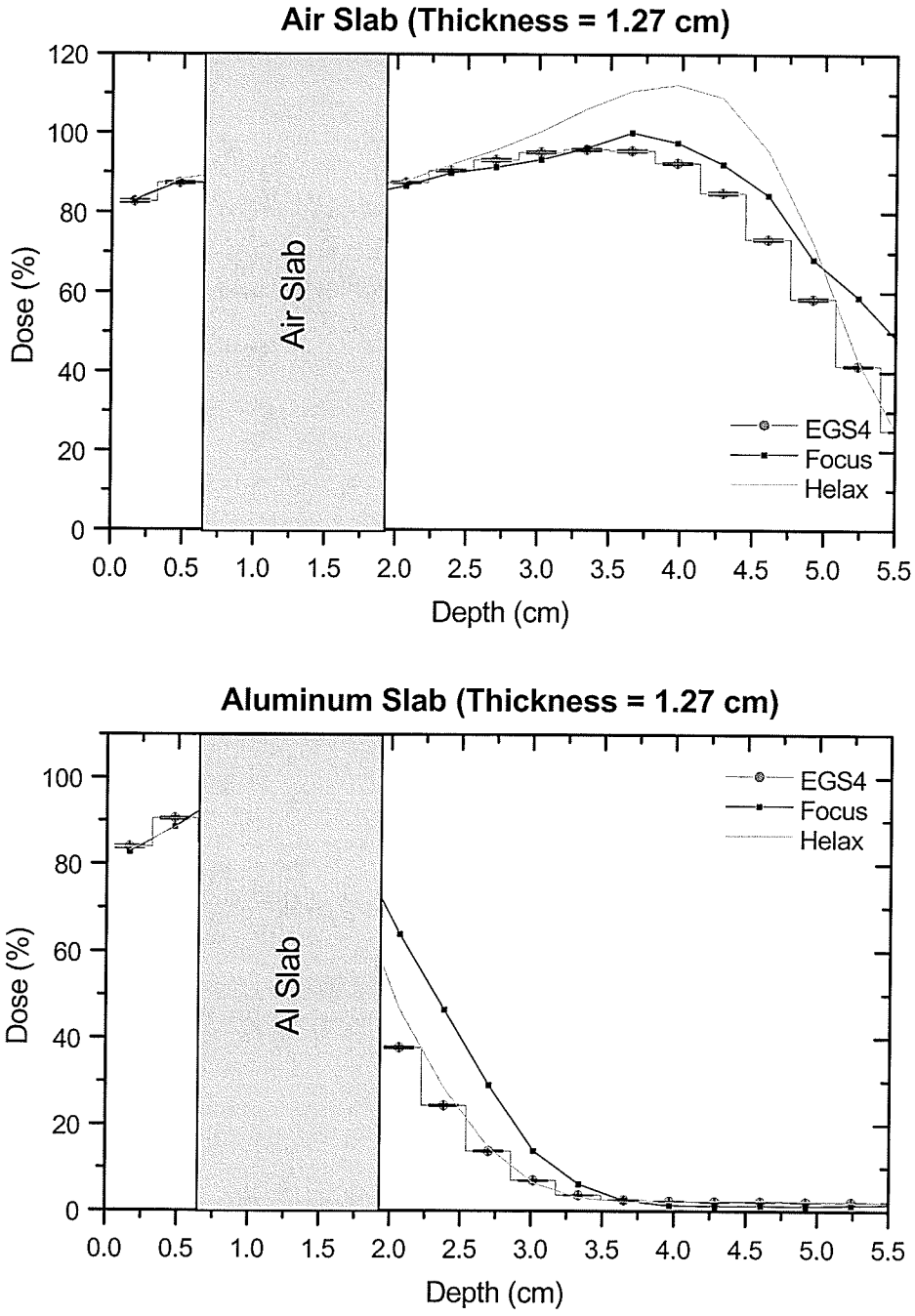

Figure 4. 10 This figure illustrates the dose distributions predicted beneath a 1.27 cm thick slab, located 0.635 cm below the surface of a water phantom. The beam energy was 9 MeV, and the field size was 10 cm x 10 cm. This very thick slab geometry is not of direct clinical interest.

From these figures it can be seen that both the Helax and Focus results deviated significantly from the Monte Carlo predictions. A qualitative examination of these curves revealed that both treatment planning systems had a tendency to over predict the dose in the descending portion of the distribution. Helax had difficulties predicting the dose beyond the thickest air slab. Interestingly, when the material of the thickest slab was changed to aluminum Focus yielded the worse prediction. To allow for a more quantitative analysis, the maximum and mean deviations between Monte Carlo and treatment planning predictions were calculated. Table 4.5 lists these results for slabs of increasing thickness T.

Table 4.5 Summary of the deviation between Monte Carlo and treatment planning calculations for a slab inhomogeneity. The beam energy was 9 MeV and the field size was 10 cm x 10 cm. Tabulated values have been expressed as a percentage of the central axis normalization dose. Quoted slab thicknesses correspond to the simulated geometry, these dimensions were reproduced to within ± 0.1 cm on the treatment planning systems.

		Data Above R_{80}				**Data Above R_{50}**			
		Mean Dev. (%)		Max Dev. (%)		Mean Dev. (%)		Max Dev. (%)	
		FOCUS	*HELAX*	*FOCUS*	*HELAX*	*FOCUS*	*HELAX*	*FOCUS*	*HELAX*
Slab T =	*Air*	1.7	1.6	4.0	4.5	3.2	2.4	10.1	5.8
0.3175 cm	*Al*	1.7	1.8	4.1	4.7	2.0	1.5	4.1	4.7
Slab T =	*Air*	2.7	3.2	7.0	7.5	4.0	4.3	10.9	8.9
0.635 cm	*Al*	3.6	3.2	6.3	5.7	4.3	4.5	7.5	7.0
Slab T =	*Air*	2.8	9.9	7.2	24.1	5.5	10.6	17.2	24.1
1.27 cm	*Al*	Dose beneath slab < 80 %				Dose beneath slab < 50 %			

From these data it was observed that the accuracy of treatment planning predictions degraded as slab thickness was increased. With the exception of the thickest slab, the behavior of Focus and Helax was very similar.

A three level rating system was introduced to summarize treatment planning performance. This approach is based upon the ± 5 % target accuracy specified by Van Dyk [5] for electron dose calculations in the presence of slab-shaped inhomogeneities. In the past [37] electron dose calculations have been considered satisfactory when one standard deviation of the dosimetric calculations were within the Van Dyk criteria. The rating scheme presented here differs from this approach in that a maximum allowable deviation is specified. Furthermore, the same rating scheme is used for both slab-shaped and cylindrical inhomogeneities. A rating of 'Pass' was assigned if the maximum deviation between Monte Carlo and treatment planning doses was below 5 %. A rating of 'Indeterminate' was assigned if the mean deviation was less than 5 % but the maximum deviation was between 5 % and 10 %. Finally, if the mean deviation exceeded 5 % or the maximum deviation exceeded 10 % the dosimetric prediction was considered a 'Failure'. These ranking criteria are summarized in table 4.6.

Table 4.6 Summary of performance rating criteria. Maximum and mean deviations are expressed as percentages of the central axis normalization dose.

Rating	Criteria for Qulaification
Pass	Max Dev. ≤ 5 %
Indeterminate	Mean Dev. ≤ 5 % *and* 5 % ≤ Max Dev. ≤ 10 %
Failure	Mean Dev. > 5 % *or* Max Dev. > 10 %

Table 4.7 Performance Ratings for Slabs. The beam energy was 9 MeV, and the field size was 10 cm x 10 cm. Quoted slab thicknesses correspond to the simulated geometry, these dimensions were reproduced to within ± 0.1 cm on the treatment planning systems.

		Data Above R_{80}		Data Above R_{50}	
		FOCUS	*HELAX*	*FOCUS*	*HELAX*
Slab T =	*Air*	Pass	Pass	Failure	Indeterminate
0.3175 cm	*Al*	Pass	Pass	Pass	Pass
Slab T =	*Air*	Indeterminate	Indeterminate	Failure	Indeterminate
0.635 cm	*Al*	Indeterminate	Indeterminate	Indeterminate	Indeterminate
Slab T =	*Air*	Indeterminate	Failure	Failure	Failure
1.27 cm	*Al*	Dose beneath slab < 80 %		Dose beneath slab < 50 %	

4.2.1.3 15 cm x 15 cm Field

Since a large degree of correlation was expected to exist between the dosimetric predictions for a 10 cm x 10 cm field and a 15 cm x 15 cm field, only one slab thickness was considered for the larger field size at this energy. The depth dose prediction beyond a 0.635 cm thick slab are plotted in figure 4.11. The inaccuracy illustrated in these two graphs was quantified in table 4.8, and the corresponding performance rating for each treatment planning system is given in table 4.9

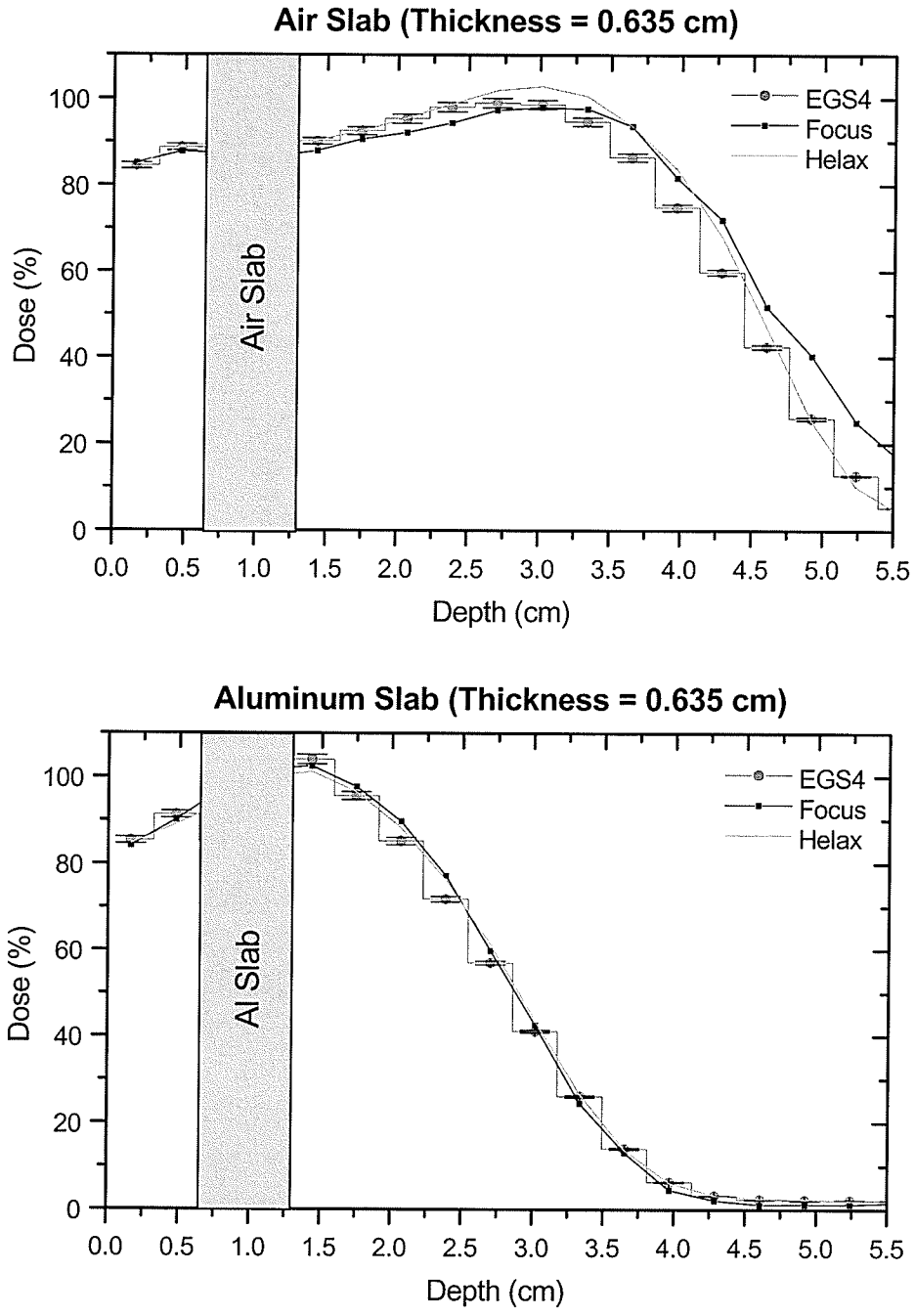

Figure 4. 11 This figure illustrates the dose distributions predicted beneath a 0.635 cm thick slab, located 0.635 cm below the surface of a water phantom. The beam energy was 9 MeV, and the field size was 15cm x 15cm.

Table 4.8 Summary of the deviation between Monte Carlo and treatment planning calculations for a slab inhomogeneity. The beam energy was 9 MeV and the field size was 15 cm x 15 cm. Tabulated values have been expressed as a percentage of the central axis normalization dose. The quoted slab thickness corresponds to the simulated geometry, this value was reproduced to within ± 0.1 cm on the treatment planning systems.

		Data Above R_{80}				**Data Above R_{50}**			
		Mean Dev. (%)		Max Dev. (%)		Mean Dev. (%)		Max Dev. (%)	
		FOCUS	*HELAX*	*FOCUS*	*HELAX*	*FOCUS*	*HELAX*	*FOCUS*	*HELAX*
Slab T =	*Air*	2.9	2.7	7.2	7.2	4.3	3.9	12.2	8.9
0.635 cm	*Al*	2.7	2.2	4.5	3.0	3.3	3.1	5.5	4.4

Dosimetric predictions behind the air slab were similar to those obtained for the 10 cm x 10 cm field. Predictions beneath the aluminum slab were improved.

Table 4.9 Performance Ratings for Slabs. The beam energy was 9 MeV, and the field size was 15 cm x 15 cm. The quoted slab thickness corresponds to the simulated geometry, which was reproduced to within ± 0.1 cm on the treatment planning systems.

		Data Above R_{80}		**Data Above R_{50}**	
		FOCUS	*HELAX*	*FOCUS*	*HELAX*
Slab T =	*Air*	Indeterminate	Indeterminate	Failure	Indeterminate
0.635 cm	*Al*	Pass	Pass	Indeterminate	Pass

4.2.2 18 MeV Beam

4.2.2.1 Verification of Monte Carlo Calculations

TLD measurements and Monte Carlo calculations of the dose deposited beneath either air or aluminum slabs within a PMMA phantom exposed to an 18 MeV electron beam are plotted in figure 4.12. The slab inhomogeneities tested in this case had a thickness of 1.27 cm, and were placed below 1.27 cm of PMMA. Once again all predictions were within ± 5 % of measured values. This close agreement served as a verification of the ability of EGS4 to accurately calculate the measured dose deposited beneath slab inhomogeneities by an 18 MeV electron beam produced by the KD2-B.

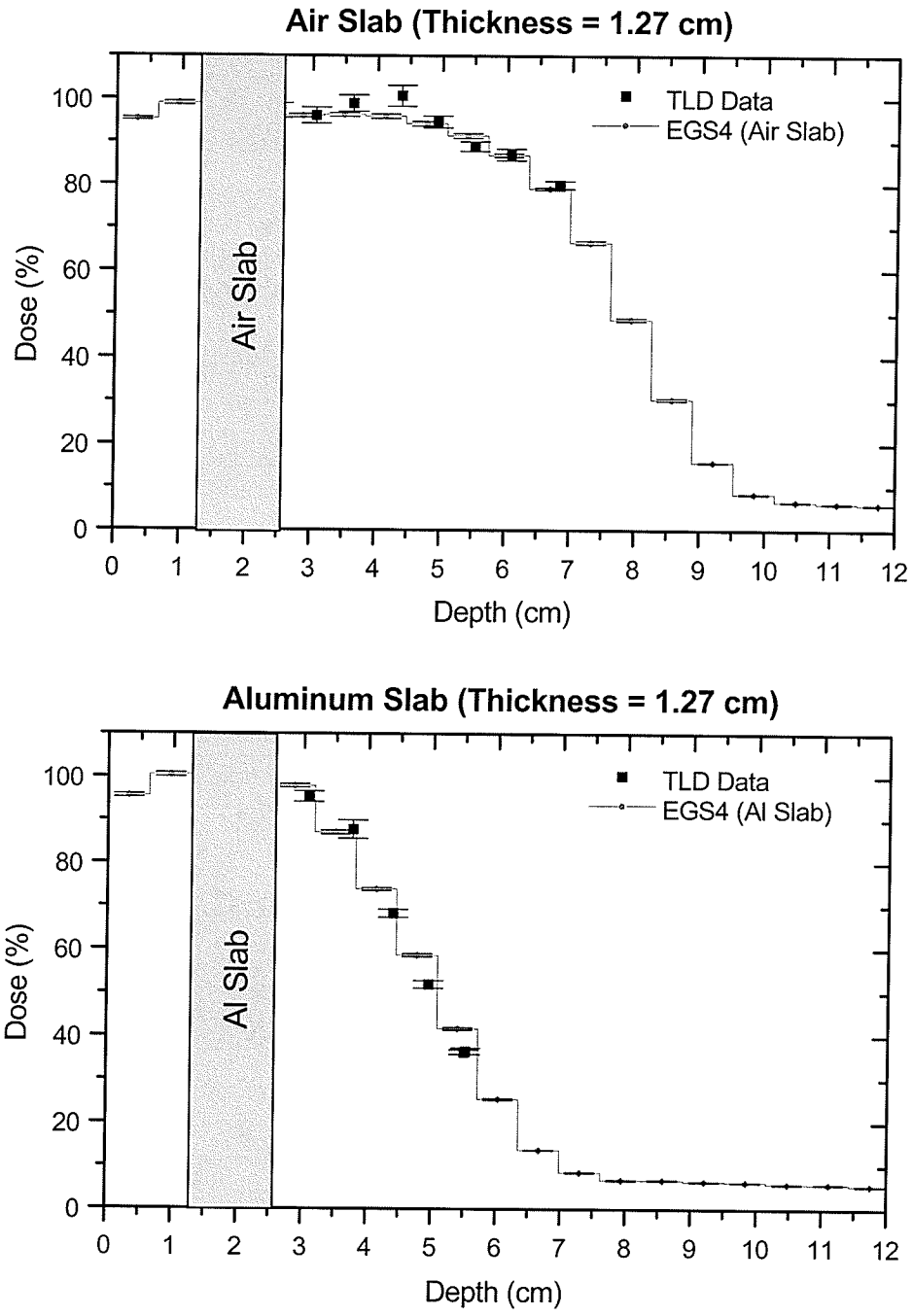

Figure 4. 12 TLD measurements (square points) are shown here for a PMMA phantom containing a slab inhomogeneity. The Monte Carlo data and the TLD measurements differ by less than 5 %, verifying the ability of EGS4 to accurately predict the dose behind air and aluminum slabs in PMMA. The beam energy was 18 MeV, and the field size was 10 cm x 10 cm.

4.2.2.2 10 cm x 10 cm Field

The dose distributions predicted behind the three slabs considered with the 18 MeV beam are shown in figures 4.13 - 4.15. The accuracy of these curves is summarized in table 4.10. As in the 9 MeV investigation, it was found that predictions became less accurate as slab thickness increased, with a tendency toward over prediction. In the case of the air slabs, this progressive inaccuracy was more rapid for Helax than it was for Focus. However, for the aluminum slabs the quality of the Focus predictions was observed to degrade more quickly. It was observed that Focus predictions beneath aluminum slabs were significantly less accurate than they were in the 9 MeV case. They were also much less accurate than their Helax counterparts.

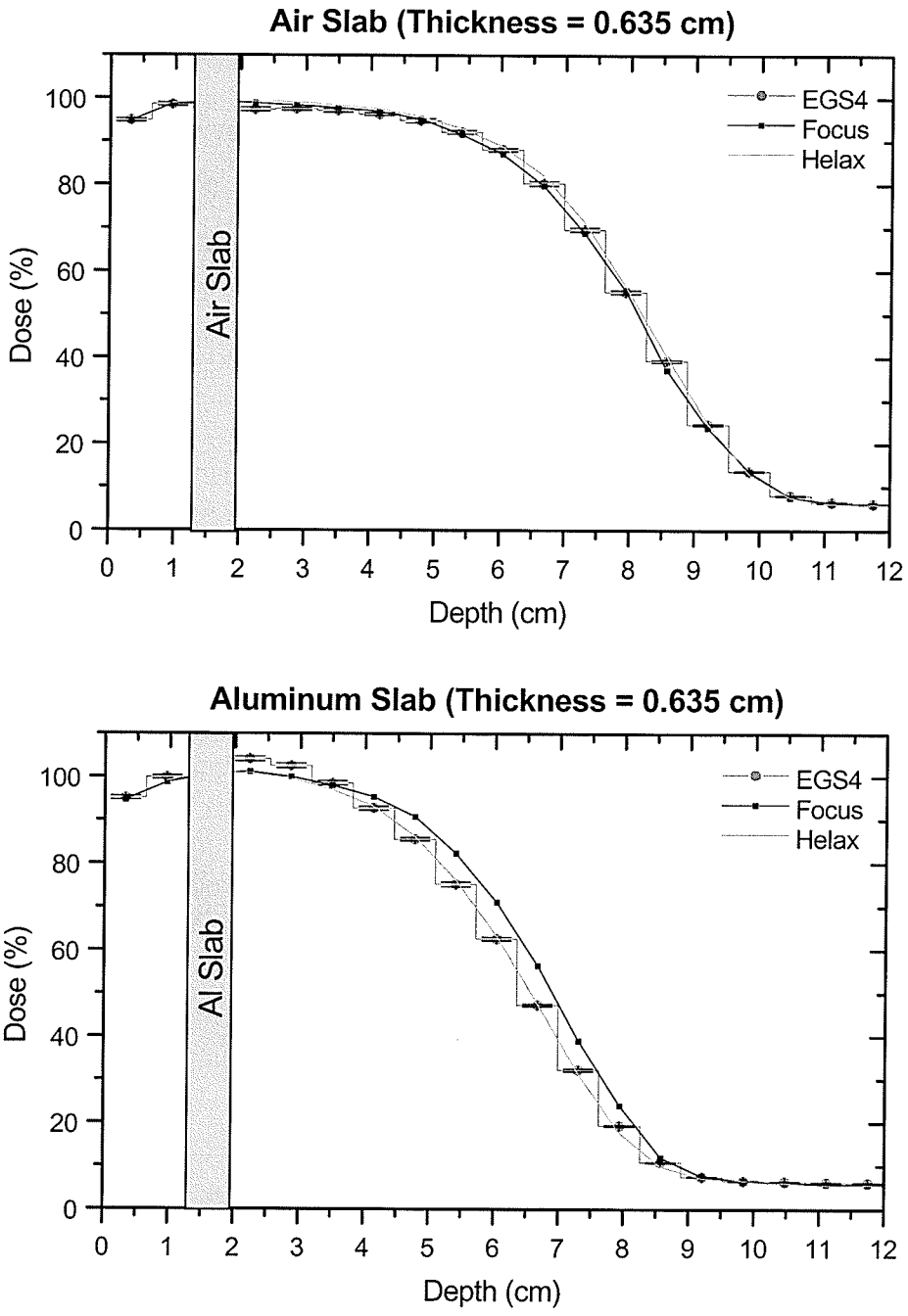

Figure 4. 13 This figure illustrates the dose distributions predicted beneath a 0.635 cm thick slab, located 1.27 cm below the surface of a water phantom. The beam energy was 18 MeV, and the field size was 10 cm x 10 cm.

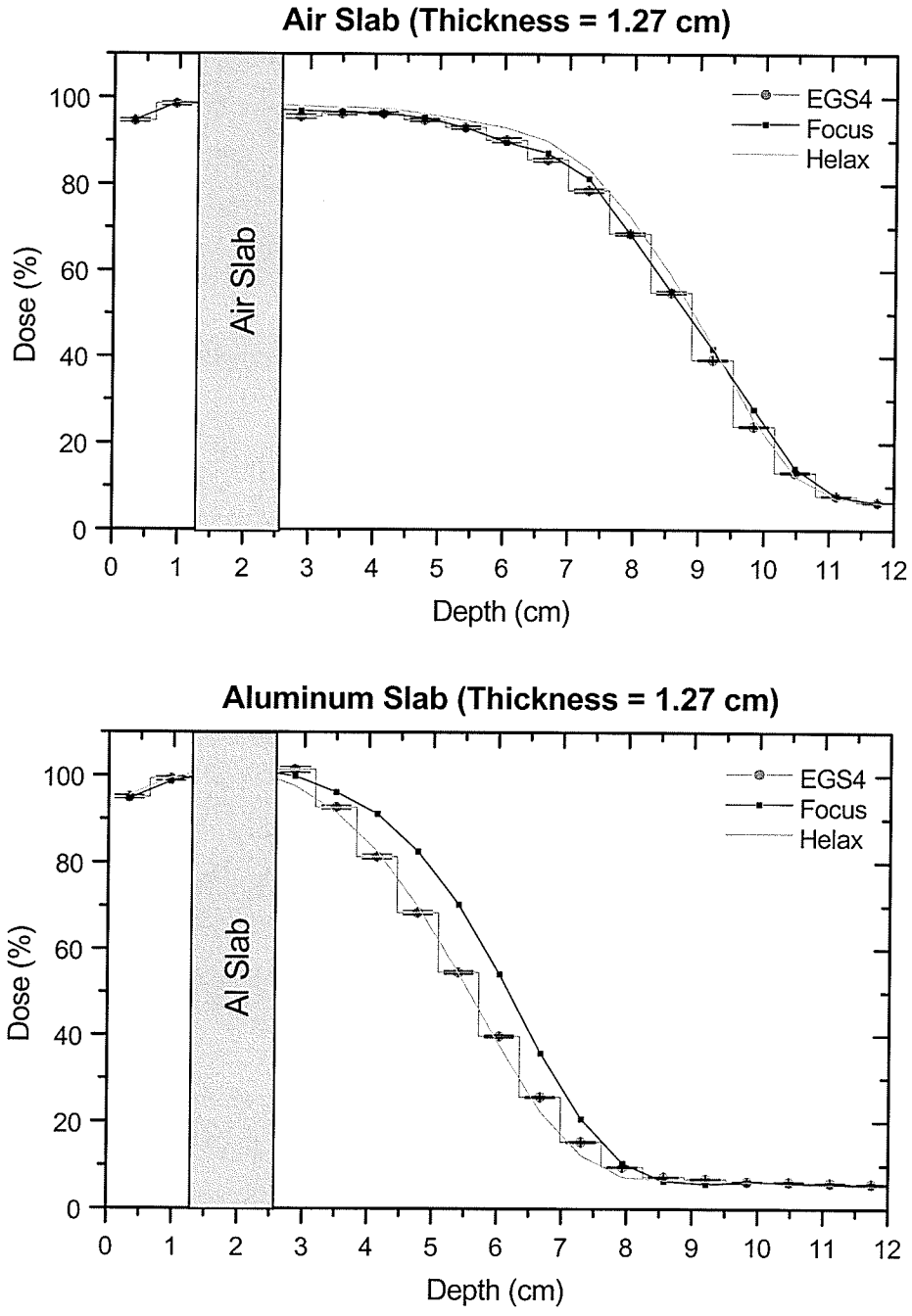

Figure 4. 14 This figure illustrates the dose distributions predicted beneath a 1.27 cm thick slab, located 1.27 cm below the surface of a water phantom. The beam energy was 18 MeV, and the field size was 10 cm x 10 cm.

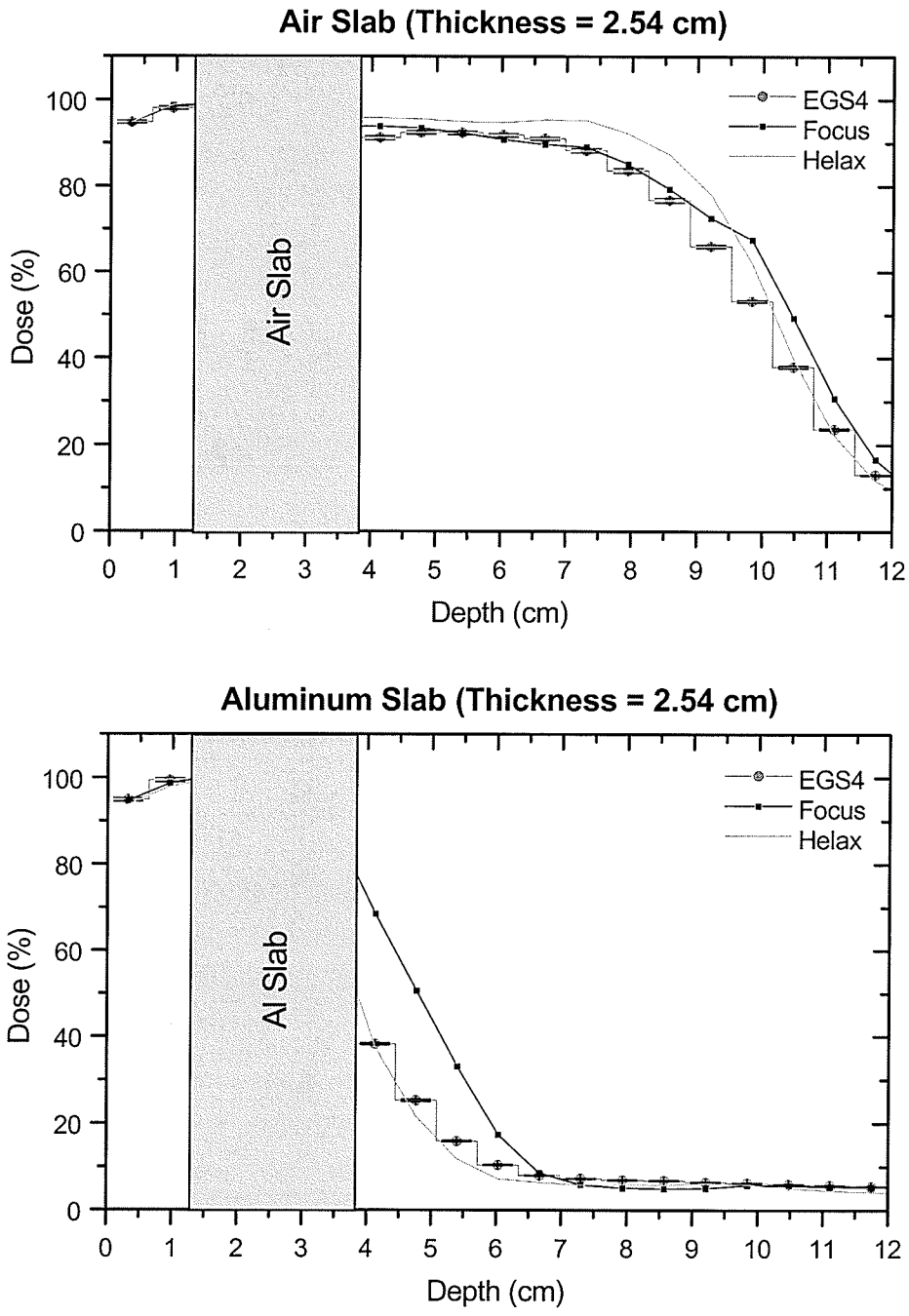

Figure 4. 15 This figure illustrates the dose distributions predicted beneath a 2.54 cm thick slab, located 1.27 cm below the surface of a water phantom. The beam energy was 18 MeV, and the field size was 10 cm x 10 cm. This very thick slab geometry is not of direct clinical interest.

Table 4.10 Summary of the deviation between Monte Carlo and treatment planning calculations for a slab inhomogeneity. The beam energy was 18 MeV and the field size was 10 cm x 10 cm. Tabulated values have been expressed as a percentage of the central axis normalization dose. Quoted slab thicknesses correspond to the simulated geometry, these dimensions were reproduced to within ± 0.1 cm on the treatment planning systems.

		Data Above R_{80}				**Data Above R_{50}**			
		Mean Dev. (%)		Max Dev. (%)		Mean Dev. (%)		Max Dev. (%)	
		FOCUS	*HELAX*	*FOCUS*	*HELAX*	*FOCUS*	*HELAX*	*FOCUS*	*HELAX*
Slab T =	*Air*	0.8	1.3	1.5	1.9	0.7	1.3	1.5	1.9
0.635 cm	*Al*	2.8	1.8	5.2	3.2	4.2	1.5	8.4	3.2
Slab T =	*Air*	0.6	2.2	1.6	4.3	0.7	2.6	2.7	4.9
1.27 cm	*Al*	7.2	1.9	14.1	3.7	9.9	1.6	15.7	3.7
Slab T =	*Air*	1.2	4.7	2.7	8.6	3.2	6.4	14.3	12.0
2.54 cm	*Al*	Dose beneath slab < 80 %				Dose beneath slab < 50 %			

The performance rating scheme outlined in table 4.6. was employed to classify these results as either: a pass, as indeterminate, or as a failure. The results are tabulated in table 4.11

Table 4.11 Performance Ratings for Slabs. The beam energy was 18 MeV, and the field size was 10 cm x 10 cm. Quoted slab thicknesses correspond to the simulated geometry, these dimensions were reproduced to within ± 0.1 cm on the treatment planning systems.

		Data Above R_{80}		Data Above R_{50}	
		FOCUS	*HELAX*	*FOCUS*	*HELAX*
Slab T = 0.635 cm	*Air*	Pass	Pass	Pass	Pass
	Al	Indeterminate	Pass	Indeterminate	Pass
Slab T = 1.27 cm	*Air*	Pass	Pass	Pass	Pass
	Al	Failure	Pass	Failure	Pass
Slab T = 2.54 cm	*Air*	Pass	Indeterminate	Failure	Failure
	Al	Dose beneath slab < 80 %		Dose beneath slab < 50 %	

4.2.2.3 15 cm x 15 cm Field

Only one slab inhomogeneity was considered for the 15 cm x 15 cm field with a beam energy of 18 MeV. The slab was 1.27 cm thick, and located beneath 1.27 cm of water. Results are presented in figure 4.16 as well as Tables 4.12 and 4.13. Results for an incident field size of 15 cm x 15 cm were similar to those for the 10 cm x 10 cm field shown in figure 4.14.

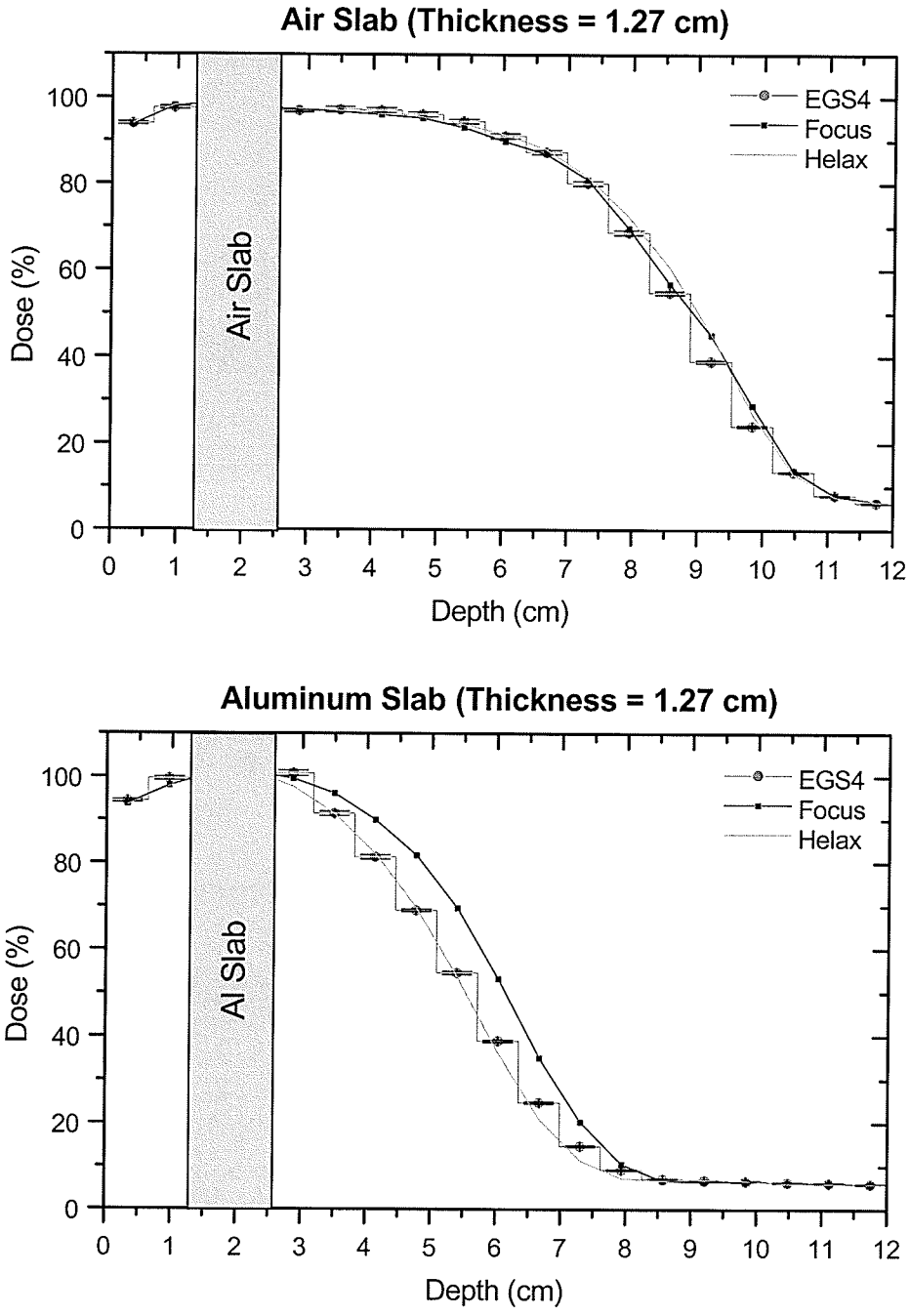

Figure 4. 16 This figure illustrates the dose distributions predicted beneath a 1.27 cm thick slab, located 1.27 cm below the surface of a water phantom. The beam energy was 18 MeV, and the field size was 15 cm x 15 cm.

Table 4.12 Summary of the deviation between Monte Carlo and treatment planning calculations for a slab inhomogeneity. The beam energy was 18 MeV and the field size was 15 cm x 15 cm. Tabulated values have been expressed as a percentage of the central axis normalization dose. The quoted slab thickness corresponds to the simulated geometry, this value was reproduced to within ± 0.1 cm on the treatment planning systems.

		Data Above R80				**Data Above R50**			
		Mean Dev. (%)		Max Dev. (%)		Mean Dev. (%)		Max Dev. (%)	
		FOCUS	*HELAX*	*FOCUS*	*HELAX*	*FOCUS*	*HELAX*	*FOCUS*	*HELAX*
Slab T =	*Air*	0.8	0.7	1.4	1.5	1.0	1.5	2.0	5.7
1.27	*Al*	4.9	1.3	8.7	3.1	8.5	1.1	15.0	3.1

Table 4.13 Performance Ratings for Slabs. The beam energy was 18 MeV, and the field size was 15 cm x 15 cm. The quoted slab thickness corresponds to the simulated geometry, which was reproduced to within ± 0.1 cm on the treatment planning systems.

		Data Above R_{80}		**Data Above R_{50}**	
		FOCUS	*HELAX*	*FOCUS*	*HELAX*
Slab T =	*Air*	Pass	Pass	Pass	Intermediate
0.635 cm	*Al*	Intermediate	Pass	Failure	Pass

4.3 Dose Distributions Beneath Cylindrical Inhomogeneities

Neither treatment planning system was expected to provide an accurate representation of the dose distribution beneath small cylindrical inhomogeneities. As discussed in section 2.3, the anticipated failure of the semi-infinite slab approximation was expected to yield under-predicted doses in the hot spots behind air cylinders and

over-predicted doses in the cold spots behind aluminum cylinders.

4.3.1 9 MeV Beam

4.3.1.1 Monte Carlo Verification

The accuracy with which EGS4 simulations matched TLD measurements was investigated for cylindrical inhomogeneities 0.635 cm in radius, 0.635 cm in height, and located beneath 0.635 cm of PMMA. The results are shown in figure 4.17. The cylindrical inhomogeneities illustrated on these curves have been drawn to scale with the depth axis. The maximum and mean deviations between calculated and measured doses were found to be well within the ± 5 % target.

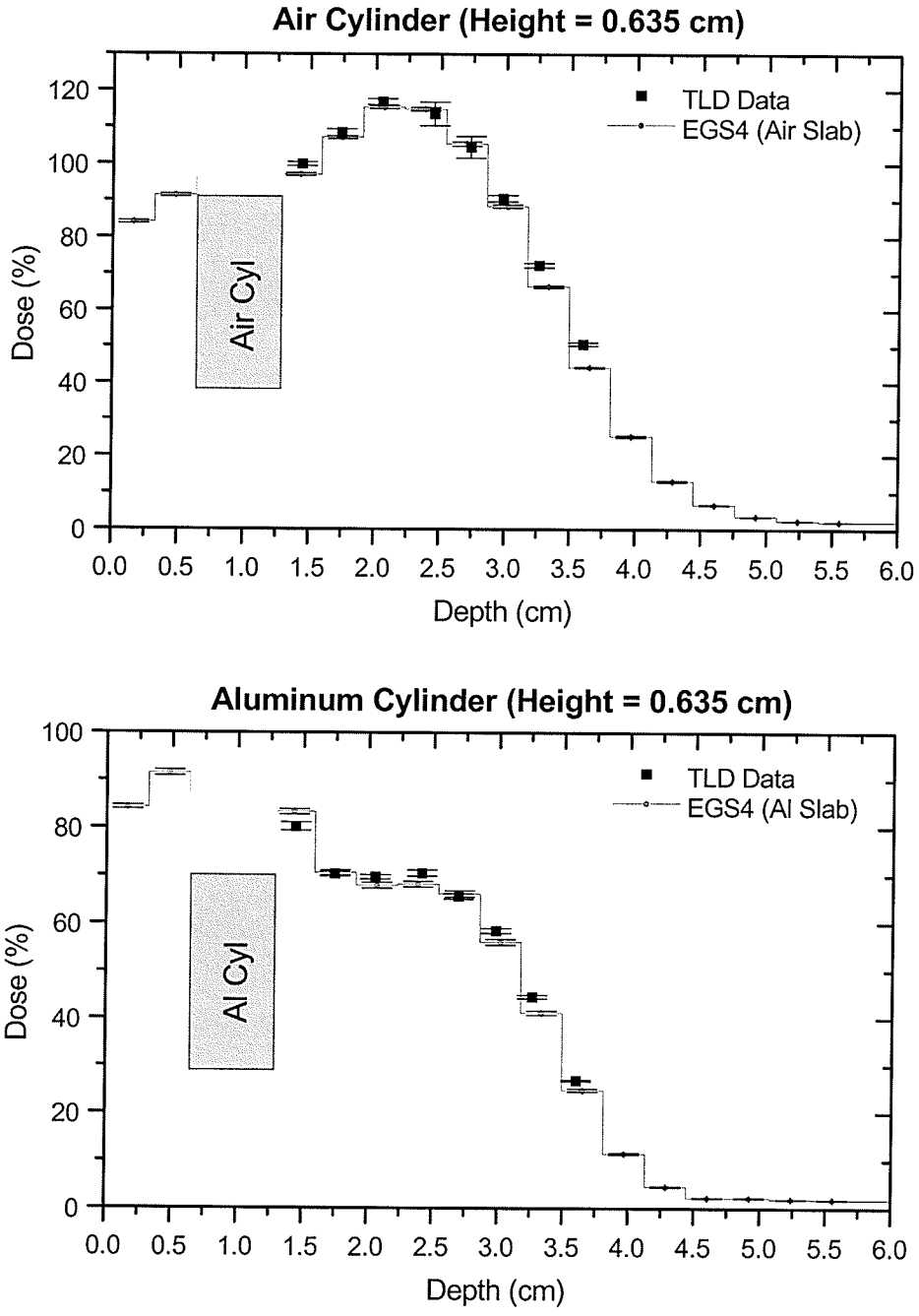

Figure 4. 17 TLD measurements (square points) are plotted here for a PMMA phantom containing a cylindrical inhomogeneity. The Monte Carlo data and the TLD measurements differ by less than 5 %, verifying the ability of EGS4 to accurately predict the dose behind air and aluminum cylinders in PMMA. The beam energy was 9 MeV, and the field size was 10 cm x 10 cm.

4.3.1.2 10 cm x 10 cm Field

The ability of Helax and Focus to predict the dose deposited beneath cylindrical inhomogeneities exposed to a 10 cm x 10 cm beam of 9 MeV electrons is illustrated in figures 4.18 - 4.20. From these data it was observed that at shallow depths Focus under predicted the dose beneath air cylinders. However as the depth is increased, Focus predictions tended toward excessive values. These trends were reversed for the aluminum cylinder. The behavior of Focus predictions in the vicinity which was immediately adjacent to the inhomogeneity was an illustration of the inadequacy of the semi-infinite slab approximation. Helax predictions did not vary significantly with cylinder height. Consequently the Helax results did not exhibit any consistent trend with respect to the Monte Carlo data.

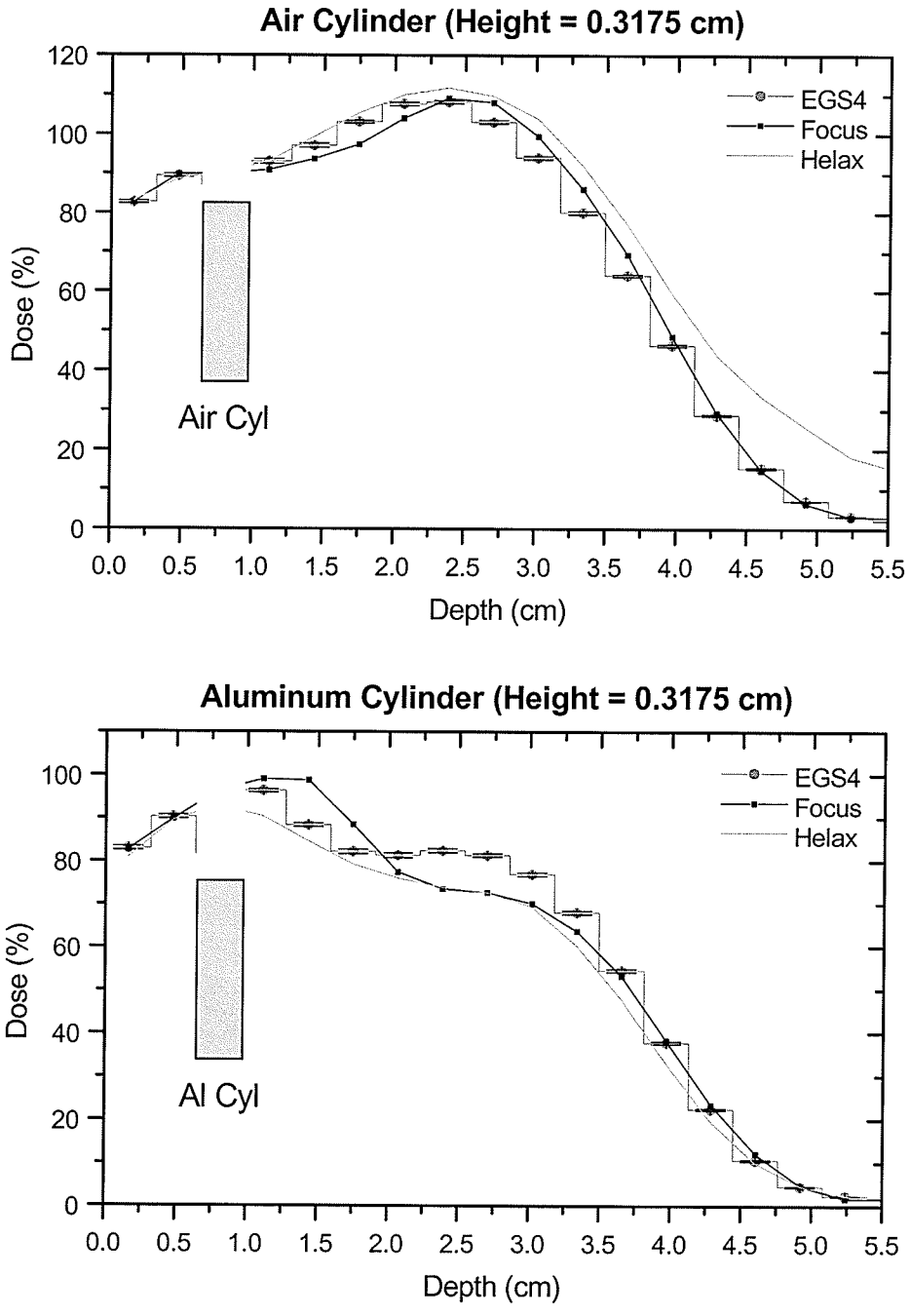

Figure 4. 18 This figure illustrates the dose distributions predicted beneath the central axis of a cylinder of 0.3175 cm thickness and 0.635 cm radius. The cylinder was located 0.635 cm below the surface of a water phantom. The beam energy was 9 MeV, and the field size was 10 cm x 10 cm.

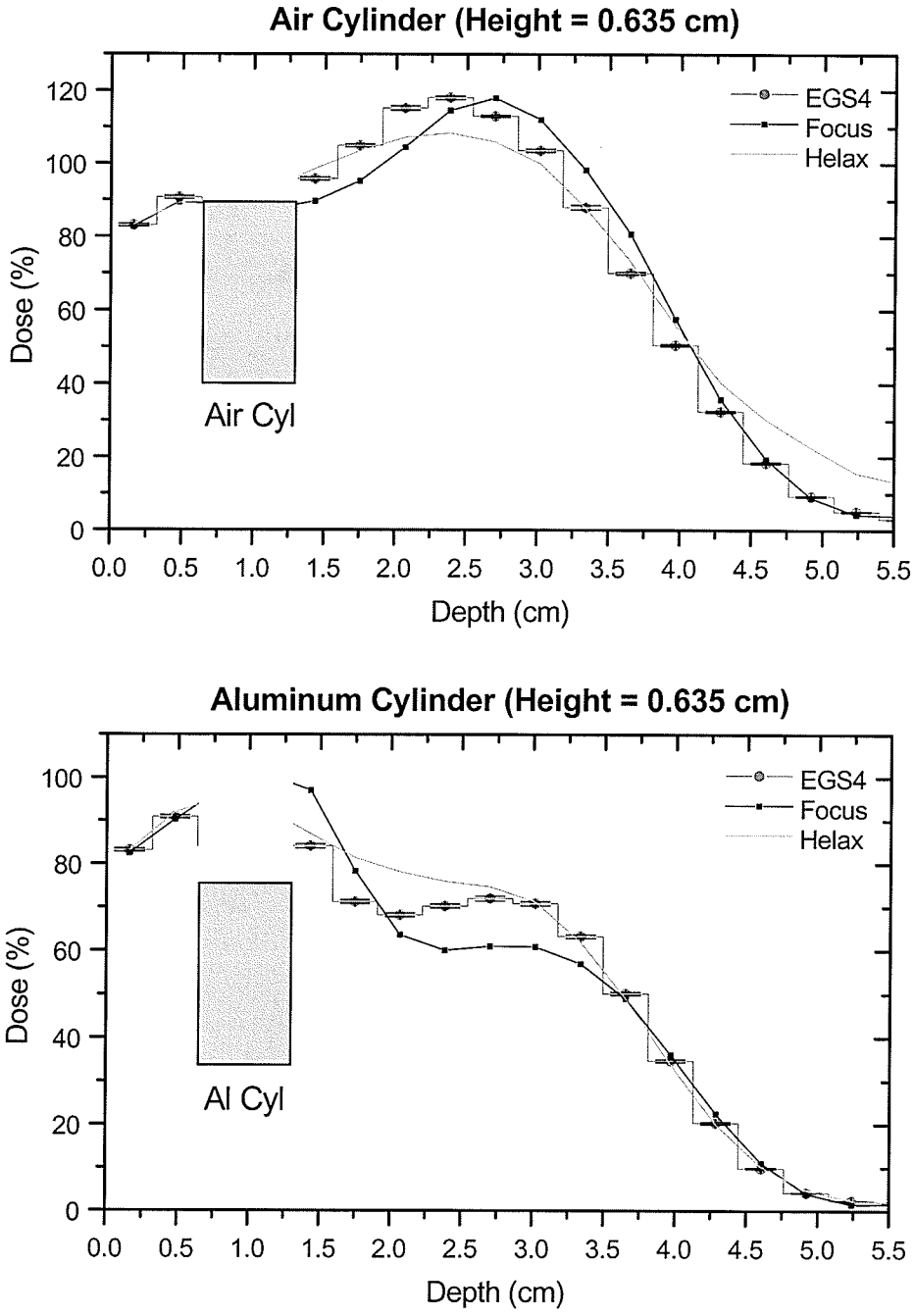

Figure 4. 19 This figure illustrates the dose distributions predicted beneath the central axis of a cylinder 0.635 cm in radius and height, located 0.635 cm below the surface of a water phantom. The beam energy was 9 MeV, and the field size was 10 cm x 10 cm.

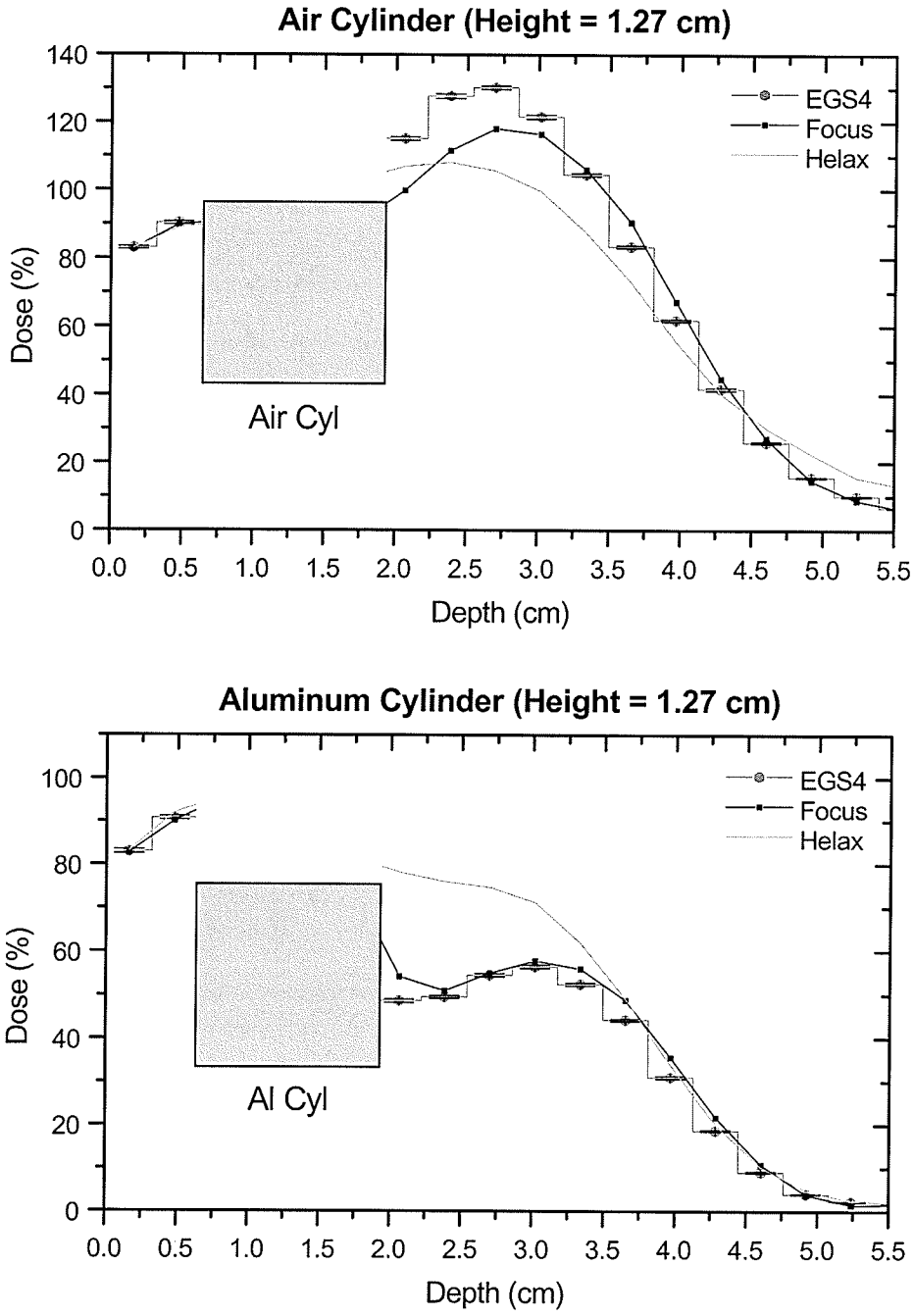

Figure 4. 20 This figure illustrates the dose distributions predicted beneath the central axis of a cylinder 1.27 cm in height and 0.635 cm in radius. The cylinder was located 0.635 cm below the surface of a water phantom. The beam energy was 9 MeV, and the field size was 10 cm x 10 cm.

The maximum and mean deviation between doses calculated by the treatment planning systems and Monte Carlo simulation are given in table 4.14 below for cylindrical inhomogeneities of height H. The corresponding performance ratings are given in table 4.15

Table 4.14 Summary of the deviation between Monte Carlo and treatment planning calculations for a cylindrical inhomogeneity. The beam energy was 9 MeV and the field size was 10 cm x 10 cm. Tabulated values have been expressed as a percentage of the central axis normalization dose. Quoted cylinder heights correspond to the simulated geometry, these dimensions were reproduced to within ± 0.1 cm on the treatment planning systems.

		Data Above R_{80}				**Data Above R_{50}**			
		Mean Dev. (%)		Max Dev. (%)		Mean Dev. (%)		Max Dev. (%)	
		FOCUS	*HELAX*	*FOCUS*	*HELAX*	*FOCUS*	*HELAX*	*FOCUS*	*HELAX*
Cyl H = 0.3175 cm	*Air*	4.0	4.8	6.1	11.9	4.2	5.7	6.1	12.9
	Al	6.8	5.9	10.4	8.7	5.9	6.4	10.4	8.7
Cyl H = 0.635 cm	*Air*	7.7	4.7	10.7	9.7	8.0	4.6	10.7	9.7
	Al	12.9*	2.8*	12.9*	2.8*	7.9	4.3	12.9	10.2
Cyl H = 1.27 cm	*Air*	9.6	17.0	16.1	24.6	9.0	15.4	16.1	24.6
	Al	Dose beneath cylinder < 80 %				2.5	20.1	5.6	29.5

Entries marked by an asterisk (*) were calculated at only one depth.

These data indicate that 9 MeV Focus predictions beneath air cylinders were typically more accurate than those for aluminum cylinders. Helax accuracy was similar to that of Focus, except for predictions beneath very thick cylinders. In these situations Helax failed severely. Overall results were very poor, with both treatment planning

systems failing in nearly all cases.

Table 4.15 Performance Ratings for Cylinders. The beam energy was 9 MeV , and the field size was 10 cm x 10 cm. Quoted cylinder dimensions correspond to the simulated geometry, these values were reproduced to within ± 0.1 cm on the treatment planning systems.

		Data Above R_{80}		Data Above R_{50}	
		FOCUS	*HELAX*	*FOCUS*	*HELAX*
Cyl H = 0.3175 cm	*Air*	Indeterminate	Failure	Indeterminate	Failure
	Al	Failure	Failure	Failure	Failure
Cyl H= 0.635 cm	*Air*	Failure	Indeterminate	Failure	Indeterminate
	Al	Failure*	Pass*	Failure	Failure
Cyl H = 1.27 cm	*Air*	Failure	Failure	Failure	Failure
	Al	Dose beneath cylinder < 80 %		Indeterminate	Failure

Entries marked by an asterisk (*) were calculated at only one depth.

4.3.1.3 15 cm x 15 cm Field

Doses were calculated beneath the central axis of a cylinder with a radius and height of 0.635 cm. The cylinder was located 0.635 cm below the top surface of a water phantom. The resulting dose distributions are shown in figure 4.21. Table 4.16 lists the maximum and mean deviation between treatment planning predictions and Monte Carlo calculations. Finally, table 4.17 includes the performance ratings scored by Focus and Helax in this situation. Overall results were slightly better than the corresponding 10 cm x 10 cm values.

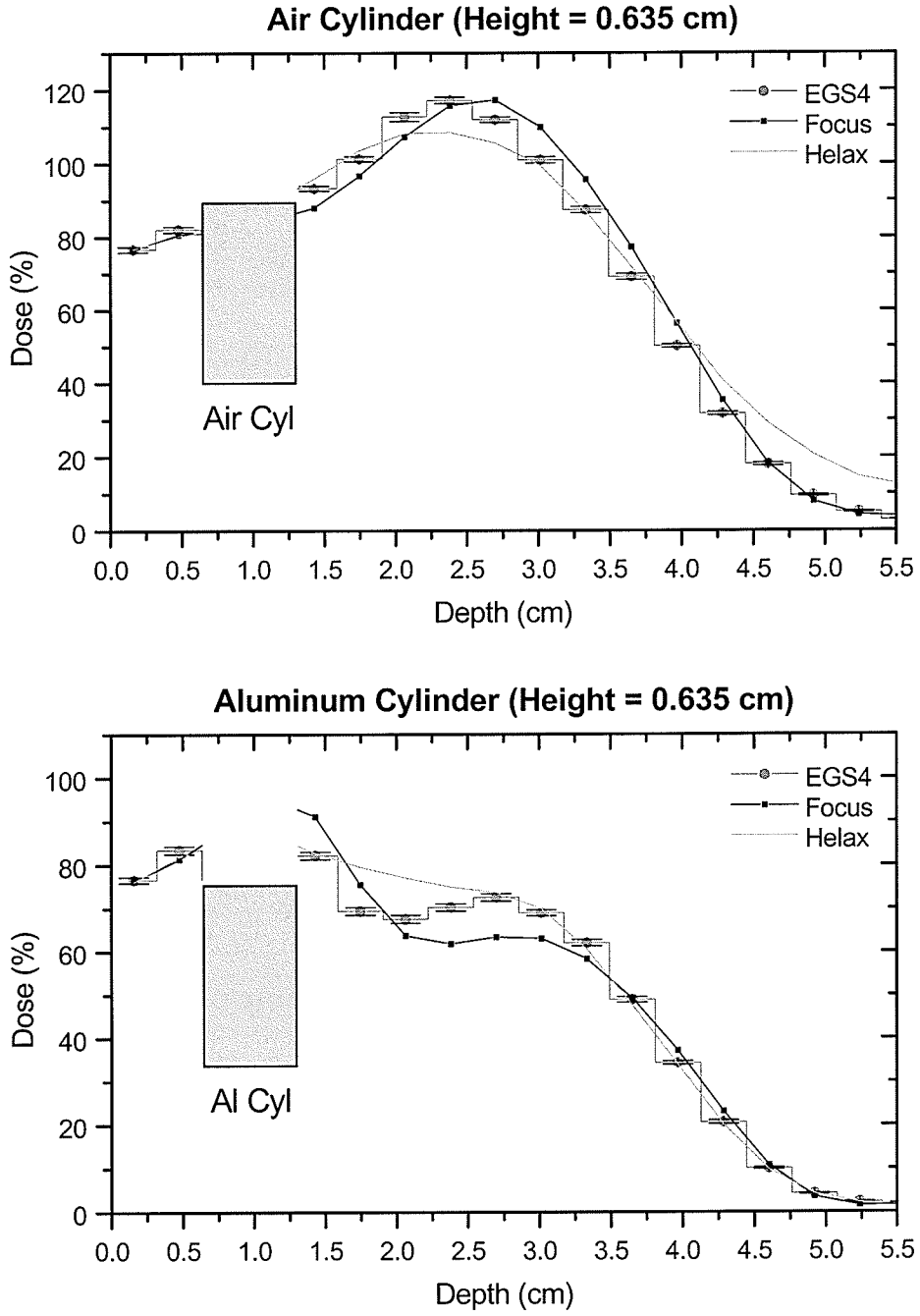

Figure 4. 21 This figure illustrates the dose distributions predicted beneath the central axis of a cylinder 0.635 cm in radius and height. The cylinder was located 0.635 cm below the surface of a water phantom. The beam energy was 9 MeV, and the field size was 15 cm x 15 cm.

Table 4.16 Summary of the deviation between Monte Carlo and treatment planning calculations for a cylindrical inhomogeneity. The beam energy was 9 MeV and the field size was 15 cm x 15 cm. Tabulated values have been expressed as a percentage of the central axis normalization dose. The quoted cylinder height corresponds to the simulated geometry, this value was reproduced to within ± 0.1 cm on the treatment planning systems.

		Data Above R_{80}				**Data Above R_{50}**			
		Mean Dev. (%)		Max Dev. (%)		Mean Dev. (%)		Max Dev. (%)	
		FOCUS	*HELAX*	*FOCUS*	*HELAX*	*FOCUS*	*HELAX*	*FOCUS*	*HELAX*
Cyl H =	*Air*	5.6	3.8	9.0	8.7	6.0	4.0	9.0	8.7
0.635 cm	*Al*	9.0*	0.6*	9.0*	0.6*	7.0	4.5	9.1	10.0

Entries marked by an asterisk (*) were calculated at only one depth.

Table 4.17 Performance Ratings for Cylinders. The beam energy was 9 MeV Beam, and the field size was 15 cm x 15 cm. The quoted cylinder height corresponds to the simulated geometry, this value was reproduced to within ± 0.1 cm on the treatment planning systems.

		Data Above R_{80}		**Data Above R_{50}**	
		FOCUS	*HELAX*	*FOCUS*	*HELAX*
Cyl H =	*Air*	Failure	Indeterminate	Failure	Indeterminate
0.3175 cm	*Al*	Failure*	Pass*	Failure	Failure

Entries marked by an asterisk (*) were calculated at only one depth.

4.3.2 18 MeV Beam

4.3.2.1 Verification of Monte Carlo Calculations

The accuracy with which 18 MeV EGS4 simulations matched TLD measurements was investigated for cylindrical inhomogeneities 0.635 cm in radius, located beneath 1.27 cm of PMMA. The air cylinder had a height of 2.54 cm, while the aluminum cylinder was 1.27 cm high. The results are shown in figure 4.22.

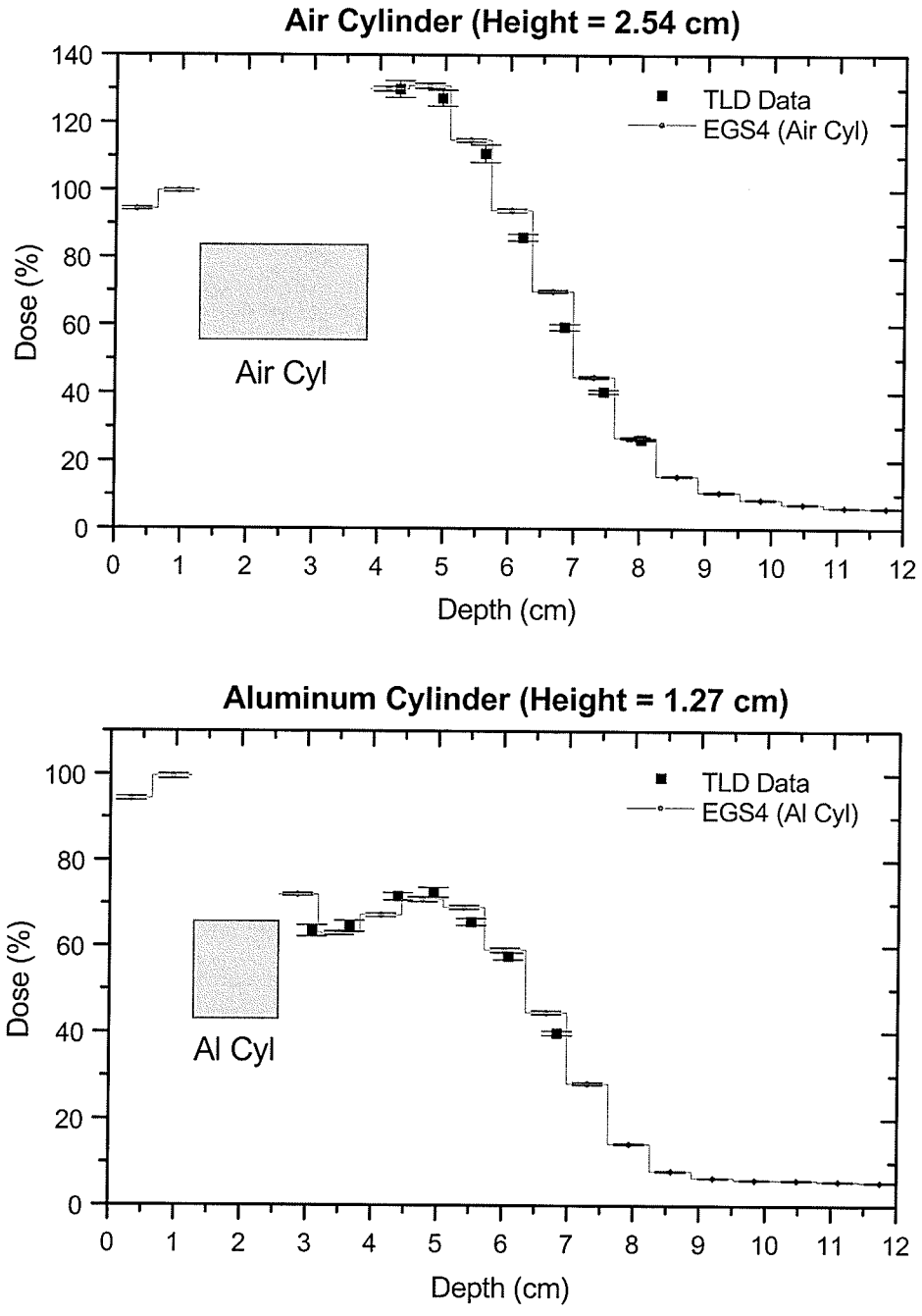

Figure 4.22 TLD measurements (square points) are shown here for a PMMA phantom containing a cylindrical inhomogeneity. The Monte Carlo data and the TLD measurements differ by less than 5 %, verifying the ability of EGS4 to accurately predict the dose behind air and aluminum cylinders in PMMA. The beam energy was 18 MeV, and the field size was 10 cm x 10 cm.

The maximum and mean deviation between calculated and measured doses was found to be within the ± 5 % target.

4.3.2.2 10 cm x 10 cm Field

The dose distributions predicted by Helax and Focus beneath cylindrical inhomogeneities exposed to a 10 cm x 10 cm beam of 18 MeV electrons are illustrated in figures 4.23 - 4.25 . From these data it was observed that both Focus and Helax were under-predicting the high dose region behind air cylinders. Furthermore, both systems suggested a dose which is greater than that seen in the low dose region beneath aluminum cylinders. These trends were consistent with the expected failure of the semi-infinite slab approximation. A more quantitative description of the accuracy of the treatment planning predictions is included in tables 4.18 and 4.19

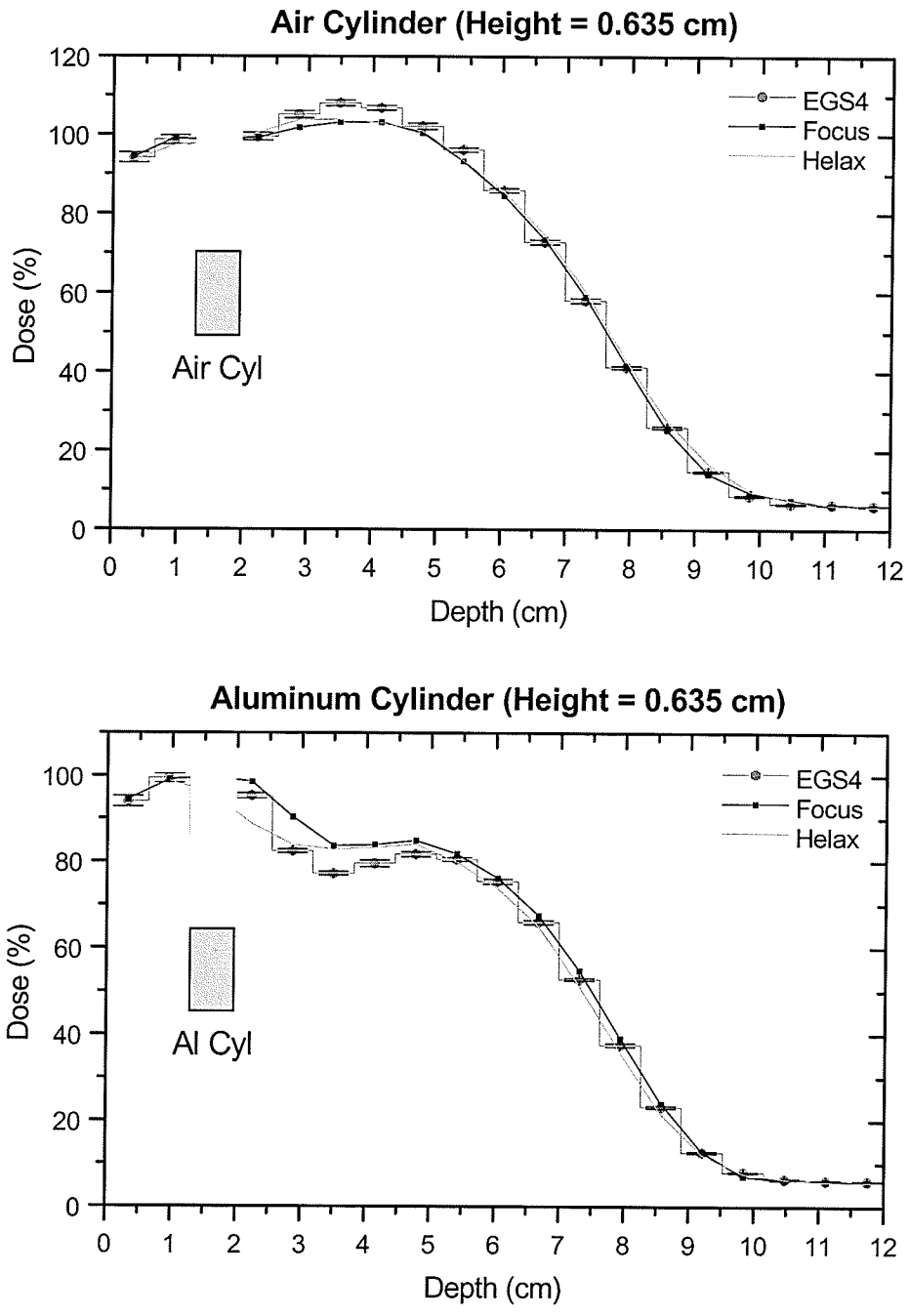

Figure 4. 23 This figure illustrates the dose distributions predicted beneath the central axis of a cylinder 0.635 cm in radius and height. The cylinder was located 0.635 cm below the surface of a water phantom. The beam energy was 18 MeV, and the field size was 10 cm x 10 cm.

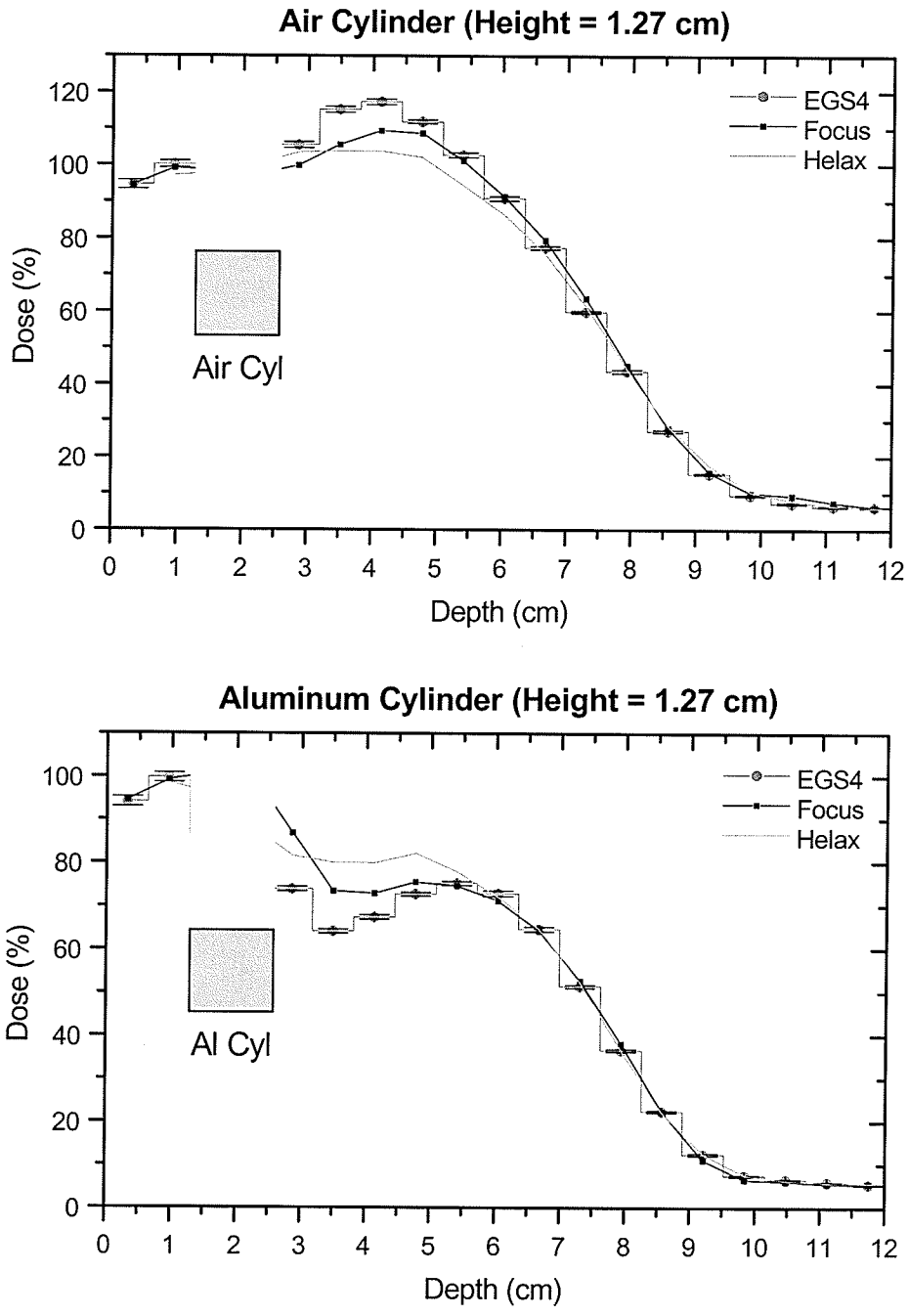

Figure 4. 24 This figure illustrates the dose distributions predicted beneath the central axis of a cylinder 0.635 cm in radius and 1.27 cm in height. The cylinder was located 0.635 cm below the surface of a water phantom. The beam energy was 18 MeV, and the field size was 10 cm x 10 cm.

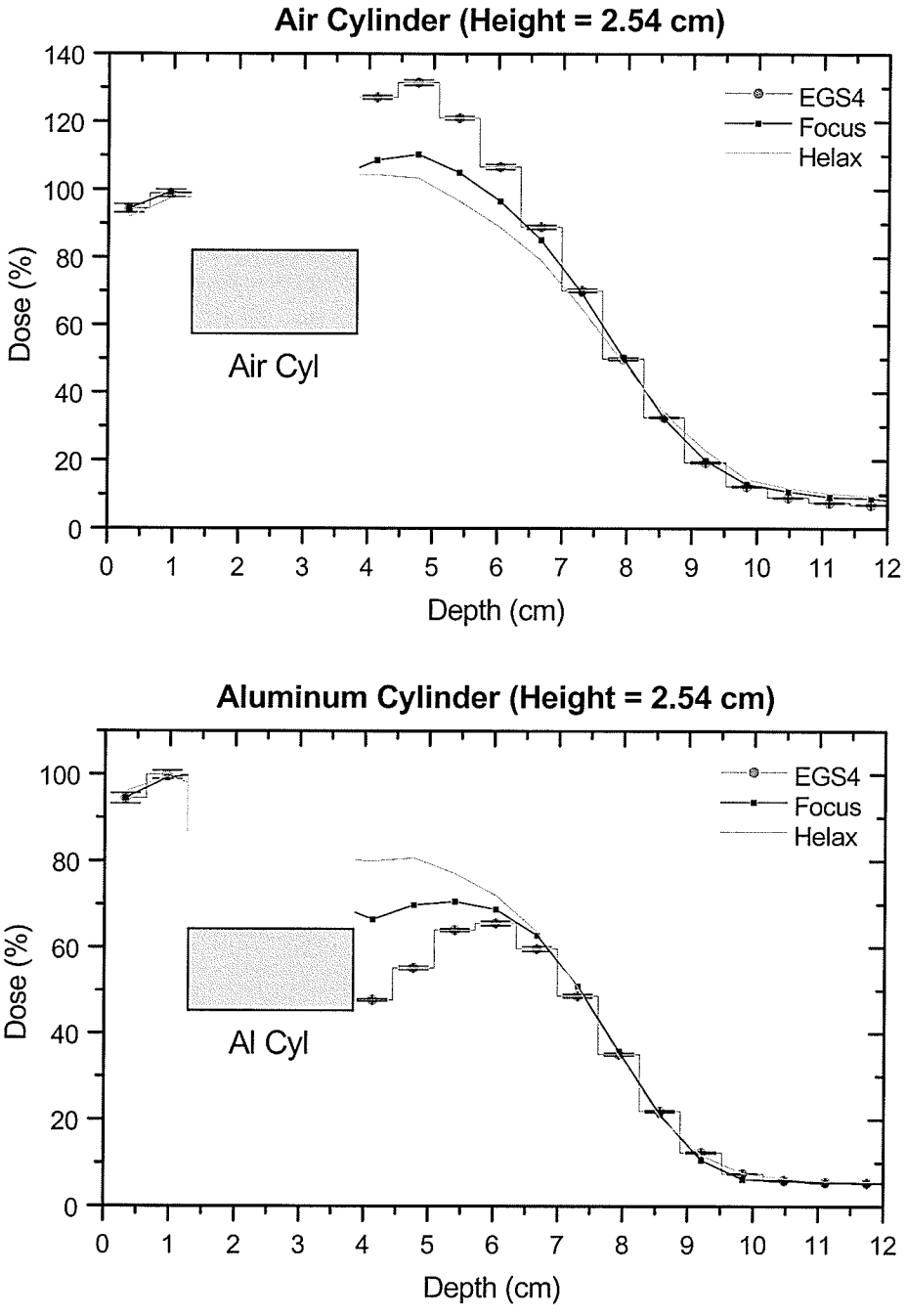

Figure 4. 25 This figure illustrates the dose distributions predicted beneath the central axis of a cylinder 0.635 cm in radius and 2.54 cm in height. The cylinder was located 0.635 cm below the surface of a water phantom. The beam energy was 18 MeV, and the field size was 10 cm x 10 cm.

Table 4.18 Summary of the deviation between Monte Carlo and treatment planning calculations for a cylindrical inhomogeneity. The beam energy was 18 MeV and the field size was 10 cm x 10 cm. Tabulated values have been expressed as a percentage of the central axis normalization dose. Quoted cylinder heights correspond to the simulated geometry, these dimensions were reproduced to within ± 0.1 cm on the treatment planning systems.

		Data Above R_{80}				**Data Above R_{50}**			
		Mean Dev. (%)		Max Dev. (%)		Mean Dev. (%)		Max Dev. (%)	
		FOCUS	*HELAX*	*FOCUS*	*HELAX*	*FOCUS*	*HELAX*	*FOCUS*	*HELAX*
Cyl H = 0.635 cm	*Air*	2.6	2.1	4.8	4.2	2.2	2.1	4.8	4.2
	Al	4.4	3.4	8.0	6.5	3.4	2.7	8.0	6.5
Cyl H = 1.27 cm	*Air*	4.8	8.2	9.6	13.6	4.3	6.6	9.6	13.6
	Al	Dose beneath cylinder < 80 %				4.3	6.2	13.0	15.8
Cyl H = 2.54 cm	*Air*	13.9	20.6	21.1	28.1	10.1	15.6	21.1	28.1
	Al	Dose beneath cylinder < 80 %				9.3	16.2	18.8	32.2

Both Focus and Helax gave very similar results for the thin cylinder (H = 0.635 cm). As the cylinder thickness was increased, the treatment planning systems became less accurate, with the quality of the Helax predictions degrading more rapidly.

Table 4.19 Performance Ratings for Cylinders. The beam energy was 18 MeV, and the field size was 10 cm x 10 cm. Quoted cylinder dimensions correspond to the simulated geometry, these values were reproduced to within ± 0.1 cm on the treatment planning systems.

		Data Above R_{80}		Data Above R_{50}	
		FOCUS	*HELAX*	*FOCUS*	*HELAX*
Cyl H =	*Air*	Pass	Pass	Pass	Pass
0.635 cm	*Al*	Indeterminate	Indeterminate	Indeterminate	Indeterminate
Cyl H=	*Air*	Indeterminate	Failure	Indeterminate	Failure
1.27 cm	*Al*	Dose beneath cylinder < 80 %		Failure	Failure
Cyl H =	*Air*	Failure	Failure	Failure	Failure
2.54 cm	*Al*	Dose beneath cylinder < 80 %		Failure	Failure

Dosimetric accuracy was significantly improved over the 9 MeV case, but was still disappointing. As discussed in section 2.3 , Helax and Focus both make use of small angle approximations. Since the scattering power is proportional to the inverse of the energy squared, these approximations became more applicable as the energy was increased. This is one possible explanation for the improved agreement observed at the higher energy.

4.3.2.3 15 cm x 15 cm Field

For the 15 cm x 15 cm field, doses were calculated beneath the central axis of a cylinder with a radius of 0.635 cm, and a height of 1.27 cm. The cylinder was located

1.27 cm below the top surface of a water phantom. The resulting predictions are plotted in figure 4.26 . The results are summarized in tables 4.20 and 4.21. These data indicate that the accuracies of the dose calculations observed beneath cylinders exposed to a 15 cm x 15 cm beam did not differ significantly from those shown for the 10 cm x 10 cm field in tables 4.18 and 4.19.

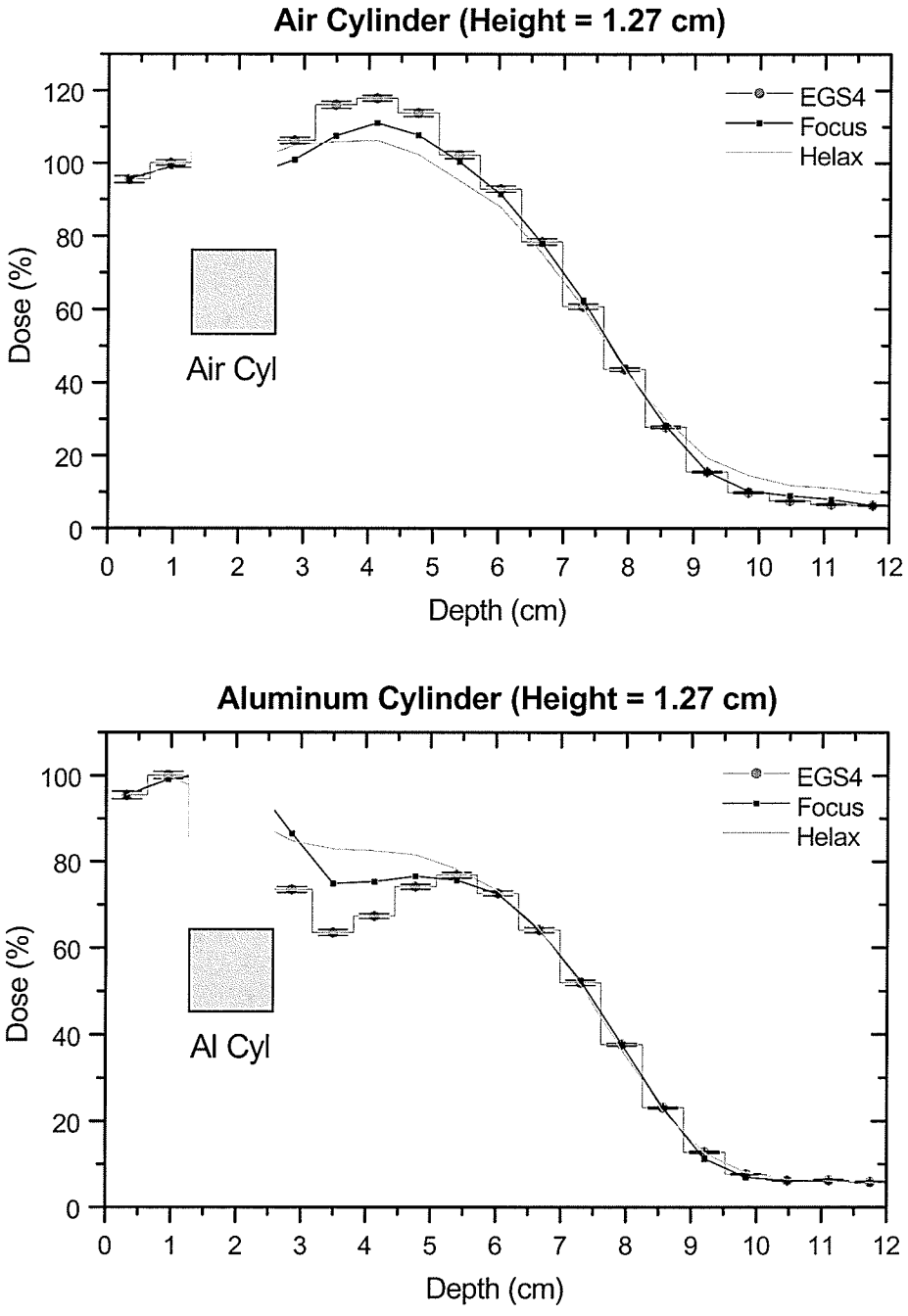

Figure 4. 26 This figure illustrates the dose distributions predicted beneath a cylinder 0.635 cm in radius and 1.27 cm in height. The cylinder was located 0.635 cm below the surface of a water phantom. The beam energy was 18 MeV, and the field size was 15 cm x 15 cm.

Table 4.20 Summary of the deviation between Monte Carlo and treatment planning calculations for a cylindrical inhomogeneity. The beam energy was 18 MeV and the field size was 15 cm x 15 cm. Tabulated values have been expressed as a percentage of the central axis normalization dose. The quoted cylinder height corresponds to the simulated geometry. This value was reproduced to within ± 0.1 cm on the treatment planning systems.

		Data Above R_{80}				**Data Above R_{50}**			
		Mean Dev. (%)		Max Dev. (%)		Mean Dev. (%)		Max Dev. (%)	
		FOCUS	*HELAX*	*FOCUS*	*HELAX*	*FOCUS*	*HELAX*	*FOCUS*	*HELAX*
Cyl H = 1.27 cm	*Air*	5.0	7.8	8.5	11.7	4.0	6.3	8.5	11.7
	Al	Dose beneath cylinder < 80 %				4.6	7.0	13.1	19.4

Table 4.21 Performance Ratings for Cylinders. The beam energy was 18 MeV, and the field size was 15 cm x 15 cm. The quoted cylinder height corresponds to the simulated geometry, this value was reproduced to within ± 0.1 cm on the treatment planning systems.

		Data Above R_{80}		**Data Above R_{50}**	
		FOCUS	*HELAX*	*FOCUS*	*HELAX*
Cyl H = 1.27 cm	*Air*	Indeterminate	Failure	Indeterminate	Failure
	Al	Dose beneath cylinder < 80 %		Failure	Failure

5 Conclusions

The accuracies of the electron dose calculation algorithms implemented by Helax-TMS (version 4.1) and Focus (version 2.5) have been evaluated through a comparison with Monte Carlo calculations. Results calculated by Monte Carlo simulation were found to agree with experimental measurements to within ± 5 %. This investigation involved the prediction of central axis depth dose distributions beneath cylindrical and slab shaped inhomogeneities embedded in a water phantom. Dosimetric accuracy was evaluated over two ranges. The first (Range-80) extended from the base of the inhomogeneity out to R_{80}. The second (Range-50) encompassed the region between the base of the inhomogeneity and R_{50}. In all cases, the shape and dosimetric accuracy of percentage depth dose curves calculated by Focus and Helax did not change substantially when the field size was increased from 10 cm x 10 cm to 15 cm x 15 cm.

When calculating the dose deposited beneath slab-shaped inhomogeneities, the electron dose calculation algorithms are primarily limited by small angle scattering approximations, and in the case of Focus, a failure to model range straggling. The discrepancies between treatment planning and Monte Carlo calculations within phantoms containing slab-shaped inhomogeneities are given in tables 4.5 and 4.10 for beam energies of 9 MeV and 18 MeV respectively. With the exception of Focus predictions beneath aluminum slabs, dosimetric calculations were more accurate at the higher energy. The only dose distributions found to yield consistently accurate results within Range-80

were the 18 MeV Focus predictions beneath air slabs (Maximum deviation < 3 % of normalization dose), and the 18 MeV Helax predictions beneath aluminum slabs (Maximum deviation < 4 % of normalization dose).

In addition to being restricted by the abovementioned approximations, Focus and Helax electron dose calculations in phantoms containing cylindrical inhomogeneities are also subject to the semi-infinite slab approximation. The discrepancies between treatment planning and Monte Carlo calculations within phantoms containing cylindrical inhomogeneities are given in tables 4.14 and 4.18 for beam energies of 9 MeV and 18 MeV respectively. Dosimetric accuracy was found to be unreliable in nearly all cases.

For all inhomogeneity geometries, both treatment planning systems exhibited a decrease in calculation accuracy as inhomogeneity thicknesses were increased. In one example, after increasing the height of an air cylinder from 0.6 ± 0.1 cm to 1.3 ± 0.1 cm, and finally to 2.5 ± 0.1 cm, the maximum deviation between Focus and Monte Carlo distributions calculated for the 18 MeV beam over Range-50 were 4.8 %, 9.6 %, and 21.1 % respectively. The corresponding numbers for the Helax distributions were: 4.2 %, 13.6 %, and 28.1 % respectively.

Overall, the performance of these treatment planning systems was judged to be unacceptable for the accurate dosimetry required in electron radiotherapy. Electron beam treatments are often administered in the head and neck region where the trachea, nasal cavities, sinuses, and multifarious bone structures combine to form very challenging inhomogeneities. The inaccuracies in electron dosimetry observed beneath the simple

slab-shaped and cylindrical inhomogeneities studied in this work indicate that the algorithms implemented by Helax and Focus are likely to perform poorly in the complex geometry involved with patient treatments. The clinical repercussions of this dosimetric inaccuracy will depend on how rapidly the tumor control probability (TCP) and the normal tissue complication probability (NTCP) vary as a function of absorbed dose. The behavior of the TCP and the NTCP changes significantly for different treatment sites.[38]

A rigorous treatment of electron transport is required to achieve a high degree of dosimetric accuracy. This suggests that the method of Monte Carlo simulation is the most appropriate tool for planning electron treatments. With recent advances in computing speed, and through the minimization of redundant calculations, Monte Carlo simulation is rapidly becoming a clinically viable option.[39]

References

[1] F. Khan, "The physics of radiation therapy," 2nd Ed. Baltimore: Lippincott Williams & Wilkins, (1994).

[2] R. Mohan, "Why Monte Carlo," XII th ICCR, 16-18 (1997)

[3] M. Blomquist, M. Karlsson, M. Karlsson, "Test procedures for verification of an electron pencil beam algorithm implemented for treatment planning," Radiother. Oncol. **39** 271-286 (1996).

[4] R. Muller-Runkel, S. Cho, "Evaluation of a commercial three-dimensional electron pencil beam algorithm," Med. Phys. **24** 91-101 (1997).

[5] J. Van Dyk, R. Barnett, J. Cygler, P. Shragge, "Commissioning and quality assurance of treatment planning computers," Int. J. Radiat. Oncol. Biol. Phys. **26** 261-273 (1993).

[6] K. Shortt, C. Ross, A. Bielajew, D. Rogers, "Electron beam dose distributions near standard inhomogeneities," Phys. Med. Biol. **31** 235-249 (1985).

[7] C. Ramsey, I Cordrey, K Spencer, A Oliver, "Dosimetric verification of two commercially available three-dimensional treatment planning systems usig the TG 23 test package," Med. Phys. **26** 1188-1195 (1999).

[8] A. Ahnesjö, M. Aspradakis, "Dose calculations for external photon beams in radiotherapy," Phys. Med. Biol. **44** R99-R155 (1999).

[9] I. Lax, A. Brahme, "Electron beam dose planning using Gaussian beams - Energy and spatial scaling with inhomogeneities," Acta Rad. Onc. **24**, 75-85 (1985).

[10] I. Lax, A. Brahme, P. Andreo, "Electron beam dose planning using Gaussian beams - Improved radial profiles," Acta Rad. Suppl. **364**, 49-59 (1983).

[11] Helax-TMS, "Dose formalism and Models in Helax-TMS," Helax AB, a division of the MDS Nordion Group (1998).

[12] CMS, "Calculation physics and clinical applications manual," Vol 1. Computerized Medical Systems Inc., (1998).

[13] K. Hogstrom, M. Mills, P. Almond, "Electron beam dose calculations," Phys. Med. Biol. **26** 445-459 (1981).

[14] L. Eyges, "Multiple scattering with energy loss," Phys. Rev. 74, 1534-1535 (1948)

[15] K. Hogstrom, R. Steadham, "Electron beam dose computation," Teletherapy: Present and Future - Proceedings of the 1996 Summer School, Ed. T. Mackie, Ed. J. Palta, Madison: Advanced Medical Publishing, 137-174 (1996).

[16] A. Bielajew, H. Hirayama, W. Nelson, D. Rogers, "History, overview, and recent improvements of EGS4," Institute for National Measurement Standards National Research Council of Canada Report NRC-PIRS-0436, (1994).

[17] P. Andreo, "Monte Carlo techniques in medical radiation physics," Phys. Med. Biol., **36** 861-920 (1991).

[18] W. Nelson, H. Hirayama, D. Rogers, "The EGS4 code system," Stanford Linear Accelerator Center, (1985)

[19] A. Bielajew, Proceedings from "Radiation Transport Calculations using the EGS4 Monte Carlo System," Lecture 9 - Electron Monte Carlo Simulation, (1993).

[20] H. Bethe, "Scattering of electrons," Z. für Physik **76** 293 (1932).

[21] F. Bloch, "Stopping power of atoms with several electrons," Z. für Physik **81** 363 (1933).

[22] H. Bethe, "Molière's theory of multiple scattering," Phys. Rev. **89** 1256 (1953).

[23] H. Messel, D. Crawford, "Electron-photon shower distribution function," Oxford: Pergamon Press, (1970)

[24] A. Bielajew, D. Rogers, "PRESTA: the parameter reduced electron-step transport algorithm for electron Monte-Carlo transport," Nucl. Instr. and Meth. **B18** 165-181 (1987).

[25] D. Rogers, C. Ma, G. Ding, B. Walters, "BEAM users manual," NRC Canada, (1995).

[26] A. Bielajew, "Fundamentals of the Monte Carlo method for neutral and charged

particle transport," Ann Arbor: University of Michigan, (1998).

[27] Microcal™ Software Inc., ORIGIN™ User's Manual (Version 4.0)," Microcal™ Software, Inc., (1995)

[28] UIN/HCUG, "Osiris version 3.1 - user manual," UIN/HCUG (1995).

[29] R.A.C Siochi, Siemens Medical Systems OCS, Personal communication.

[30] F. Attix, "Introduction to radiological physics and radiation dosimetry," New York: John Wiley & Sons, Inc. (1986).

[31] A. Wu, A. Kalend, R. Zwicker, E. Sternick, "Comments on the method of energy determination for electron beams in the TG-21 protocol," Med. Phys. **11** 871-872 (1984).

[32] PTW-Freiburg, "MP3/MP3-S Therapy beam analyzer - Description of the components and installation manual," Freiburg: PTW-Freiburg (1995).

[33] PTW-Freiburg, "Mephysto version 6.0 - user manual," Freiburg: PTW-Freiburg (1996).

[34] IAEA (International Atomic Energy Agency) *Absorbed Dose Determination in Photon and Electron Beams. An International Code of Pratice* Technical Report Series 277 (Vienna: IAEA) (1987)

[35] PTW-Frieburg, "Instruction manual for PTW-TLD oven," Freiburg: PTW-Frieburg (1992).

[36] Harshaw/Bicron Radiation Measurement Products, "Model 3500 manual TLD reader user's manual", Harshaw/Bicron Radiation Measurement Products (1993).

[37] G. Ding, J. Cygler, G. Zhang, M. Yu, "Evaluation of a commercial three-dimensional electron beam treatment planning system," Med. Phys. **12** 2571-2580 (1999)

[38] J. Munzenrider, A. Brown, J. Chu, L. Coia, K. Doppke, B. Emami, G. Kutcher, R. Mohan, J. Purdy, B. Shank, et al., "Numerical scoring of treatment plans," Int J Radiat Oncol Biol Phys. **21** 147-163 (1991).

[39] I. Kawrakow, "VMC++ electron and photon dose calculations optimized for RTP" Lecture 13 - Voxel Monte Carlo another approach, OMEGA BEAM Workshop (2001).

Appendix I Justification of phantom dimensions

The outer boundaries of an ideal phantom would appear semi-infinite in extent. For the finite phantom used in this work, calculations were not extended far beyond the field edge. Consider an electron which is incident upon the phantom surface right at the field edge. If this electron travels a distance x to the phantom boundary, it may escape into the air and never return. However, if the phantom were infinite in the x direction, the electron would be much more likely to scatter back toward the region of interest. If this scattered electron were able to arrive back at the field region (a minimum total travel distance of 2x), the physical phantom and the ideal semi-infinite phantom would yield different results in the region of interest. On the other hand, if the distance 2x exceeds the CSDA range for electrons with energy equal to the beam energy, the phantom will appear to be semi-infinite within the field region.

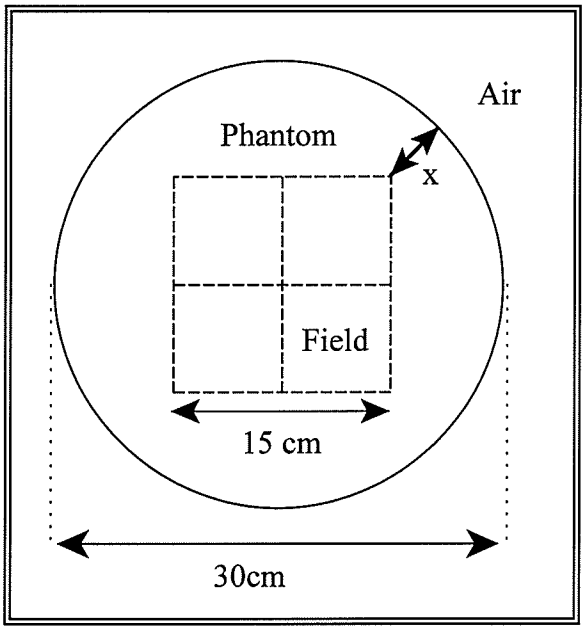

Figure A.1

An electron will be most likely to escape the phantom when high energies and large field sizes are used. Adopting the worst case scenario, a beam of 18 MeV electrons and a 15 cm x 15 cm field is considered. When this field is applied to the center of a

cylindrical phantom of 30 cm diameter, the closest distance from the field edge to the phantom boundary (x) is 4.39 cm. The CSDA range for 18 MeV electrons in water is roughly 8.6 cm, which is less than 8.79 (2x). Thus, within the field region, a cylindrical phantom of 30 cm diameter and height should be indistinguishable from the ideal phantom. The two phantoms are certainly indistinguishable with respect to central axis measurements.

Of course the same could be said of a cubic phantom with sides equal to 30 cm in length. In this case, the distance corresponding to 2x is 15 cm.

Appendix II Measured Phantom Dimensions

Nominal standard PMMA thicknesses were used when specifying Monte Carlo phantom geometries. These same nominal values were reproduced within ± 0.1 cm when defining phantoms in Focus and Helax. The layers used to construct the physical phantom did not match these nominal values exactly. These discrepancies are quantified in the table below. The tabulated differences did not yield significant differences between measured and simulated doses.

Table AII.1 Measured versus nominal thickness of homogeneous layers.

	Layer Index	Nominal Standard Thickness (cm)	Measured Thickness (cm)
Homogeneous Layers	1	0.3175	0.282 ± 0.001
	2	0.3175	0.281 ± 0.001
	3	0.635	0.579 ± 0.001
	4	0.635	0.575 ± 0.001
	5	1.27	1.228 ± 0.004
	6	1.27	1.258 ± 0.006
	7	1.905	1.826 ± 0.007
	8	1.905	1.90 ± 0.02
	9	2.54	2.441 ± 0.008

Table AII.2 Measured versus nominal thickness of inhomogeneous layers.

	Layer Index	Nominal Standard Thickness (cm)	Measured Thickness (cm)
Air Slabs	1	0.3175	0.282 ± 0.001
	2	0.635	0.584 ± 0.001
	3	0.635	0.584 ± 0.001
	4	1.27	1.226 ± 0.006
Aluminum Slabs	1	0.635	0.633 ± 0.002
	2	0.635	0.637 ± 0.001
	3	0.635	0.636 ± 0.001
	4	0.635	0.636 ± 0.001
Air/Aluminum Cylinders	1	0.3175	0.282 ± 0.001
	2	0.635	0.581 ± 0.001
	3	1.27	1.276 ± 0.005
	4	2.54	2.471 ± 0.009
Detector Layer	1	0.635	0.579 ± 0.001

Table AII.3 Measured versus nominal thickness of aluminum plugs. The diameter of the aluminum plugs was measured to be 1.283 ± 0.001 cm. These fit tightly into the cylindrical air cavities, which had a diameter of 1.286 ± 0.001 cm.

	Plug Index	Nominal Standard Thickness (cm)	Measured Thickness (cm)
Aluminum Plugs	1	0.3175	0.271 ± 0.001
	2	0.635	0.592 ± 0.001
	3	1.27	1.285 ± 0.001
	4	2.54	2.480 ± 0.001

Appendix III The Ratio Correction Method

The success of the ratio correction method was tested for cylindrical and slab inhomogeneities using the 18 MeV 10 cm x 10 cm electron beam. In this situation Helax was found to be using depth ionization data instead of depth dose data. Consequently the large discrepancy between Helax and Monte Carlo homogeneous distributions represented a stringent test of the capabilities of the ratio correction technique.

The corrected and uncorrected dose distributions beneath an air slab (thickness = 0.635 cm, depth = 1.27 cm) and an aluminum cylinder (height = 0.635 cm, depth = 1.27 cm)) are shown in figure A.2. An improvement in the uncorrected Helax dose prediction is to be expected if the appropriate depth dose data were to be used. This expectation is particularly valid for the thinnest inhomogeneities irradiated by the18 MeV electron beam. This is because Helax performance is limited by its implementation of the semi-infinite slab approximation, and this approximation is less restrictive when thin inhomogeneities are considered. Furthermore, the accuracy of the small angle scattering approximation implemented by Helax improves as the beam energy increases.

For both inhomogeneities the corrected distribution was observed to introduce an improvement to the un-corrected values. For the slab, the mean discrepancy between Monte Carlo and Helax data across the entire range decreased from 2.1 % to 0.76 % after the correction was introduced. For the cylinder the improvement was from 2.7 % to 1.3 %.

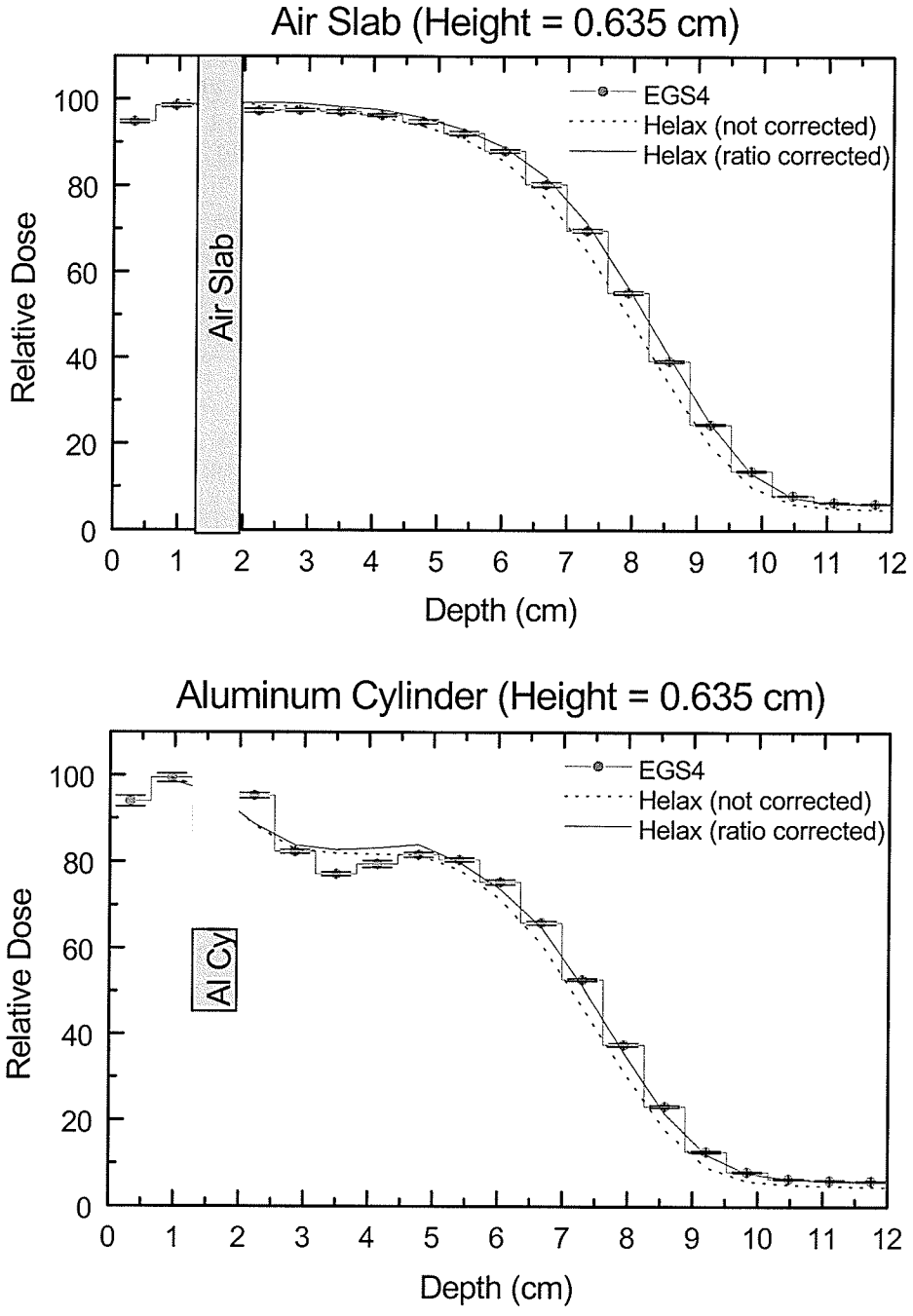

Figure A.2 These inhomogeneities were located 1.27 cm below the surface of a water phantom. Beam energy: 18 MeV. Field size: 10 cm x 10 cm.

Appendix IV

Testing the change in treatment planning calculations with slight variations in inhomogeneity geometry

The values tabulated below represent the mean and maximum deviation of the dose predicted for the altered inhomogeneity from that predicted for the nominal geometry. The electron beam used had an energy of 18 MeV, and was placed at an SSD of 100 cm. The unaltered slab was taken to have a height and depth of 1.27 cm. The unaltered cylinder had the same dimensions, and a diameter which was also equal to 1.27 cm. When varying the inhomogeneity geometry, the height, depth and diameter were each increased by 1 mm.

Table AIV.1 The effect of slight changes in inhomogeneity geometry

		Data Above R80				**Data Above R50**			
		Mean Dev. (%)		Max Dev. (%)		Mean Dev. (%)		Max Dev. (%)	
		FOCUS	*HELAX*	*FOCUS*	*HELAX*	*FOCUS*	*HELAX*	*FOCUS*	*HELAX*
Air Slab	*Thickness*	0.5	0.2	2.0	1.0	0.8	0.4	3.1	2.1
	Depth	0.9	0.1	2.5	0.6	1.5	0.3	5.3	1.1
Al Slab	*Thickness*	0.7	0.7	1.7	1.6	1.3	1.2	4.0	3.3
	Depth	1.2	0.8	2.7	1.6	2.1	1.1	6.3	2.2
Air Cyl	*Height*	4.3	0.5	7.6	0.8	4.4	0.5	7.6	0.8
	Depth	0.6	0.1	0.9	0.2	0.7	0.1	1.4	0.3
	Diameter	1.3	0.6	2.2	1.4	1.4	0.6	2.6	1.4
Al Cyl	*Height*	3.7	0.4	8.8	0.7	3.7	0.4	8.8	0.7
	Depth	0.8	0.6	1.9	0.9	0.9	0.6	1.9	0.9
	Diameter	1.3	1.0	3.4	2.4	1.5	1.4	3.4	2.5